LBL-28544

Lawrence Berkeley Laboratory
UNIVERSITY OF CALIFORNIA

Materials & Chemical Sciences Division

Low Frequency Magnetic Resonance with a dc SQUID

C. Connor
(Ph.D. Thesis)

October 1989

Prepared for the U.S. Department of Energy under Contract Number DE-AC03-76SF00098.

DISCLAIMER

LBL-28544

Low Frequency Magnetic Resonance with a dc SQUID

by

C. Connor

Lawrence Berkeley Laboratory

University of California

Berkeley, California 94720

This work was supported by the Director, Office of Energy Research, Office of Basic Energy Sciences, Materials Sciences Division of the U.S. Department of Energy under Contract No. DE-AC03-76SF00098.

I. INTRODUCTION

Magnetic resonance is a valuable technique for studying a wide variety of problems ranging from biochemistry to solid state physics. In particular, nuclear magnetic resonance (NMR) has been very successfully applied to the study of molecules in solution.[1] Part of the reason for this success is the averaging of internal interactions by the rapid molecular motion in solution. We can divide these interactions into those that are anisotropic, for which the strength of the interaction depends on the orientation of the molecule in a magnetic field, and those that are isotropic.[2] If the molecules were fixed at random orientations in the field, the anisotropic interactions would broaden the resonance line, while the isotropic interactions would merely shift the resonance frequency. In solution, molecular motion of all but the largest molecules occurs on a time scale much shorter than the effective times for these interactions. Isotropic interactions are unaffected by this motion, but anisotropic interactions are time-averaged to some isotropic value. Thus the NMR spectra of molecules in solution usually consists of narrow, well-resolved lines whose positions, determined by the isotropic interactions and the averaged anisotropic interactions, are sensitive indications of the nuclear environment.

No such averaging occurs in solids, so the spectral lines are broadened, making chemical information difficult to extract from the spectrum. However, the scope of high-resolution NMR has been extended to solid samples by artificial averaging techniques, such as sample spinning and multiple pulse averaging.[3] These techniques have been very

successful for nuclei like ^{1}H and ^{13}C, which experience relatively small anisotropic interactions. However, for nuclei that experience quadrupolar interactions, which are often too large to average by these techniques, less success has been achieved.

Parallel to the development of NMR has been that of nuclear quadrupole resonance (NQR), which focuses on the direct measurement of the quadrupole coupling.[4] Pure NQR is carried out in the absence of a static magnetic field. The anisotropy of the quadrupole interaction, which in a magnetic field was determined by the orientation of the molecule with respect to the field, is no longer present. The resonance frequency is then determined solely by the quadrupole interaction, and relatively narrow lines are obtained. This technique has been widely applied to ^{35}Cl and ^{37}Cl, which are two of the few nuclei in which the quadrupole coupling is of an appropriate strength for conventional NQR to be useful. The restricted frequency range comes about because of the detection method used for conventional NMR and NQR. The sample rests inside a coil which is part of a circuit tuned to the resonance frequency.[5] With the appropriate excitation by a radio-frequency magnetic field, the sample magnetization oscillates at the resonance frequency. This time dependent magnetization generates an electric potential across the pickup coil. According to Faraday's Law, the amplitude of the induced voltage is proportional to the frequency, for a given magnetization. This dependence reduces the sensitivity of conventional NQR at low frequency, restricting its use to nuclei with relatively large quadrupole interactions. The frequency range of NQR has been extended to lower frequencies by field-cycling, but in general this

technique is rather cumbersome.[6,7]

To summarize, high resolution NMR of solids is generally restricted to samples with small anisotropic interactions, while NQR is useful for those with large quadrupole interactions. One of the purposes of this dissertation is to present applications of a technique which is useful for nuclei having interactions in the intermediate region, ranging from a few hundred kilohertz to several megahertz. Within this group lie ^{11}B, ^{27}Al, and ^{23}Na, which are found in many important inorganic solids. Often these materials have broad resonances spread over a wide spectral range. The broad bandwidth required for their detection makes conventional magnetic resonance with a tuned circuit difficult or impossible.

Such a technique for low frequency magnetic resonance also has important applications to NMR. When the interaction of the nucleus with the static magnetic field greatly exceeds all the other interactions, including the interaction with the radio-frequency field, the selection rules for transitions between magnetic sublevels become rigidly enforced. Working in a small magnetic field relaxes the selection rules somewhat, allowing previously forbidden transitions to be directly observed.[8] This permits direct observation of interactions that may have been previously only indirectly, if at all, observable. An example will be presented in Chapter VI of the direct measurement of the tunneling splitting of a methyl group at low temperature, using these normally forbidden transitions.

The device which makes these experiments possible is the SQUID (Superconducting QUantum Interference Device).[9] Conventional NMR and NQR

spectrometers use transistor-based detectors, which are responsive only to voltage. This forces the experimenter to convert the sample magnetization to a voltage, a process that is less efficient at low frequencies when the Faraday induction effect is used. However, the SQUID directly measures the magnetization, so there is no frequency dependent sensitivity to the sample magnetization. Of course, many other devices also measure magnetic field directly, but none has the low frequency sensitivity of the SQUID.

Chapter II presents the theory required to extend conventional magnetic resonance to z-axis magnetic resonance, a form most efficient for the SQUID. The operating principles of the SQUID, as well as the techniques used to convert the SQUID response into a useful output voltage, are outlined in Chapter III. The SQUID spectrometer constructed for these experiments is described in Chapter IV. Also in this chapter are a discussion of the design considerations for a SQUID spectrometer, and indications of the overall performance of our instrument. Experimental results on NQR and low frequency NMR are found in Chapters V and VI respectively.

REFERENCES

1. a) R. R. Ernst, G. Bodenhausen, and A. Wokaun, Principles of Magnetic Resonance in One and Two Dimensions (Clarendon Press, Oxford, 1987);
   b) K. Wüthrich, Science 243, 45 (1989).

2. A. Abragam, The Principles of Nuclear Magnetism (Clarendon Press Oxford, 1961).

3. M. Mehring, Principles of High Resolution NMR in Solids, 2nd ed. (Springer, Berlin, 1983).

4. T. P. Das and E. L. Hahn, Solid State Physics, edited by F. Seitz and D. Turnbull, Suppl. 1 (Academic Press, New York, 1958).

5. D. I. Hoult and R. E. Richards, J. Magn. Reson. 24, 71 (1976).

6. D. B. Zax, A. Bielecki, K. W. Zilm, A. Pines, and D. P. Weitekamp, J. Chem. Phys. 83, 4877 (1985).

7. D. T. Edmonds, Int. Rev. Phys. Chem. 2, 103 (1982).

8. a) J. T. Daycock and G. P. Jones, J. Phys. C 2, 998 (1969);
   b) S. Clough, A. J. Horsewill, P. J. McDonald and F. O. Zelaya, Phys. Rev. Lett. 55, 1794 (1985).

9. a) J. Clarke, Phys. Today 39, 36 (1986);
   b) R. L. Fagaly, Sci. Prog., Oxf. 71, 181 (1986).

II. MAGNETIC RESONANCE THEORY

A. Hamiltonians

This section provides an introduction to some of the interactions between a nuclear spin and its environment. The most important interaction concerning the work reported here is the electric quadrupole coupling, acting between a nuclear spin with $I \geq 1$ and the electric field gradient at the nuclear site.[1] The electric field gradient is usually generated by electrons in non-spherically symmetric orbitals around the nucleus, or by electronic charges on other nuclei near the nuclei of interest. In some cases nearby charges distort spherically symmetric orbitals to produce an electric field gradient. The Hamiltonian for the interaction is written as the product of the electric field gradient and the electric quadrupole moment, eQ,

$$\mathcal{H}_Q = \frac{e^2qQ}{4I(2I-1)} [3I_z^2 - I(I+1) + \frac{\eta}{2}(I_+^2 - I_-^2)] \quad . \qquad \text{II-1}$$

Equation (II-1) is written in the principal axis system of the quadrupole interaction, which is a coordinate system in which the interaction is diagonal. In this axis system, the components of the electric field gradient are V_{zz}, V_{xx}, and V_{yy}, corresponding to the components of the electric field gradient along the z, x, and y axes respectively. According to the Laplace equation, $V_{zz} + V_{xx} + V_{yy} = 0$, so only two parameters are required to define the electric field gradient. By convention they have been chosen as

$$eq = V_{zz} \qquad \eta = \frac{V_{xx} - V_{yy}}{V_{zz}} \qquad \text{II-2}$$

where $|V_{zz}| \geq |V_{yy}| \geq |V_{xx}|$, so that η ranges from 0 to 1. If the electric field gradient possesses cylindrical symmetry around the z-axis then $\eta = 0$. The terms I_z, I_+, and I_- in Equation (II-1) are the components of nuclear spin angular momentum in the principal axis system of the quadrupolar interaction. We will use the symbol ω_Q to denote the transition frequency between nuclear spin states split by the quadrupolar interaction.

The next interaction to be considered is the Zeeman interaction, which results when a nuclear magnetic dipole is placed in a static magnetic field H_o. In a frame in which the field is along the z-axis,

$$\mathcal{H}_z = -\gamma\hbar H_o I_z \quad . \qquad \text{II-3}$$

The product of the gyromagnetic ratio γ and the field strength H_o is defined as the Larmor frequency, $\omega_o = \gamma H_o$. If the quadrupole interaction produces much larger splittings than does the Zeeman interaction, it is usually more convenient to write the Zeeman term in the principal axis system of the quadrupolar interaction,

$$\mathcal{H}_z' = -\gamma\hbar H_o(I_z\cos\theta + I_x\sin\theta\cos\phi + I_y\sin\theta\sin\phi) \quad . \qquad \text{II-3}'$$

In this equation θ and ϕ are the polar and azimuthal angles respectively, which relate the direction of the magnetic field to the principal axis system of the quadrupolar interaction.

We also need to consider the effect of a third interaction, that

of a time-dependent radio frequency (rf) magnetic field, $H_1\cos\omega t$. If the field is applied along the x-axis of the frame in which we are interested, it can be written

$$\mathcal{H}_1 = -\gamma\hbar H_1 I_x \cos\omega t \quad . \qquad \text{II-4}$$

Since the field is applied along only one axis, it is a linearly polarized rf field. We will be concerned also with circularly polarized rf fields, for which the Hamiltonian is

$$\mathcal{H}_1 = -\gamma\hbar H_1 (I_x \cos\omega t \pm I_y \sin\omega t) \quad . \qquad \text{II-5}$$

The sign of the I_y term depends on the direction of circular polarization.

The fourth and final interaction to be considered is that between two magnetic dipoles. In the principal axis system of the dipolar interaction, the Hamiltonian for two spins I and I′ is written

$$\mathcal{H}_d = \frac{\hbar\gamma\gamma'}{r^3}(A + B + C + D + E + F) \qquad \text{II-6}$$

where

$$A = I_z I_z'(1 - 3\cos^2\theta)$$

$$B = -\frac{1}{4}(I_+ I_-' + I_- I_+')(1 - 3\cos^2\theta)$$

$$C = -\frac{3}{2}(I_z I_+' + I_+ I_z')\sin\theta\cos\theta e^{-i\theta}$$

$$D = -\frac{3}{2}(I_z I_-' + I_- I_z')\sin\theta\cos\theta e^{+i\theta}$$

$$E = -\frac{3}{4}(I_+ I'_+)\sin^2\theta e^{-2i\theta}$$

$$F = -\frac{3}{4}(I_- I'_-)\sin^2\theta e^{+2i\theta} \quad .$$

The angles θ and ϕ relate the principal axis system of the dipolar interaction to the laboratory frame, and r is the distance between the nuclei. If the nucleus of interest is dipolar-coupled to more than one nucleus, Equation (II-6) is modified to consist of the sum of the corresponding dipolar interactions.

Two characteristic times describing the spin system will also be used. These are T_1 and T_2, whose operational definitions will be the time required for the spin system to exchange energy with the lattice and with other spins, respectively.

B. Conventional NMR and NQR

We now present a very brief and general description of conventional magnetic resonance. If the quadrupolar Hamiltonian is the dominant interaction, the experiment is referred to as NQR, while if the Zeeman interaction, Equation (II-3) is dominant, we use the term NMR. The total Hamiltonian, which is the sum of all the relevant Hamiltonians, creates a splitting of the spin states. Using a radio frequency field, with a frequency matching the splitting frequency, the experimenter generates a coherent superposition of spin states. The spin states involved are almost always separated by $\Delta m = 1$. This coherence usually corresponds to a macroscopic magnetization oscillating at the resonance frequency. Detection is effected by a voltage induced in a

coil, which forms part of a resonant circuit tuned to the frequency of the transition.

These experiments can generally be classified as either pulsed or continuous wave (cw). Pulsed experiments involve a short intense burst of resonant radiation, after which the induced time dependent magnetization decays to zero. The decay rate is often on the order of T_2, and in some simple cases may be T_2 itself. A Fourier transform of the decay gives the absorption signal. In cw experiments the frequency of a small rf field is swept slowly through the resonance position. At resonance the field is effective in inducing transitions, so power is absorbed from the field. Under the appropriate conditions, a plot of the power absorbed as a function of the rf frequency yields the absorption signal. Numerous texts describe the principles and techniques of these experiments more fully.[2]

C. Z-axis cw NMR of Spin 1/2 Nuclei

In this and the following section we describe a different class of magnetic resonance techniques. These experiments are made possible by the ability of the SQUID to detect magnetization at very low frequencies. This section concentrates on the simplest magnetic resonance experiment that can be done with the SQUID spectrometer.[3] It consists of sweeping a small, linearly polarized rf field through the resonance frequency of a system of isolated spin 1/2 nuclei, in a constant magnetic field. The energy level diagram for such a system is given in Figure II.1. The populations at thermal equilibrium are given

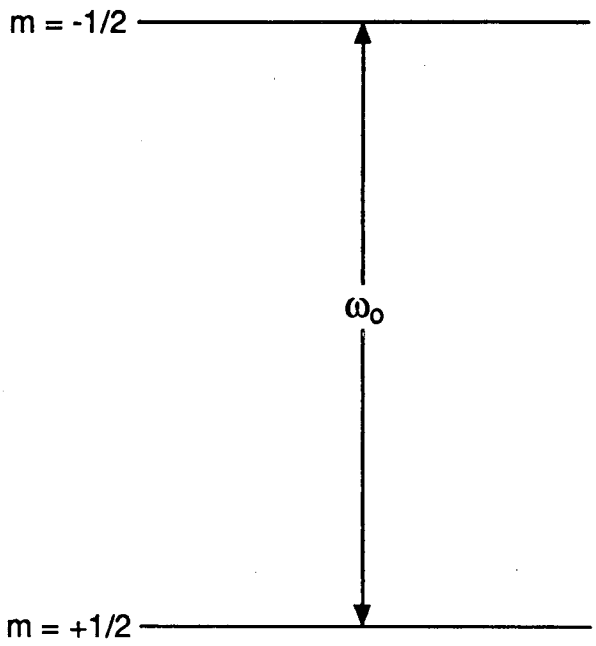

Figure II.1: Energy levels of a spin 1/2 nucleus in a magnetic field H_o. The levels are split by the Larmor frequency $\omega_o = \gamma H_o$.

by the Boltzmann distribution. Under most experimental conditions the ratio $\hbar\omega_o/kT$ is very small, so only the first term in the expansion of the exponential is necessary for calculations. This so-called high temperature expansion will be valid for all the work discussed here.

At thermal equilibrium, the spin system will exhibit a magnetization along the magnetic field, which we take to be along the z-axis. Using the high temperature approximation, the equilibrium magnetization is given by

$$M_z^o = \frac{N\gamma^2\hbar I(I+1)}{3kT} H_o \qquad \text{II-7}$$

where N is the density of spins (i.e. the number of spins per unit volume). This magnetization produces a fixed dc output from the SQUID. To determine the resonance frequency, it is necessary to produce a change in M_z. This is done by slowly sweeping a small rf field through the resonance frequency. At resonance, the field will induce transitions between the two levels, reducing the magnetization. Thus, by monitoring the z-axis magnetization as a function of the frequency of the rf field, we are able to measure the level splitting.

In order to qualitatively describe the lineshapes observed using this technique, it is necessary to consider the effect of the sweep rate and the strength of the rf field.[4] We somewhat arbitrarily divide the effect of the rf into three regimes: non-saturating, saturating, and adiabatic rapid passage.

First we discuss the non-saturating case. As the name implies, the effect of the rf field is so small that its effect on the z-axis

magnetization is negligible. Although some transitions are induced by the field, the transition rate is much less than $1/T_1$, the spin-lattice relaxation rate. This is the regime in which many conventional cw NMR experiments are carried out. Of course, since the change in M_z is negligible, no signal will be observed by the SQUID. The condition to be satisfied in non-saturating NMR is

$$W \ll \frac{1}{T_1} \qquad \text{II-8}$$

where $W = \pi\gamma^2 B_1{}^2 g(\omega)$ is the rate of transitions induced by the rf, and $g(\omega)$ is the normalized line shape in units of inverse hertz.

The second case is the saturating sweep, obtained at higher rf levels such that

$$W \gg \frac{1}{T_1} \quad . \qquad \text{II-9}$$

The rf field adds energy to the spin system faster than it can be dissipated by heat leaks to the lattice, so the effective temperature of the spin system is increased. According to Equation (II-7), an increased temperature corresponds to a reduced magnetization. The strongest effect this saturating rf field can have is to completely destroy the magnetization, so the maximum change in M_z is just M_z^o. After the rf frequency has passed through the resonance frequency, the magnetization will exponentially return to its equilibrium value of M_z^o. The spin-lattice relaxation time may be directly measured from this recovery.

To deduce the expected lineshape, we need to consider that the line has some characteristic width Δ_o. If the sweep rate κ is very slow,

so that the time required to traverse the line is much longer than T_1, the normal absorption spectrum will be obtained. On the other extreme, if the line is swept much faster than T_1, the integral of the absorption line is observed. The true lineshape and resonance frequency can then be obtained by taking the derivative. Figure II.2 shows simulations of the lineshape as a function of the sweep rate. The simulated lineshape, $S(\omega)$ is defined by

$$S(\omega) = \int_0^{\omega} g(\omega') e^{-(\omega - \omega')/\kappa T_1} \, d\omega' \quad . \qquad \text{II-10}$$

For these simulations a Gaussian function was used for $g(\omega)$, appropriate to broadening by dipolar couplings in solids. In the limit of very fast or very slow sweeps the line shape and line centers are easily obtained. For the situation in between, the line centers are most easily found by adding forward and reverse sweeps and using the center of the resulting symmetric pattern. If the linewidth is also required, it may be obtained by measuring T_1 from the spectrum, then using a model function for the line shape, such as a Gaussian, to simulate the observed spectra.

The third situation to be discussed is the adiabatic rapid passage. To perform this experiment it is neccessary to sweep through the line in a time much less than T_1. This condition prevents heat transfer between the lattice and the spin system during the passage, hence the term "rapid". The adiabatic condition requires that the effective magnetic field, which is the sum of the rf and static fields, varies so slowly that the magnetization is always oriented along the direction of the effective field. These conditions can be summarized by

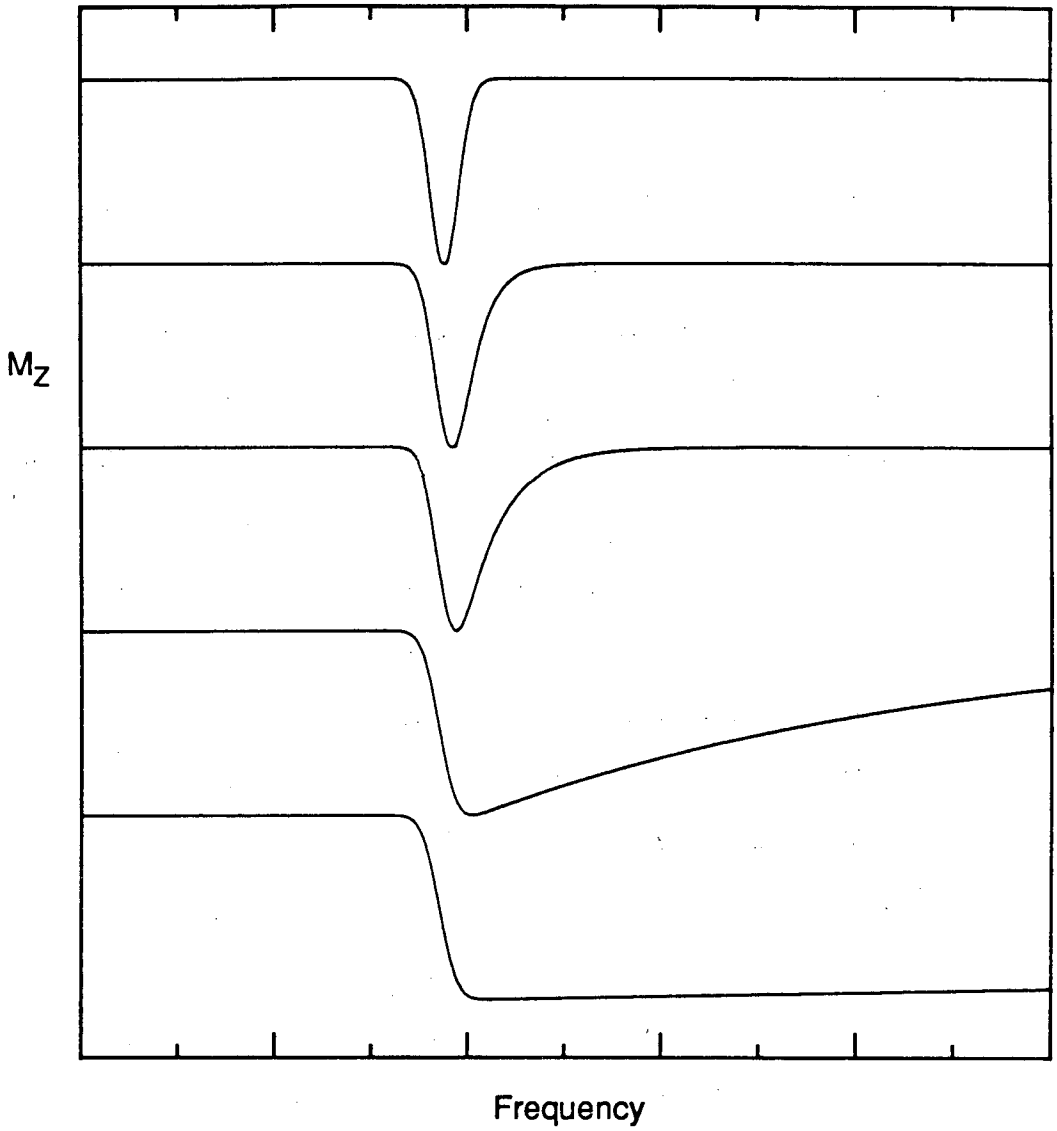

Figure II.2: Simulated z-axis cw NMR lineshapes for a sweep through the resonance frequency of a spin 1/2 system. The sweep rates range from very slow (upper trace) to very fast (lower trace).

$$(\gamma B_1)^2 \gg \frac{d\omega}{dt} \gg \frac{\Delta_o}{T_1} \qquad \text{II-11}$$

where the first inequality assures adiabaticity and the second the rapid condition. If Equation (II-11) is satisfied, the effect on the spin system will be an inversion of the magnetization, so that it is left antiparallel to the static field. The change in M_z is then $2M_z^o$, twice as large as the maximum change for the saturating passage. The equilibrium condition returns with a time constant T_1, as in the saturating sweep, and the lineshape obtained is similar to that for the faster sweeps in Figure II.2. In practice, the maximum rf amplitude that can be applied is limited by coupling of the rf field to the SQUID, as will be discussed fully in Chapter IV. This restriction forces us to do most experiments in the saturating mode.

We should note that although this section has dealt mainly with a simple two level system, the experiment will work on more complex systems as well. The change in the populations of virtually any two levels of most multilevel systems will produce a change in the magnetization of the spin system.

D. Z-axis cw NQR

In this section we consider the problem of detecting the energy level splitting produced by the quadrupole interaction, given by Equation (II-1), on a half-integer spin with $I \geq 3/2$. The theory for this problem was originally worked out by Weber and Hahn,[5] who also did

experiments using a conventional NQR spectrometer. Jach did the first experiments of this type with a SQUID-based spectrometer, applied to ^{27}Al (spin 5/2).[6] Initially a spin 3/2 system is considered, and then the straightforward extension to spin 5/2 is made. The energy level diagram for a spin 3/2 in an axially symmetric ($\eta = 0$) electric field gradient is shown in Figure II.3. For reasons that will be discussed later in this section, a small magnetic field is applied parallel to the direction of the z-axis of the electric field gradient. The magnetic field splits the transition at ω_Q into two components, having frequencies $\omega_Q + \omega_o$ and $\omega_Q - \omega_o$. We think of the energy level system as being comprised of two manifolds, the +m and the -m manifolds, consisting of the +3/2, +1/2 and -3/2, -1/2 levels respectively. Using the high temperature approximation, the relative populations at thermal equilibrium are

$$\begin{aligned} p_{-3/2} &= \tfrac{1}{4}(1 - \xi - \delta) \\ p_{+3/2} &= \tfrac{1}{4}(1 - \xi + \delta) \\ p_{-1/2} &= \tfrac{1}{4}(1 + \xi - \delta) \\ p_{+1/2} &= \tfrac{1}{4}(1 + \xi + \delta) \end{aligned} \qquad \text{II-12}$$

where

$$\xi = \frac{\hbar\omega_Q}{kT} \qquad \text{and} \qquad \delta = \frac{\hbar\omega_o}{kT} \; .$$

The magnetization of the spin system is obtained, as in the case of the spin 1/2, by summing the products of the population of each level

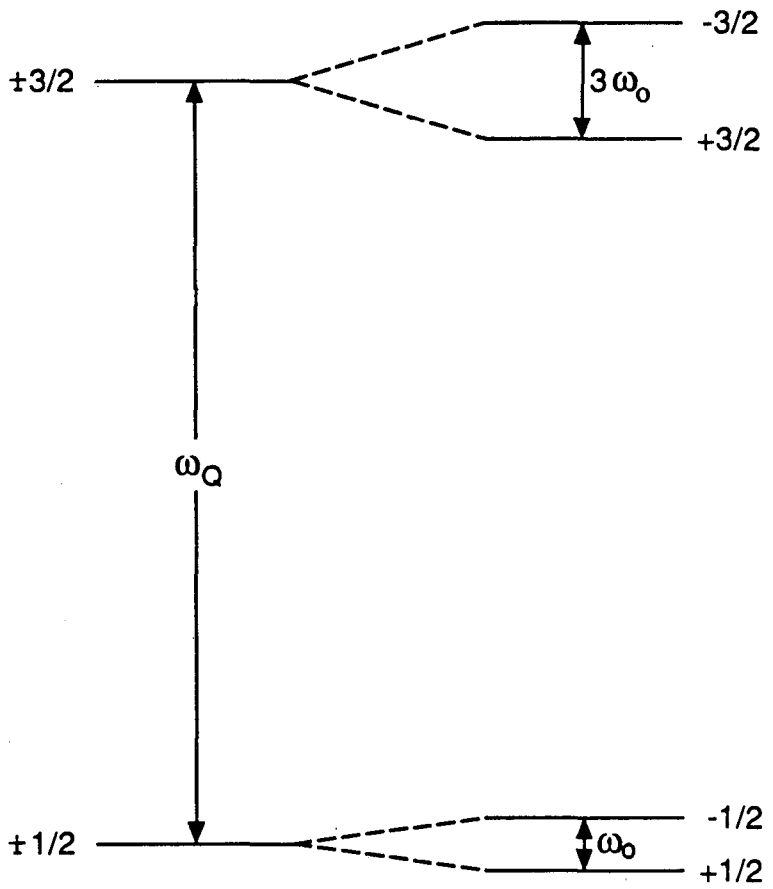

Figure II.3: Energy level diagram for a spin 3/2 nucleus in an axially symmetric electric field gradient ($\eta = 0$). A small magnetic field along the symmetry axis splits the degeneracy of the $\pm m$ states, so the allowed NQR transitions appear at $\omega_Q \pm \omega_o$.

multiplied by the value of M_z for that level

$$M_z = \sum_i p_i M_{zi}$$
$$= N\gamma\hbar \sum_i p_i m_i \quad . \qquad \text{II-13}$$

At thermal equilibrium, Equation (II-13) yields

$$M_z = \frac{N\gamma\hbar}{(2I+1)} \sum_{m=-I}^{I} m \left(1 - \frac{e^2qQ(3m^2 - I(I+1))}{kT \quad 4I(2I-1)} + \frac{\hbar\gamma m}{kT} H_o\right). \qquad \text{II-14}$$

We can simplify this equation by noting that

$$\sum_{m=-I}^{I} m = \sum_{m=-I}^{I} m^3 = 0$$

so there is no contribution to M_z, at thermal equilibrium, from the quadrupolar term. Then Equation (II-14) may be written

$$M_z = \frac{N\gamma^2\hbar^2 H_o}{(2I+1)kT} \sum_{m=-I}^{I} m^2 \qquad \text{II-14'}$$

where the summation over m gives 5 for I = 3/2, and 35/2 for I = 5/2.

Now we consider the effect of a small rf field swept from low to high frequency. We assume that the rf field has sufficient strength to satisfy Equation (II-9), so that the populations of any two levels whose difference matches the rf frequency are equalized. The (+3/2,+1/2) component of the transition is at lower frequency, $\omega_Q - \omega_o$, so the field initially saturates this component. At this point, and before the rf frequency approaches the higher frequency component, the magnetization,

for I = 3/2, is

$$M_z = \frac{N\gamma\hbar}{4kT}\left(\frac{e^2qQ}{4} + \frac{9}{2}\hbar\gamma H_o\right) \quad . \qquad \text{II-15}$$

A comparison with Equation (II-14´), using $\omega_Q >> \omega_o$, shows that the magnetization has been increased by a factor of order ω_Q/ω_o. This is contrasted with the spin 1/2 case, in which the rf field destroys the magnetization. Ignoring any decrease in M_z due to spin lattice relaxation or other effects, the magnetization is still given by Equation (II-15) when the other resonance position is reached. After equalization of the populations of the (-3/2,-1/2) transition, the magnetization is

$$M_z = \frac{4N\gamma^2\hbar^2}{4kT} H_o \qquad \text{II-16}$$

near its initial value in Equation (II-14´). Thus the output of the SQUID is a rectangular peak, centered at ω_Q, with width $2\omega_o$. The quadrupole splitting ω_Q, as well as ω_o if desired, can be directly measured from this spectrum. An idealized representation of the spectrum obtained is given in Figure II.4.

In practice several factors distort this idealized lineshape. The transitions are broadened by dipolar couplings to nearby nuclei[7] and by local variations of the quadrupole coupling parameters. Cross-relaxation between the two manifolds tends to decrease the overall signal amplitude.[8] Spin-lattice relaxation distorts the lineshape when the time spent sweeping between the resonance positions is on the order of T_1 or longer. Also, the response from powder samples, in which the

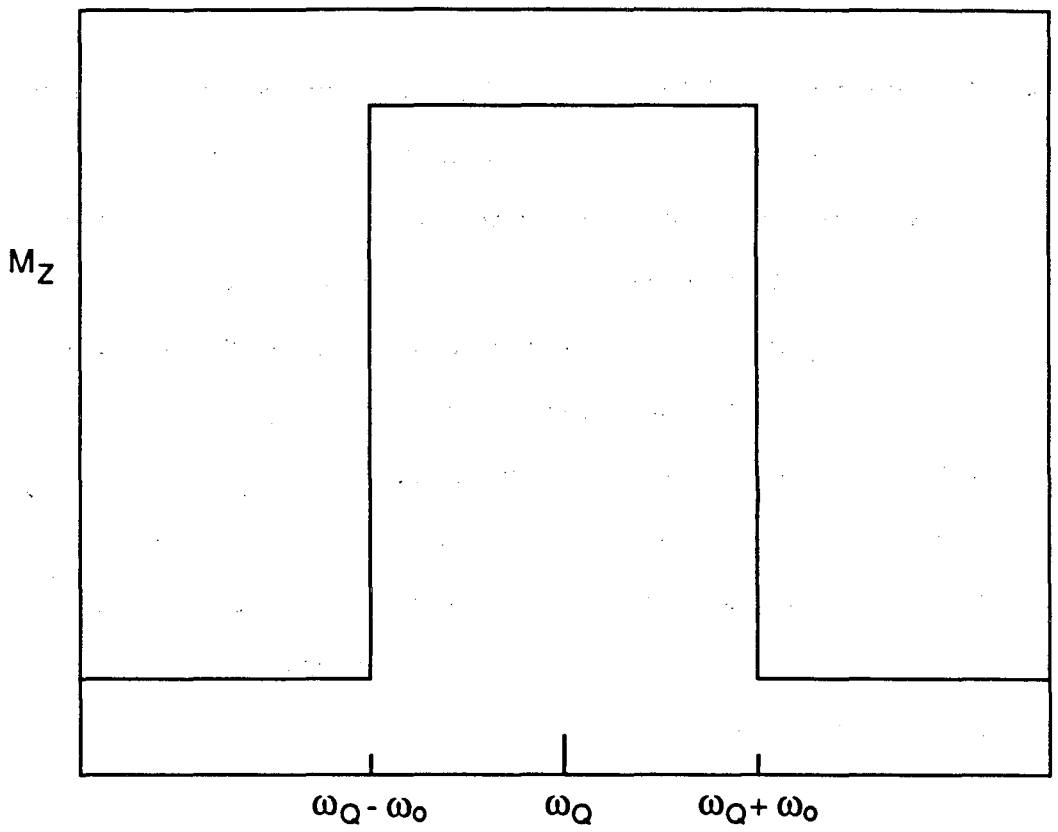

Figure II.4: Idealized z-axis cw NQR lineshape, expected from the frequency sweep through the two components of the transition of a spin 3/2 nucleus in a low magnetic field.

orientations of the electric field gradients are random in space, will not even be approximately rectangular. All of these effects will be discussed below.

First we consider the effect of the dipolar interactions. In most samples the nuclear spins to be observed are not well separated spatially, so a dipolar coupling betwen nuclei will be observed. Since the strength of the coupling depends both on the direction of the internuclear vector and the distance between nuclei, normally a given spin will experience a Gaussian-like distribution of couplings. This produces a Gaussian lineshape, with a characteristic width γH_L, where H_L is called the local field. Abragam and Kambe have given prescriptions for calculating H_L, given the lattice parameters of the sample.[7] For example, in a cubic lattice of spin 3/2 nuclei, with the electric field gradient along the cubic axis, they found

$$H_L^2 = 60.0 \frac{\gamma^2 \hbar^2}{d^6} \qquad \text{II-17}$$

where d is the dimension of the unit cell. Dipolar coupling to both like and unlike nuclei will introduce a dipolar line broadening. For the samples we will be concerned with, H_L is on the order of a few gauss.

Variations in the quadrupolar splitting, due to defects and distortions in the lattice, are another important source of line broadening. This variation may range from fractions of a percent, for well-defined crystals, to ten percent or more for glassy or amorphous materials.

Cross-relaxation between the +m and -m manifolds can have a strong

effect on the signal amplitude, and may destroy the signal completely in some cases. Cross-relaxation, also known as spin diffusion,[8] occurs when two energy level splittings almost coincide. Two spins, coupled by the dipolar interaction, can simultaneously change state in a nearly energy conserving process. This flip-flop, represented by $(+1/2,-3/2) \rightarrow (+3/2,-1/2)$, is shown in Figure II.5. This process corresponds to $\Delta m = +2$ for the entire spin system, so it must be driven by the E term in the dipolar Hamiltonian, Equation (II-6). The change in the total magnetization of the spin system from this flip-flop is $+2\lambda$, where λ is loosely defined as the magnetization from a single spin. Another flip-flop transition, driven by the F term in $\mathcal{H}_D$, can occur with equal probability. This involves the transitions $(+3/2,-1/2) \rightarrow (+1/2,-3/2)$, and produces a change in the total magnetization of -2λ. Although the probabilities for these two flip-flops are equal, since the E and F terms have the same magnitude, their respective rates are different. This is because the number of spin pairs able to undergo the first type of flip-flop is proportional to $(n_{+1/2} \cdot n_{-3/2})$, while the number able to experience the second type of flip-flop is proportional to $(n_{+3/2} \cdot n_{-1/2})$. If the population differences within the two manifolds differ, spin diffusion will tend to equalize them. In particular, if a rf field saturates the +m manifold, so that M_z is increased to its value given in Equation (II-15), spin diffusion will reduce it with a characteristic time T_{SD}. If the rate of transitions induced by the rf field is much less than $1/T_{SD}$, no signal will be observed.

Since cross-relaxation only occurs between transitions of nearly the same energy, we can make the cross-relaxation rate arbitrarily small

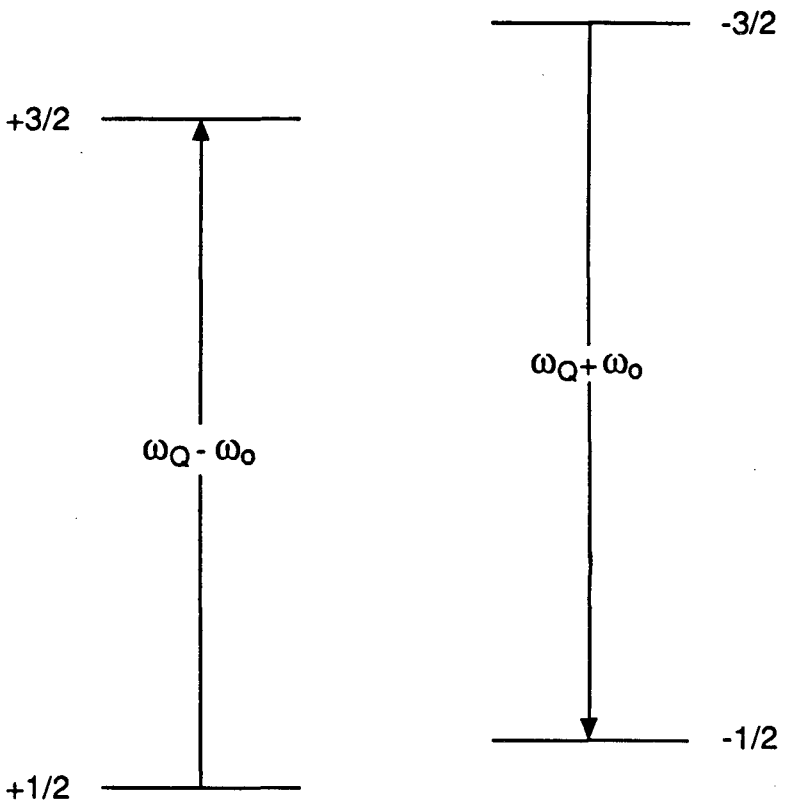

Figure II.5: Flip-flop process involving (+1/2,-3/2)→(+3/2,-1/2), induced by the E term in the dipolar Hamiltonian.

by splitting the transition frequencies of the two manifolds.[6] This is done by applying a small dc field, H_o, along the z-axis of the electric field gradient, so the two components differ in frequency by $2\gamma H_o$. If $H_o >> H_L$, the cross-relaxation rate is vanishingly small, and can be ignored for our purposes. However, as will be discussed later, for powder samples H_o has some undesirable effects, so in practice a value of $H_o \sim H_L$ is often used.

We now consider the effect of spin-lattice relaxation, which occurs on a time scale T_1. After the rf is swept through the low frequency component of the transition, the population difference in the +m manifold decays back to its thermal equilibrium value. Ignoring cross-relaxation, the -m manifold retains its equilibrium value during this decay. The magnitude of the magnetization associated with the -m transition is thus larger than that of the +m, and the signal will extend below the baseline. The simulated lineshapes for various sweep rates are presented in Figure II.6. The lineshapes were calculated by numerically approximating the integral

$$S(\omega) = \int_0^{\omega} (g_1(\omega') + g_2(\omega'))e^{-(\omega - \omega')/\kappa T_1}\, d\omega' \qquad \text{II-18}$$

where $g_1(\omega)$ and $g_2(\omega)$ are Gaussians describing the absorption lineshapes of the two components. Note that $g_1(\omega)$ and $g_2(\omega)$ have opposite signs, appropriate to the different sign of m in the two manifolds.

The last factor affecting the observed lineshape is the use of powder samples. The effect is strongly dependent on the sample parameters as well as the experimental conditions, and is difficult to

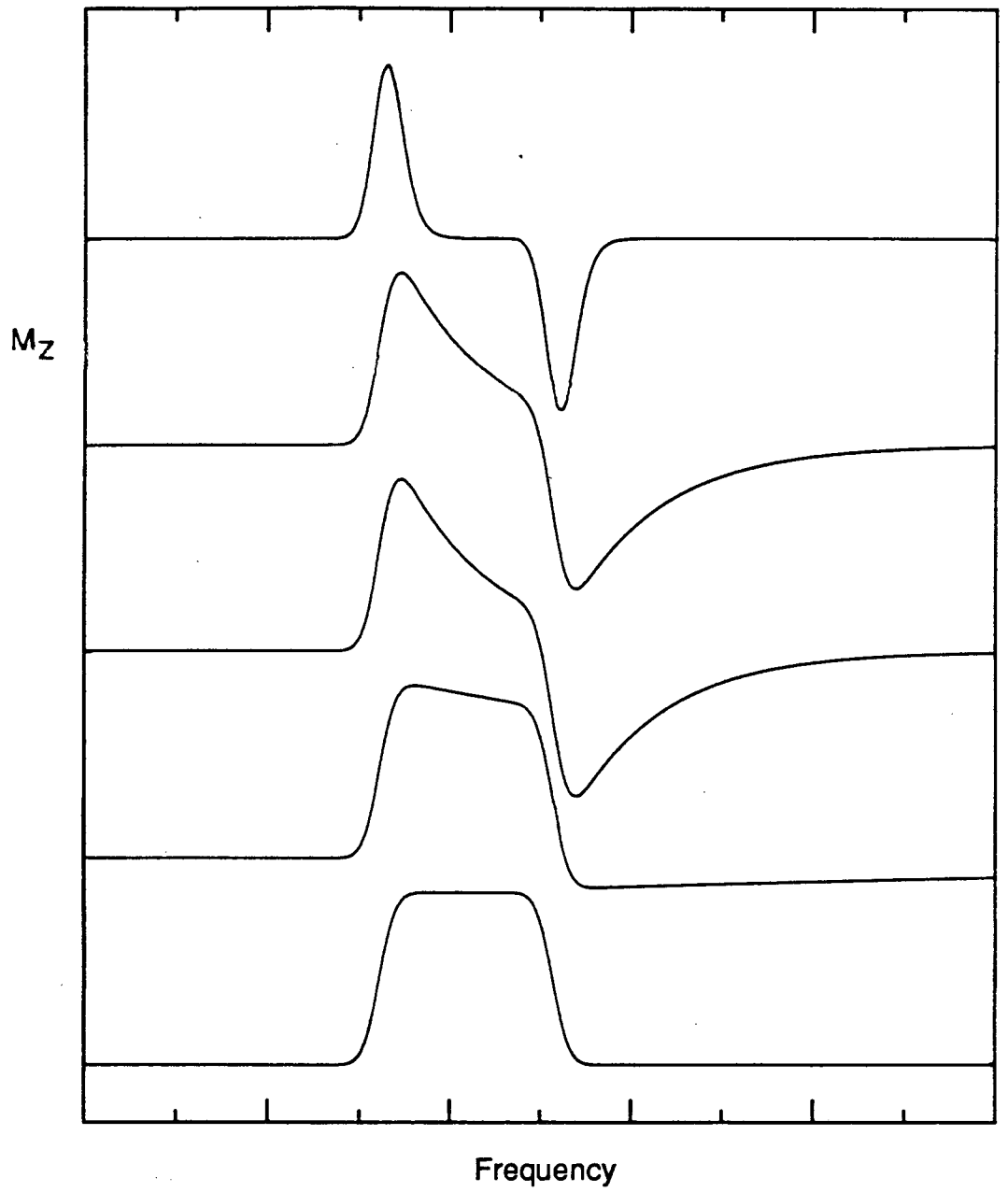

Figure II.6: Simulated z-axis cw NQR lineshapes for a quadrupolar spin system, as a function of the sweep rate of the rf field. The lower traces correspond to faster sweeps.

evaluate even approximately. However, the most important NQR applications of the SQUID spectrometer will involve powder samples, since single crystal samples are readily amenable to study by conventional NMR techniques.[9] The purpose of this section is to point out the general factors to be considered for z-axis NQR of powder samples. We consider a powder sample one which consists of small domains, oriented randomly with respect to the laboratory axis system. Each domain is assumed to be perfectly crystalline, so that all the nuclei within each domain have the same quadrupolar splitting. In a zero-field NQR experiment, all the nuclei in the sample have the same resonance frequency, and the only source of line broadening will be the previously discussed dipolar interaction. The application of a small magnetic field introduces additional broadening as will be described below.

From Equation (II-3′), using degenerate first-order perturbation theory, one arrives at a simple result for the energies of the ±3/2 states; these states are shifted by $\Delta E(\pm 3/2) = \mp m\gamma\hbar H_o \cos\theta$, and m is still a good quantum number.[1] The magnetic field is oriented at an angle θ with respect to the quadrupolar interaction, which is assumed to have cylindrical symmetry. However, for the ±1/2 levels the situation is not quite as simple. The I_x and I_y terms in $\mathcal{H}_Z'$ mix these levels, resulting in two states

$$|+\rangle = \sin\alpha|+1/2\rangle + \cos\alpha|-1/2\rangle$$
$$|-\rangle = -\cos\alpha|+1/2\rangle + \sin\alpha|-1/2\rangle \qquad \text{II-19}$$

where

$$\tan\alpha = \left(\frac{f + 1}{f - 1}\right)^{1/2} \text{ and } \quad f = (1 + (I + 1/2)^2\tan^2\theta)^{1/2} \quad .$$

Now for these states m is no longer a good quantum number, so transitions from either of the 3/2 states to either of these two states are allowed. The energy shifts of these mixed states are given by $\Delta E(\pm) = \mp(f/2)\hbar\gamma H_o\cos\theta$.

Now we return to the problem of the shape and amplitude of the powder lineshape. The functions $g_i(\omega)$ used in Equation (II-18) must now be replaced by the corresponding powder lineshape function, which depends on the dc and rf field strengths,

$$g_i(\omega,H_o,H_1) = \int_0^{\pi}\int_0^{2\pi} \frac{1}{4\pi} g_i(\omega,\theta)\Gamma(\theta)\Xi(\theta,H_1)T(\theta,H_o)\rho d\phi\sin\theta d\theta . \quad \text{II-20}$$

The functions $g_i(\omega,\theta)$ have the same width as the $g_i(\omega)$, but are centered at $\omega_Q \pm \omega_o f\cos\theta$. The induced magnetization of the spin system appears along the quadrupolar symmetry axis, while the SQUID measures the component along the laboratory z-axis. Thus the signal from a crystallite with polar angle θ is reduced by a factor $\Gamma(\theta) = \cos\theta$. The term $\Xi(\theta,H_1)$ reflects the fact that only the projection of the rf orthogonal to the quadrupolar z-axis is effective in exciting transitions. The effective rf field available for inducing transitions is $H_{1,eff} = H_1\cos\theta$. The function $\Xi(\theta,H_1)$ then describes the signal height as a function of the effective rf strength, and has the form $\Xi(\theta,H_1) \sim (1 - \exp(-H_{1,eff}/H_1^o))$, where H_1^o is a characteristic rf strength depending on the sample parameters and sweep rate. An

experimental measurement of the function $\Xi(\theta,H_1)$ is presented in Chapter IV. The dc field is less effective in preventing cross relaxation when the quadrupole z-axis is tilted with respect to the lab z-axis, and $T(\theta,H_o)$ accounts for this. The effective field for splitting the two transitions becomes $H_{o,eff} \sim H_o\cos\theta$. As this effective field approaches the local field, cross relaxation can no longer be neglected and will reduce the signal intensity and distort the signal shape. The functional form is $T(\theta,H_o) \sim (1 - \exp(-H_{o,eff}/H_L))$, and the sweep rate and zero-field cross relaxation rate affect the overall magnitude of $T(\theta,H_o)$.

The magnetic field may also broaden the line, since the splitting due to the field is dependent on the orientation. If the distribution of quadrupolar splittings is negligible, and we have $H_o > H_L$, the linewidth will be on the order of $2\gamma H_o$. Thus in some cases it is better to use $H_o \sim H_L$ to minimize the linewidth while still maintaining signal intensity. For glassy or disorganized samples, where a large variation of quadrupolar splittings is expected, the value of H_o is not as critical. The contribution to the linewidth from H_o can always be estimated if the field strength and the gyromagnetic ratio of the observed nucleus is known. However, it is most reliable to compare experiments at different fields if linewidth information is desired.

Finally, the factor ρ accounts for the reduced filling factor of the powder sample as compared with a single crystal. For particles of approximately spherical shape $\rho \sim 1/2$. This value is independent of the particle size, as long as the sample is made up of a large number of particles.

We now consider the application of this experimental technique to

quadrupolar nuclei with spin other than 3/2. The simplest extension is to spin 5/2 nuclei. The (±3/2,±1/2) transition behaves similarly to the spin 3/2 case, except of course only about half of the spin 5/2 nuclei participate in this transition. The (±5/2,±3/2) transition is simpler than the (±3/2,±1/2) transition, since neither the ±3/2 states or the ±5/2 states are mixed by the dc magnetic field. A summary of the magnetization at each stage in the sweep through resonance is presented in Table II-1. The results are based on a sweep with a saturating rf field, from low to high frequency.

Table II.1: Expectation Values for Mz During Saturation

	I = 3/2	I = 5/2
Thermal Equilibrium	$5\,\frac{N\gamma^2\hbar^2}{4kT}\,H_o$	$\frac{35}{2}\,\frac{N\gamma^2\hbar^2}{6kT}\,H_o$
After Saturating (+3/2,+1/2)	$\frac{N\gamma\hbar}{4kT}\left(\frac{1}{4}\,e^2qQ + \frac{9}{2}\,\hbar\gamma H_o\right)$	$\frac{N\gamma\hbar}{6kT}\left(\frac{3}{40}\,e^2qQ + 17\hbar\gamma H_o\right)$
After Saturating (+5/2,+3/2)		$\frac{N\gamma\hbar}{6kT}\left(\frac{6}{40}\,e^2qQ + 17\hbar\gamma H_o\right)$
After Saturating Both Components	$4\,\frac{N\gamma^2\hbar^2}{4kT}\,H_o$	$\frac{33}{2}\,\frac{N\gamma^2\hbar^2}{6kT}\,H_o$

The final magnetization of the spin 5/2 system is the independent of whether the (±3/2,±1/2) transition or the (±5/2,±3/2) transition was observed. Sweeping from high to low frequency changes the sign of the quadrupolar term but does not affect the Zeeman term. Under favourable conditions this effect may allow the determination of γ, permitting the assignment of unidentified resonances to specific isotopes in the sample. Successful experiments have been carried out on both 3/2 and 5/2

spin nuclei. The extension to higher half integral spin is straightforward.

Less obvious is the extension to integer spin nuclei. The simplest of these, spin 1, we consider here. The Hamiltonian in zero field, Equation (II-1), has eigenstates, for $\eta = 0$, of $|+1\rangle$, $|0\rangle$, and $|-1\rangle$.[1,10] These states are also the eigenstates of I_z, with the respective eigenvalues +1, 0, and -1. When $\eta \neq 0$, the eigenstates become

$$\begin{aligned} |+\rangle &= \tfrac{1}{\sqrt{2}}(|+1\rangle + |-1\rangle) \\ |-\rangle &= \tfrac{1}{\sqrt{2}}(|+1\rangle - |-1\rangle) \\ |0\rangle &= |0\rangle \quad . \end{aligned} \qquad \text{II-21}$$

These eigenstates are exact, even for very small values of η, and also in the limit $\eta = 0$. As is easily seen, $\langle I_z \rangle = 0$ for spins in either of these three states, so moving spins from one state to another will produce no observable magnetization. Since this basis is correct for arbitrarily small values of η, and one expects that very few samples have η identically zero, it first appears that the experiment will not work for most spin 1 systems. However, the $|+1\rangle$, $|0\rangle$, $|-1\rangle$ basis, in which a signal is predicted, is approximately correct for small η. To the extent that this basis is correct, a signal will be observed. Jach presents a more quantitative argument of this point.[10] Although no successful experiments using this technique have been carried out on spin 1 systems, an ideal test case is ^{14}N in solid N_2. The relatively high spin density, short spin-lattice relaxation time, convenient and well known quadrupolar splitting, and small or zero η make this an

excellent sample.[11]

In the final part of this section we consider the effect of various polarizations of the rf field. As first pointed out by Dean,[12] and later discussed fully by Weber and Hahn,[5] the two components making up the transition of the spin 3/2 system react differently to circularly polarized rf fields. In particular, either direction of circular polarization will excite only one of the two components. A series of experiments have been carried out on the SQUID spectrometer which exploit this effect, and will be discussed in Chapter V. Linearly polarized rf fields are composed of two counter-rotating circularly polarized fields of equal amplitude, so they excite both transitions equally. The polarization dependence of transitions springs directly from the fact that the dominant Hamiltonian is proportional to I_z^2, and is not observed in NMR experiments where the main Hamiltonian is proportional to I_z.

REFERENCES

1. T. P. Das and E. L. Hahn, Solid State Physics, edited by F. Seitz and D. Turnbull, Suppl. 1, (Academic Press, New York, 1958).

2. R. R. Ernst, G. Bodenhausen, and A. Wokaun, Principles of Magnetic Resonance in One and Two Dimensions (Clarendon Press, Oxford, 1987), and references therein.

3. E. P. Day, Phys. Rev. Lett. 29, 540 (1972).

4. M. Goldman, Spin Temperature and Nuclear Magnetic Resonance in Solids (Clarendon Press, Oxford, 1970).

5. M. J. Weber and E. L. Hahn, Phys. Rev. 120, 365 (1960).

6. T. Jach, Appl. Phys. Lett. 28, 49 (1976).

7. A. Abragam and K. Kambe, Phys. Rev. 91, 894 (1953).

8. a) N. Bloembergen, S. Shapiro, P. S. Pershan, and J. O. Artman, Phys. Rev. 114, 445 (1959);
   b) D. Suter and R. R. Ernst, Phys. Rev. B 32, 5608 (1985).

9. See, for example,
   a) H. E. Petch and K. S. Pennington, J. Chem. Phys. 36, 1216 (1962);
   b) S. Hafner and M. Raymond, Am. Mineral. 52, 1632 (1967).

10. T. Jach, Ph.D. Thesis, Stanford (1975).

11. J. R. Brookeman, M. M. McEnnan, and T. A. Scott, Phys. Rev. B 4, 3661 (1971).

12. C. Dean, Phys. Rev. 96, 1053 (1954).

III. OPERATING PRINCIPLES OF THE DC SQUID DETECTOR

A. Physical Overview

This section presents a general physical picture of how the dc SQUID acts as a magnetic flux to voltage converter. A schematic of a dc SQUID, consisting of a superconducting loop broken by two Josephson junctions, is given in Figure III.1. A junction may be a thin layer of insulating material separating the superconductors, or merely constrictions in the superconductor.[1,2] Typical dimensions of the SQUID are on the order of millimeters.[3,4] The combination of the SQUID and its associated preamplifiers, feedback circuitry, filters, etc., will be referred to as the SQUID system. Thus, for example, the voltage across the SQUID is not to be confused with the output voltage of the SQUID system.

During operation of the SQUID a fixed bias current is forced through the loop. Part of the current flows through the junctions as a supercurrent, meaning that no voltage is developed by electron flow, while the rest flows as a normal current. According to the conventional picture of superconductivity, the supercurrent is made up of electron pairs, while the normal current consists of individual electrons.[5,6] The voltage across the SQUID is proportional to the fraction of the bias current that flows as normal current. The fundamental operating principle of the SQUID is that the total supercurrent depends on the magnetic flux threading the loop. This arises because an electron pair accumulates a phase shift, proportional to the flux through the SQUID

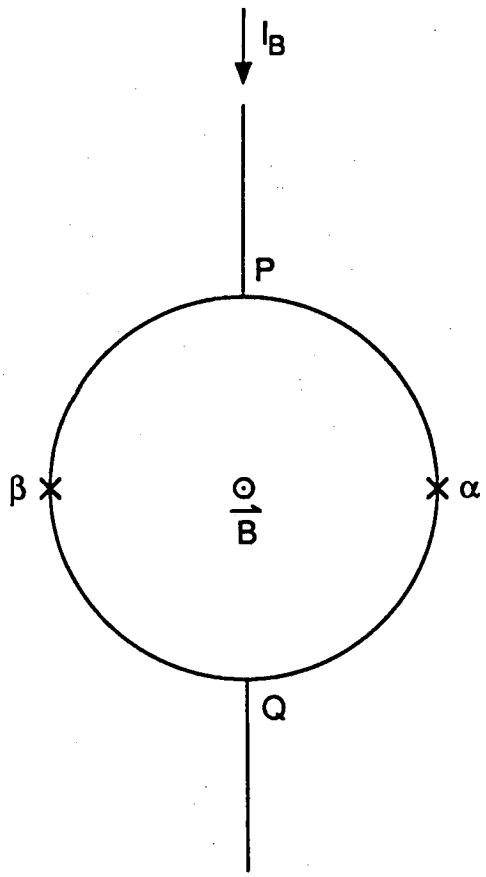

Figure III.1: A schematic representation of a dc SQUID. Electron pairs tunneling across the Josephson junctions (represented by x's) accumulate a phase which depends on the magnetic flux threading the loop. Interference effects between the currents through the two junctions permits a measurement of the flux.

loop, as it traverses a junction. In the idealized case, electron pairs passing through junction α experience a phase shift equal in magnitude but opposite in sign to the phase shift of electron pairs passing through junction β. When the two supercurrents arrive at point Q with a phase difference of $(2n + 1)\pi$ radians, they exhibit complete destructive interference and the total supercurrent is zero. All the bias current must travel as normal current in this case, and the voltage across the SQUID is at its maximum. If the supercurrents have a phase difference of $2n\pi$, they constructively interfere, minimizing the voltage across the SQUID. The voltage across the SQUID does not vanish completely however, since the bias current exceeds the maximum supercurrent through the two junctions in parallel. Thus the voltage across the SQUID is a periodic function of the flux threading the loop. Most SQUID systems operate in the flux-locked mode, using the SQUID itself as a null detector.[7] In this mode, the output voltage of the system is proportional to the current required to keep the total flux through the SQUID at a fixed level. These systems exhibit a linear response to the flux through the loop. A discussion of the key equations describing the quantum interference effect in a dc SQUID follows. The techniques used for transferring magnetic flux from a sample to the SQUID are summarized in Section IIIC. A qualitative discussion of the flux-locked mode of operation is found in Section IIID.

B. Key Equations Describing the dc SQUID[1,8-12]

According to the BCS theory of superconductivity, all the electron

pair wavefunctions within a superconducting structure are phase coherent.[5] If two superconductors are placed in close proximity, there will be some overlap of the electron wavefunctions corresponding to the two superconductors. There is a finite probability that electron pairs will tunnel between the superconductors, so the phases of electron pairs in the two superconductors will be related. This situation is represented in Figure III.2. The amplitude of the supercurrent, due to the tunneling pairs, depends sinusoidally on the phase difference across the junction,

$$j_s = j_1 \sin(\delta(t)) \qquad \text{III-1}$$

where

$$\delta(t) = \delta(0) + \frac{2e}{\hbar}\int_0^t V(t')dt' \quad . \qquad \text{III-2}$$

The $\delta(0)$ term in Equation (III-2) refers to a constant phase difference and is of little interest to us. The second term, in which V(t) is the voltage across the junction and e the electronic charge, induces a time dependence in δ. For a fixed voltage V, the supercurrent oscillates at the Josephson frequency,

$$\omega = \frac{2eV}{\hbar} \qquad \text{III-3}$$

where ω = 486 MHz for a voltage of one microvolt. This relationship has been used to obtain very accurate values of $e/\hbar$.[1] Since the SQUID typically is biased with a current of the order of microamps in excess

a) $\Psi_1 = \sqrt{\rho_1}\, e^{i\phi_1}$ $\Psi_2 = \sqrt{\rho_2}\, e^{i\phi_2}$

b) $\Psi_1 = \sqrt{\rho_1}\, e^{i\phi_1}$ $\Psi_2 = \sqrt{\rho_2}\, e^{i(\phi_1+\delta)}$

Figure III.2: a) Electron pair wavefunctions within any superconducting structure all have the same phase, which will be unrelated to the corresponding phase in another superconductor. b) If electron pair tunneling is possible between the superconductors, the wave functions will have a well defined phase relationship.

of the maximum supercurrent, and the effective resistance of the SQUID is on the order of ohms, a voltage of many microvolts will usually exist across the SQUID. Thus the supercurrent oscillates at gigahertz frequencies. Since the SQUID is current biased in normal operation, rather than voltage biased, the voltage will depend in turn on the supercurrent, and the expression for the frequency of the supercurrent in no longer simple. However, we need not be concerned with the detailed behavior of the frequency, since only the time-averaged value of the supercurrent is measured. Referring back to Figure III.1, the supercurrent arriving at Q has contributions from pairs travelling through each junction, and can be written

$$j_T = j_{1\alpha}\sin(\delta_\alpha(t)) + j_{1\beta}\sin(\delta_\beta(t)) \qquad \text{III-4}$$

where the supercurrent phases $\delta_\alpha(t)$ and $\delta_\beta(t)$ are given by Equation (III-2).

Equation (III-4) can be simplified by noting that moving an electron pair in a complete circuit around the SQUID must return the wavefunction's phase to the original value, modulo 2π. The phase shift generated by moving an electron pair from point 1 to point 2, in a magnetic field is

$$\delta = -\frac{2e}{\hbar}\int_1^2 \vec{A}\cdot d\vec{s} \quad . \qquad \text{III-5}$$

In this term $\vec{A}\cdot d\vec{s}$ is the component of the vector potential along the path followed by the electron pairs. We use this expression to determine the effect of moving the pairs through the vector potential inside the

superconducting arms of the SQUID. At first it may seem surprising that a vector potential exists in the interior of the superconductor, since it is well known that a magnetic field cannot penetrate deeply inside a superconductor. However, the magnetic field corresponds to the curl of $\vec{A}$, so a spatially invariant vector potential is not in contradiction with the absence of a magnetic field. This is the basis of the Aharanov-Bohm effect, which is very closely related to the interference within a SQUID.[13] Now the phase shift of the electron pair moving around the SQUID loop, neglecting the flux in the junctions, is

$$2\pi n = \delta_\alpha(t) - \delta_\beta(t) - \frac{2e}{\hbar} \oint_C \vec{A}\cdot d\vec{s} \quad . \qquad \text{III-6}$$

Stokes's theorem can be used to express the integral as

$$\frac{2e}{\hbar} \oint_C \vec{A}\cdot d\vec{s} = \frac{2e}{\hbar} \Phi_L \qquad \text{III-7}$$

where Φ_L is the magnetic flux threading the SQUID. Defining the flux quantum as $\Phi_o = h/2e = 2.07 \times 10^{-7}$ G·cm^2, and setting $n = 0$, allows Equation (III-4) to be written

$$j_T = j_{1\alpha}\sin(\delta_\alpha(t)) + j_{1\beta}\sin(\delta_\alpha(t) - 2\pi\Phi_L/\Phi_o) \quad . \qquad \text{III-8}$$

If the junctions are identical, so $j_{1\alpha} = j_{1\beta} = j_1$, we may write

$$j_T = 2j_1\sin(\delta_\alpha(t) - \pi\Phi_L/\Phi_o)\cos(\pi\Phi_L/\Phi_o) \qquad \text{III-9}$$

The voltage developed across the SQUID, for a bias current j_B exceeding the total critical current $2j_1$, is proportional to the difference

between the bias current and the supercurrent,

$$V(t) = R\left[\frac{j_B}{2} - 2j_1 \sin(\delta_\alpha(t) - \pi\Phi_L/\Phi_o)\cos(\pi\Phi_L/\Phi_o)\right]. \quad \text{III-10}$$

The constant of proportionality, R, is the effective resistance of one junction. As mentioned previously, $\delta_\alpha(t)$ oscillates at gigahertz frequencies, so only a time-averaged value of V(t) will be observed by a narrowband detector. Since $\delta_\alpha(t)$ depends on V(t), the time average of V(t) is not simply zero.[12] Using Equation (III-2) for $\delta_\alpha(t)$, and integrating over one period of $\delta_\alpha(t)$, yields the time-averaged voltage

$$\bar{V} = R(j_B^2 - \bar{j}_T^2)^{1/2} \quad \text{III-11}$$

where the time-averaged supercurrent, $\bar{j}_T$, is

$$\bar{j}_T = 2j_1\left|\cos(\pi\Phi_L/\Phi_o)\right| \quad . \quad \text{III-12}$$

Plots of the behavior of $\bar{V}$ as a function of Φ_L are given in Figure III.3. In practice, the behavior of Equation (III-11) is modified by many effects not considered here, including non-identical junctions, self-induced flux in the SQUID, noise, etc.[7-9,11,12] The observed function is smoothed to resemble a sine wave, as shown in the experimental flux-voltage curve in Figure III.3(c). However, as will be described in Section IIID, the response of a flux-locked SQUID is almost independent of the shape of the $\bar{V}$ versus Φ_L curve, as long as the curve is periodic.

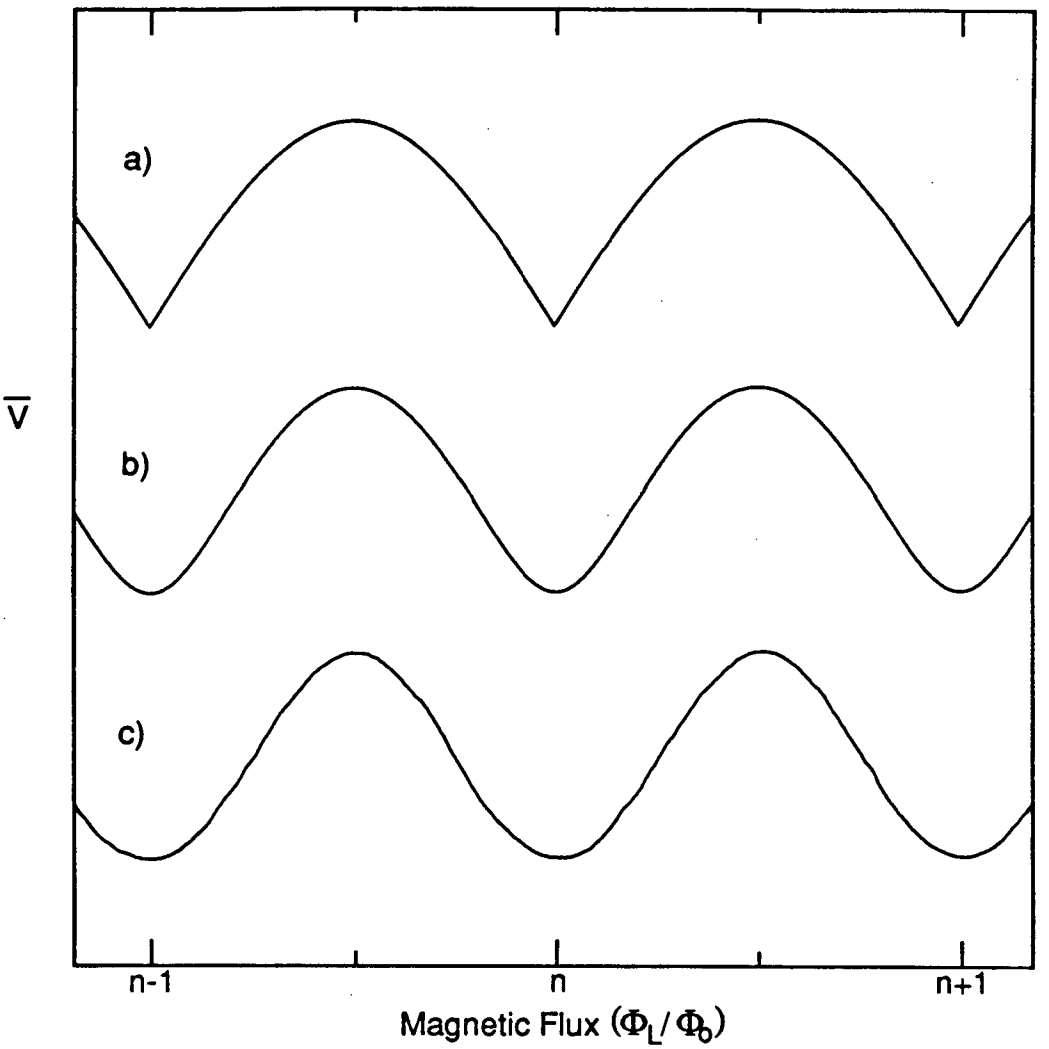

Figure III.3: a) A calculation of the time averaged voltage across the SQUID as a function of the total flux threading the loop, from Equations (III-11) and (III-12). The bias current is set equal to the total maximum supercurrent, $j_B = 2j_1$. b) As in a), but with $j_B = 2.12j_1$. c) The experimental flux-voltage curve.

C. Pickup Coil Assembly

Now we consider the problem of coupling the flux one wants to measure into the SQUID. For some applications, such as measurements of the Earth's magnetic field, for which the SQUID has been widely used, the solution is straightforward.[14] In the simplest arrangement an unshielded SQUID is oriented orthogonally to the field, and the flux is directly coupled into the loop. For applications requiring measurement of the magnetization of small samples, in principle one could simply place the sample directly inside the SQUID loop. This method is not particularly satisfactory however, because modern SQUIDs often have a loop that is prohibitively small, and shielding of external fields is compromised in an arrangement that allows easy changing of the sample. In addition, it is often desirable to have the sample at a different temperature than the SQUID, or to have the sample in a large magnetic field while the SQUID is in low or zero field. A better arrangement is to use some type of flux transformer to transfer flux from the sample to the SQUID.[12]

A variety of flux transformers have been utilized. Clarke and co-workers have used a conventional tuned circuit, containing a resistive element, for work in a narrow bandwidth at comparatively high frequency (~30 Mhz).[15-18] The time dependent magnetization induces a voltage in a coil surrounding the sample, according to Faraday's Law of Induction. The voltage generates a current in a coil coupled to the SQUID, producing flux in the SQUID. This circuit has the advantage that the current is amplified by a factor on the order of Q, the quality factor

of the circuit, and that only noise within the bandwidth of the circuit is coupled into the SQUID. However, this input circuit is not suitable for wide band, low frequency work for two reasons. The high Q of the circuit restricts the bandwidth of the circuit to a narrow range, so extensive retuning, coupled with piecewise acquisition, is required to detect with a large bandwidth. The other problem is that the induced voltage depends linearly on the rate of change of the magnetization, so low frequency signals produce less voltage. The solution usually employed is to use a superconducting pickup circuit.

This circuit consists of two superconducting coils connected by superconducting wire, as shown in Figure III.4. One coil, often called the coupling coil, is coupled to the SQUID and the other, the pickup coil, to the sample. The operating principle for this type of pickup circuit is simple; the total flux enclosed within a closed superconducting loop is fixed. If the magnetization of the sample changes, the flux produced in the pickup coil changes. In response, a current is induced in the pickup coil which generates just enough flux to cancel the change in flux from the sample. Since the pickup coil and coupling coil are part of a continuous loop, this induced current also passes through the coupling coil, producing flux through the SQUID. This input circuit has a frequency response extending from megahertz frequencies down to dc. However, as in all flux transformer circuits, only a fraction of the flux generated by the sample is delivered to the SQUID. Since this is a critical feature in determining the ultimate sensitivity of the SQUID system, it is worthwhile to consider the design of the pickup circuit in more detail.

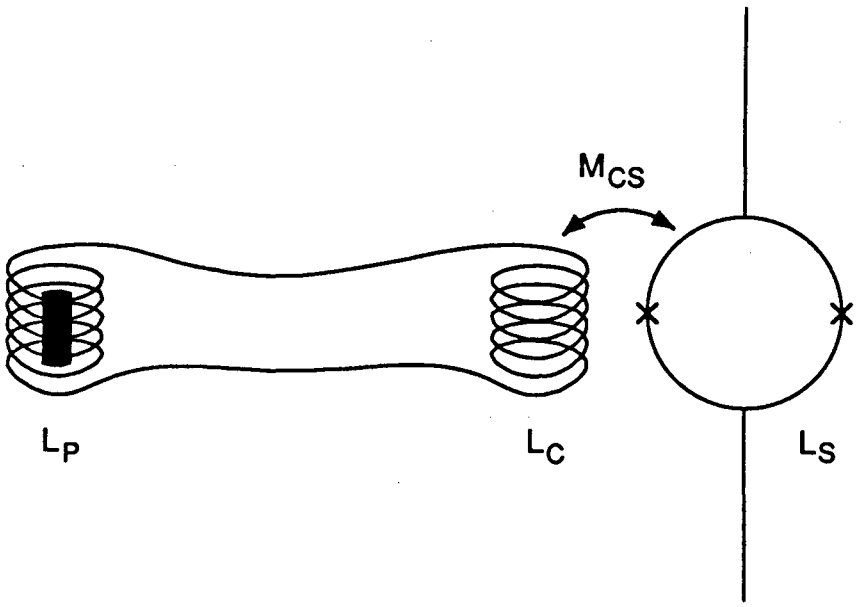

Figure III.4: The pickup coil and the coupling coil form a closed superconducting loop, which transfers flux from the sample to the SQUID. The coupling coil is coupled to the SQUID with a mutual inductance M_{cs}.

If the sample generates a magnetization M_a, the flux generated in the pickup coil, assuming a filling factor of unity, is

$$\Phi_p = 4\pi M_a \pi r_p^2 N_p \qquad \text{(cgs)} \qquad \text{III-13}$$

where r_p is the radius of the pickup coil, and N_p is the number of turns in the pickup coil. The induced current in the pickup coil is then

$$I_p = \frac{\Phi_p}{L_p + L_c} \qquad \text{III-14}$$

where L_p and L_c are the inductances of the pickup coil and coupling coil respectively. If appreciable stray inductance in the circuit exists, it should be added to the other terms in the denominator; i.e. the denominator is the sum of all the inductances in the loop. The flux coupled into the SQUID itself will depend on the mutual inductance between the coupling coil and the SQUID, M_{cs}, according to

$$\Phi_s = I_p M_{cs} \quad . \qquad \text{III-15}$$

Combining Equations (III-13) to (III-15) we obtain the change in flux through the SQUID as a function of the magnetization of the sample,

$$\Phi_s = \frac{M_{cs}}{L_p + L_c} (4\pi^2 M_a r_p^2 N_p) \quad . \qquad \text{III-16}$$

Now the primary consideration in designing a pickup coil is to optimize Φ_s with respect to M_a. This matter has been discussed in the literature, with the conclusion that, for a given sample size, the maximum signal is obtained with $L_p = L_c$.[4,19] If the sample size can be varied the problem

becomes more complex, and numerical simulations may be required.[20] A discussion of the practical details of optimizing Equation (III-16) is deferred until Section IVA.

D. SQUID Readout

This section describes in qualitative terms the principles and techniques used to convert the voltage across the SQUID to a useful output voltage.[2,4,21]

In general, SQUID systems are designed to use the full low frequency sensitivity of the SQUID, which extends down to dc. The problem with low frequency measurements is that the system noise power, which is white at high frequencies, has a 1/f dependence at low frequencies. For most SQUID systems the 1/f contribution dominates the system noise below a frequency on the order of one hertz. Measurements at far lower frequencies are often of interest. The conventional solution to reduce the 1/f noise during these low frequency measurements is to use signal modulation combined with lock-in detection.

The principle of the technique, as it applies to the SQUID, is represented in Figure III.5. A modulation coil, in addition to the coupling coil, is flux-coupled to the SQUID. It is used to apply a flux, Φ_m, to the SQUID with amplitude of about one half of a flux quantum, at a modulation frequency ν_m. The voltage across the SQUID will consist of a component at frequency ν_m and a component at $2\nu_m$. The relative amplitude of each component is determined by the flux through the SQUID, modulo Φ_o. If the sample flux is $(n + 1/4)\Phi_o$, the component at ν_m will

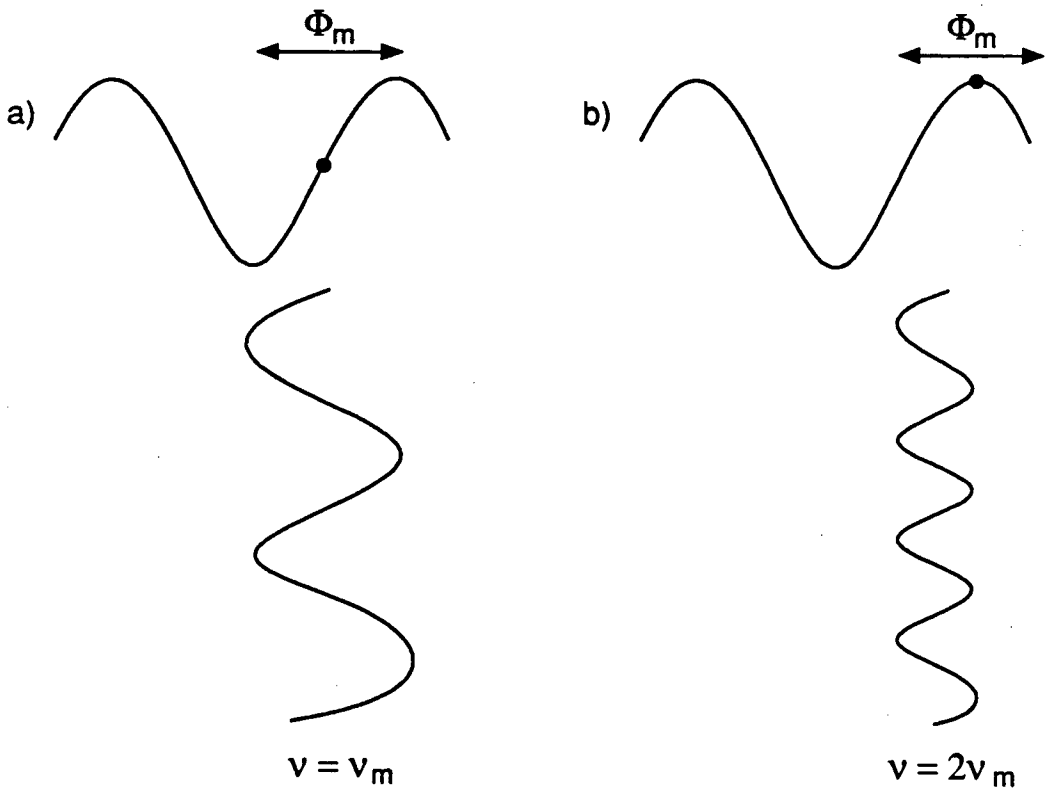

Figure III.5: The flux through the SQUID is the sum of a modulation flux, $\Phi_m = (\Phi_o/2)\sin\nu_m$, and the flux from the sample, Φ_s. a) If $\Phi_s = (n + 1/4)\Phi_o$, the modulation produces a voltage across the SQUID at frequency ν_m. b) If $\Phi_s = (n + 1/2)\Phi_o$, the voltage across the SQUID appears at $2\nu_m$, twice the modulation frequency.

be a maximum and the component at $2\nu_m$ will vanish. For a sample flux of $(n + 1/2)\Phi_o$, the component at $2\nu_m$ is maximized, while the ν_m component is zero. When the sample flux reaches $(n + 3/4)\Phi_o$, the component at ν_m again has the maximum amplitude, but its phase is shifted by 180^o with respect to the situation when $\Phi_s = (n + 1/4)\Phi_o$. Thus, if a phase sensitive detector is used, the amplitude of the ν_m component is a direct measure of the flux from the sample. This discussion has simplified the situation slightly in that the component at ν_m actually contains higher harmonics at $(2n + 1)\nu_m$. The relative amounts of these harmonics depends on the shape of the flux-voltage curve and on the modulation function. Likewise, the $2\nu_m$ component contains harmonics at $2n\nu_m$. These higher harmonics do not play any significant role in the operation of the system. In practical SQUID systems, the SQUID is connected to a circuit tuned to the modulation frequency, ν_m. The voltage in the circuit, which is approximately the voltage across the SQUID multiplied by the Q of the circuit, is mixed with a reference frequency ν_m to give a dc output. This output voltage is related to the sample flux by $V \sim \sin(2\pi\Phi_s/\Phi_o)$.

If the sample flux oscillates at ν_s, the voltage in the tuned circuit appears at $\nu_m \pm \nu_s$, and mixing down with ν_m regenerates the component at ν_s. Immediately we see that, for a given ν_m, a low Q circuit is necessary to measure frequencies at a significant fraction of the modulation frequency.

The detection system as described up to this point has one principal weakness: the mixed down voltage from the SQUID is a periodic, rather than linear, function of the sample flux. Thus the output voltage

is proportional to the sample flux only when the sample flux generates much less than one flux quantum in the SQUID i.e. in the limit as $\sin(x) \sim x$. To extend the linear dynamic range of the system, negative feedback is used with the SQUID as the null detector. The mixed down output is inverted and fed back as a flux to the SQUID. This feedback exactly cancels the flux generated in the SQUID by the sample, so the flux at the SQUID is held at some constant value. The voltage applied to the feedback coil, usually also used as the modulation coil, is then linearly proportional to the sample flux, even for very large signals. This voltage, after passing through additional filters, is referred to as the output voltage of the SQUID. The linear response of the detection system is independent of the detailed shape of the flux-voltage curve, provided that it is periodic in flux.

This modulation and feedback arrangement presents one restriction that is very important for magnetic resonance applications. Frequencies greater than the modulation frequency cannot be detected, and the modulation frequency is limited by phase shifts in the feedback current. The feedback flux has to be 180^{o} out of phase with the sample flux to prevent distortions of the signal. Phase shifts are caused by unavoidable stray reactances in the detection and feedback circuits, and become worse at higher frequencies. The modulation frequency is generally limited to a few hundred kilohertz or less, but one flux-locked system has been reported with a bandwidth of 5 to 10 MHz.[22] Conventional pulsed NMR experiments require the measurement of a magnetization oscillating at the energy level splitting frequency, so pulsed NMR measurements with a flux-locked SQUID will be restricted to

low frequencies. There seems to be no practical way to mix down the signal within the pickup loop. However, using the z-axis magnetic resonance technique described in Chapter II, this frequency restriction is completely eliminated.

Another important characteristic of the SQUID which appears from the previous discussion is its sensitivity to electromagnetic interference. We consider two types of interference: a low-level, high-frequency periodic interference and a sharp transient interference. The low-level interference, which is assumed to have a frequency much greater than the modulation frequency, modulates the flux-voltage curve. This modulation reduces the measured amplitude of the flux-voltage curve. The effective slope of the curve is thereby reduced, increasing the noise level in the output. When the interference level corresponds to a flux modulation at the SQUID of one half of a flux quantum, the flux-voltage curve is averaged to zero. For slightly larger modulation amplitudes, the curve will reappear with the opposite sign. We have measured the amplitude of the flux-voltage curve as a function of the amplitude of a sinusoidal interference, and found it behaves roughly as a sinc function. Since the effects of interference cannot be filtered out of the output voltage, interference at any frequency above the modulation frequency must be kept out of the SQUID. The second type of interference, the transient, causes the flux in the SQUID to change faster than the feedback circuit is able to follow. The system loses lock, and in general the new lock point will differ from the old one by an integer number of flux quanta. Thus the dc offset in the output will range over a number of discrete values, differing by a voltage

corresponding to a change of one flux quantum through the SQUID. This phenomenon may be useful in testing the system, since it is provides a direct measure of the overall system gain. However, it presents a problem during most magnetization measurements if the SQUID is not carefully shielded. A discussion of shielding techniques is presented in Chapter IV.

REFERENCES

1. J. Clarke, Am. Jour. Phys. 38, 1071 (1970).

2. J. Clarke, Proc. IEEE, 61, 8 (1973).

3. F. Wellstood, C. Heiden, and J. Clarke, Rev. Sci. Instrum. 55, 952 (1984).

4. J. Clarke, W. M. Goubau, and M. B. Ketchen, J. Low. Temp. Phys. 25, 99 (1976).

5 J. Bardeen, L. N. Cooper, and J. R. Schrieffer, Phys. Rev. 106, 162 (1957); 108, 1175 (1957).

6. C. Kittel, Introduction to Solid State Physics (Wiley, New York, 1986).

7. J. Clarke in Superconductor Applications: SQUIDs and Machines, edited by B. B. Schwartz and S. Foner, (Plenum, New York, 1977).

8. A. Th. A. M. De Waele and R. De Bruyn Ouboter, Physica 41, 225 (1969).

9. D. E. McCumber, J. Appl. Phys. 39, 2503 (1968).

10. R. P. Feynman, R. B. Leighton, and M. Sands, The Feynman Lectures on Physics, Vol. 3 (Addison-Wesley, Reading, 1965).

11. R. C. Jaklevic, J. Lambe, J. E. Mercereau, and A. H. Silver, Phys. Rev. A 140, 1628 (1965).

12. M. Tinkham, Introduction to Superconductivity (McGraw-Hill, New York, 1975).

13. Y. Aharanov and D. Bohm, Phys. Rev. 115, 485 (1959).

14. J. Clarke, IEEE Trans. Magn. MAG-19, 288 (1983).

15. T. Sleator, E. L. Hahn, M. B. Heaney, C. Hilbert, and J. Clarke, Phys. Rev. Lett. 57, 2756 (1986).

16. T. Sleator, E. L. Hahn, C. Hilbert, and J. Clarke, Phys. Rev. Lett. 55, 1742 (1985).

17. C. Hilbert, J. Clarke, T. Sleator, and E. L. Hahn, Appl. Phys. Lett. 47, 637 (1985).

18. T. Sleator, E. L. Hahn, C. Hilbert, and J. Clarke, Phys. Rev. B 36, 1969 (1987).

19. J. H. Claassen, J. Appl. Phys. 46, 2268 (1975).

20. J. Knuutila, S. Ahlfors, A. Ahonen, J. Hällström, M. Kajola, O. V. Lounasmaa, V. Vilkman, and C. Tesche, Rev. Sci. Instrum. 58, 2145 (1987).

21. R. P. Giffard, R. A. Webb, and J. C. Wheatley, J. Low. Temp. Phys. 6, 533 (1972).

22. A. Long, T. D. Clark, R. J. Prance, and M. G. Richards, Rev. Sci. Instrum. 50, 1376 (1979).

IV. SQUID SPECTROMETER

A. Design Considerations

This section deals with some of the factors to be considered in designing a SQUID spectrometer. Many of these, such as easy sample changing, high sensitivity, and ease in assembly and disassembly, are common to other instruments, so will not be discussed at length. Others are peculiar to SQUID-based systems, and will be considered in more detail.

Sample changing is somewhat complicated with the SQUID system because the pickup coil and the SQUID must be kept at low temperature. Because of the large thermal mass of the probe assembly, it is undesirable to remove the probe from the helium bath during sample changing. Thus it is important to have a means of changing the sample while the probe is cold. The best filling factor is obtained with the coil wrapped directly around the sample, but of course this makes sample changing very difficult.

The versatility of a SQUID spectrometer is considerably increased if sample temperature variation is possible. However, if the pickup coil is to be kept at low temperature, this entails a dewar assembly within the pickup coil to hold the sample. In the simplest configuration, sealing the sample inside an evacuated glass tube containing a heater may be sufficient. A more convenient arrangement is a reentrant dewar inside the pickup coil, as has been successfully used both for SQUID NMR[1-3] and SQUID magnetic susceptibility measurements.[4-6] For many of

the experiments described here, the reduction in signal to noise ratio, due to the reduced filling factor, is unacceptable. In addition, raising the sample temperature to, say, liquid nitrogen temperature corresponds to a reduction in the signal by a factor of almost 20, due to the reduced Boltzmann factor.

Ease in assembly, and in particular dissassembly, has been a factor not heavily weighted in SQUID spectrometer design. The main reason for this has been the problem of vibration of the pickup coil. Often the pickup coil is located in a constant magnetic field eight or ten orders of magnitude larger than the magnetic field due to the sample. Microscopic movement of the pickup coil within this inhomogeneous field will result in changing flux through the pickup coil, and a corresponding change in the output voltage. Although increasing the homogeneity of the dc field is helpful, it is still necessary to pay close attention to the rigidity of the pickup coil with respect to the dc field. Many workers cast the entire coil assembly, consisting of pickup coils, dc field coils, and perhaps rf coils, in epoxy.[4,7,8] This arrangement is not amenable to experimentation with different geometries of pickup coils. We believe we have an arrangement which strikes a reasonable compromise between reducing vibrations and allowing easy dismantling of the coil assembly.

For us, the least satisfactorily solved design problem is that of filtering the SQUID input to prevent pickup of rf and high frequency noise. Although this problem is more severe in cw spectrometers than in pulsed spectrometers, even in pulsed arrangements high frequency noise can cause serious problems. We restrict this discussion to the problem

of operation in the cw mode. To get an idea of the magnitude of the problem, consider the amount of attenuation of the rf required. Typical cw magnetic resonance experiments require rf levels of about 10 mG or more. If this field is directly coupled into a pickup coil of 10 turns and 0.5 cm diameter, it generates about 5×10^5 Φ_o through the pickup coil ($1\ \Phi_o = 2.07 \times 10^{-7}$ G·cm^2). Assuming 2% of this is coupled into the SQUID, we get 10^4 Φ_o through the SQUID. As seen in Section IIID, high frequency modulation of the flux-voltage curve by only $\Phi_o/2$ destroys the gain of the SQUID completely. Lower modulation amplitudes result in increased noise levels. A modulation amplitude of $\Phi_o/5$ is probably the most that is acceptable. Thus we need an attenuation of the rf field of at least four orders of magnitude to operate the SQUID, and five or six orders would be desirable. Some of this attenuation is obtained by orienting the rf coil orthogonally to the pickup coil. Typically a factor of 100 to 1000 is possible here, if adjustable paddles are not used. The remaining attenuation must come from either shielding the pickup coil to prevent coupling to the rf coil, or putting some sort of filter in the pickup circuit to keep rf from reaching the SQUID. Both of these arrangements have been widely used, but both types of filters generate noise.

The shield in its simplest form is simply a highly conductive cylinder placed between the pickup coil and the rf coil.[9] The shield has some characteristic skin depth, δ, related to its conductivity, ρ, by

$$\delta = \left(\frac{2}{\mu_o \omega \rho}\right)^{1/2}. \qquad \text{IV-1}$$

An electromagnetic wave, with frequency ω, passing through the shield will be attenuated by a factor on the order $e^{-t/\delta}$, where t is the thickness of the shield. For example, a 0.1 mm thick high purity copper shield held at 4.2 K shields rf above about 250 Hz. However, the amount of noise generated by the shield is inversely related to its lower cutoff frequency. The shield has some resistance R to currents encircling it, and this resistance generates Johnson noise. The Johnson noise voltage for a shield at temperature T, recorded by a voltmeter with bandwidth B, is

$$V_n = (4kTRB)^{1/2} \qquad \text{IV-2}$$

The noise current, which is responsible for the flux noise, is $I_n = V_n/R$, so the flux noise increases as the resistance is lowered. A thicker shield, required to reduce the cutoff frequency of the shield, has lower resistance and therefore higher noise current. The flux noise through the shield is $\Phi_n = L_s I_n$, where L_s is the inductance of the shield.

Although this shield has been widely used, it has the serious drawback that the rf coils must be placed inside the shield, with the sample, while the pickup coil is outside the shield. Thus the filling factor is poor for this arrangement. In addition, variation of the shield cutoff frequency to optimize the signal to noise ratio for a particular experiment does not seem to be easily achievable.

The other method, using a filter in the pickup circuit, has neither of these drawbacks. The basis of this method is that a small shunt resistor, R_s, is placed in parallel with the coupling coil.[8,10]

This simple RL filter has a low frequency cutoff of

$$\nu = \frac{R}{2\pi}\left(\frac{L_p + L_c}{L_p L_c}\right) \quad . \qquad \text{IV-3}$$

The impedance of the resistor is fixed at R_s, while the impedance of the coupling coil, ωL_c, increases with frequency. Low frequency currents pass through the coupling coil, while currents at frequencies much above the cutoff frequency pass through the resistor. As with the shield, the resistor produces a flux noise inversely related to the resistance. More complex filters have been studied, and may prove useful in some circumstances.[11,12] In particular, putting a large capacitor in series with the shunt resistor may reduce the low frequency noise generated by the resistor, without compromising the filtering action.

Given that one wants to operate at a frequency ω_o, one must decide on a cutoff frequency that reduces rf interference, but does not produce an unacceptable amount of noise. Both the shield and the shunt resistor act as simple RL filters, reducing any transmitted current by 6 dB per octave, at frequencies well above the cutoff frequency. Thus it is important to place the low frequency cutoff as low as possible. In deciding on this frequency, ideally one should know not only the operating frequency, but also how the signal varies with the strength of the applied rf field. Since the signal strength as a function of rf amplitude varies from sample to sample, the best solution is to have the cutoff frequency adjustable from outside the cryostat.

Another important consideration in the SQUID spectrometer is the design of the pickup coil circuit. We assume that the coupling coil and

its mutual inductance with the SQUID is fixed, as in many, if not all, commercial sensors. If one is designing a SQUID spectrometer from scratch, then all the pickup coil parameters, with the possible exception of the wire diameter, can be taken as variable parameters. First one must decide whether to use a gradiometer coil,[13] made up of two nearly identical, oppositely-wound coils, or a single coil. Normally the sample is placed in only one of the gradiometer coils. The gradiometer has the advantage that large scale environmental effects, such as fluctuations in a homogeneous dc magnetic field, can be attenuated by two or three orders of magnitude. However, in addition to restricting the sample length, the flux transfer from the pickup coil to the SQUID will be reduced. This comes about because in order to maintain the matching condition $L_p = L_c$, the number of turns in each half of the gradiometer is reduced by a factor of $1/\sqrt{2}$, as compared with a single coil. Thus the maximum sensitivity to sample flux will be obtained with a single pickup coil, as long as large scale noise sources do not dominate the system noise.

To optimize the pickup coil requires maximizing the flux through the SQUID for a given flux generated by the sample. If the coupling coil and its mutual inductance with the SQUID are fixed, we can simplify the requirement to that of maximizing the current through the coupling coil, for a given flux change in the region of the pickup coil. Since the maximum flux transfer occurs with $L_p = L_c$, the only parameter left is the radius of the pickup coil.[16,17] From Equation (III-16), it is apparent that the signal will increase with a larger pickup coil, if the sample size is increased correspondingly. Assuming $L_p \propto r_p N_p^2$, the flux

through the SQUID will increase approximately as $r^{3/2}$, for a given sample magnetization.

Of course there are also other factors to be considered in designing a pickup coil. Larger pickup coils will generally result in better filling factors, since wall thicknesses of sample containers and coil forms usually will not depend strongly on diameter. However, the larger dc and rf coils required for larger pickup coils require more power to generate a given field strength. Also, for expensive, toxic, or highly reactive samples it is preferable to keep the samples small. If superconducting shielding around the pickup coil region is used, the shield diameter should be much larger than the pickup coil diameter. This is because the shield distorts the flux lines, forcing some of the return flux lines through the pickup coil. Calculations of this effect have been carried out by Osterman and Williamson.[18] Since the maximum shield diameter is limited by the cryostat inner diameter, this effect may impose an upper limit on the size of the pickup coil. Incidentally, this flux distortion by nearby superconductors could be used by a clever designer to increase the signal from short samples, or those with a diameter much smaller than the pickup coil diameter.

We conclude this discussion of design considerations with a brief discussion of suitable materials to be used for probe construction in the vicinity of the pickup coil. Clearly one wants to avoid materials that give a magnetic resonance signal that can be confused with signals from the sample. One must also consider the possibility that the construction materials generate noise that can be detected by the SQUID. Day and others have dealt with this matter quite thoroughly, so this

will be only an introduction to the problem.[5,17] Many materials exhibit a temperature dependent electron paramagnetism in magnetic fields. Magnetic flux generated by these materials can couple, very strongly in some cases, to the pickup coil. So long as the magnetization is constant, this flux only shifts slightly the comparitively large dc field in which the pickup coil is immersed. However, small temperature fluctuations may cause variations of this flux, with an accompanying increase in noise in the output of the SQUID. As a general rule, non-superconducting metals should be kept out of the sample region to reduce this problem. Nuclear paramagnetism has also been considered by Day, and he concludes it may be a problem.[17] To reduce the effects of both electron and nuclear paramagnetism, it is important to hold the probe temperature as stable as possible.

B. Overview

An overview of the apparatus is shown in Figure IV.1. A copper mesh Faraday cage protects the SQUID from high frequency interference. The SQUID feedback unit is located inside the cage, and all other electronics are outside. The output voltage from the SQUID control unit passes through a low pass filter before going to either the chart recorder or computer. A two-channel rf source, one channel of which also goes to a frequency counter, powers the rf coils.

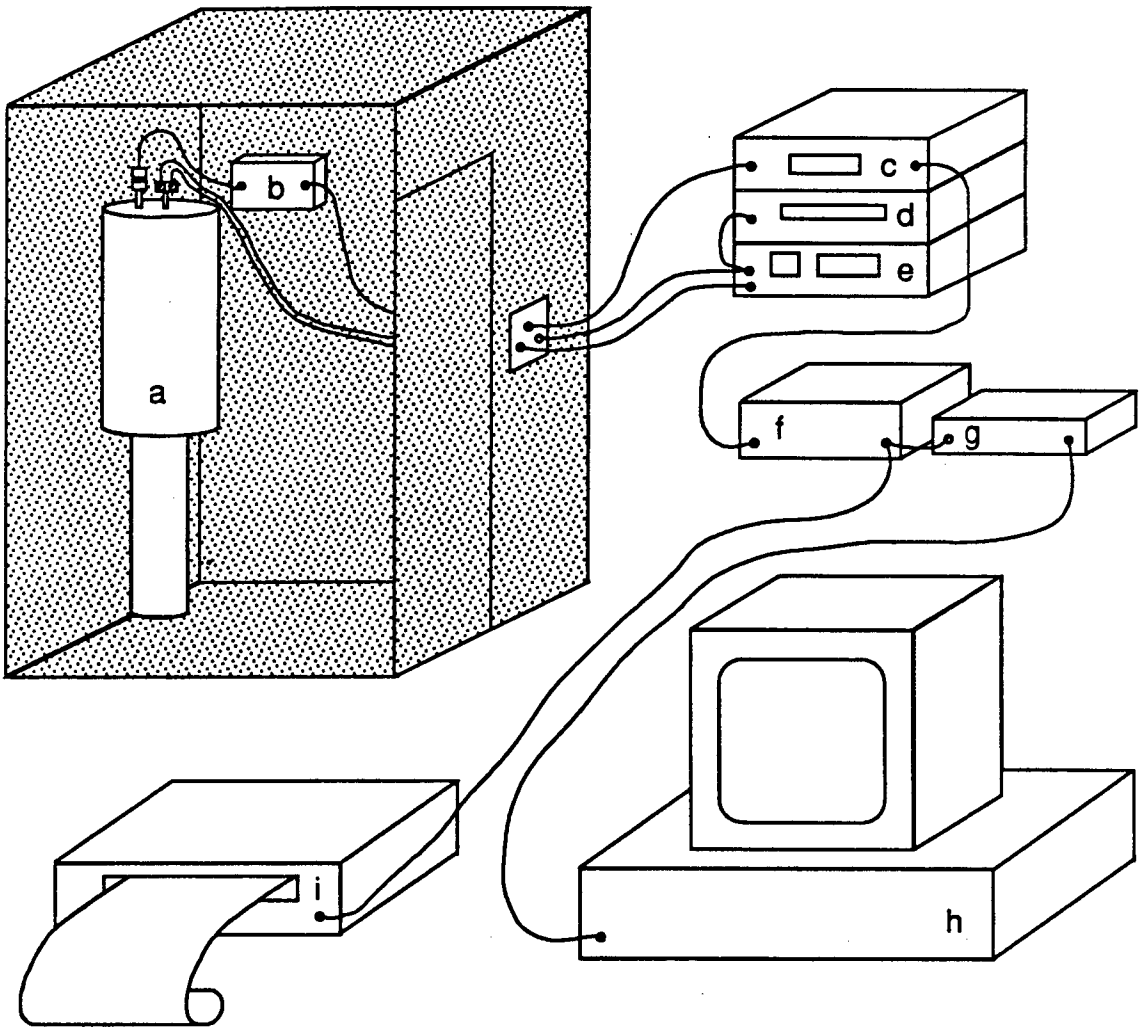

Figure IV.1: Schematic of the SQUID spectrometer. The components are as follows: a)liquid helium cryostat, b)SQUID feedback unit, c)SQUID control unit, d)frequency counter, e)two channel rf synthesizer, f)low pass filter, g)analog to digital converter, h)computer, i)chart recorder.

C. Low Temperature Probe

The low temperature probe was built to fit a liquid helium cryostat that was originally designed to fit into a superconducting magnet, so it had a long, narrow geometry. The upper part of the cryostat has an inside diameter of 3.25", which forced a rather compact design for the probe.

A cutaway view of the sample chamber and SQUID region of the current configuration of the probe is shown in Figure IV.2. During design, careful attention was paid to shielding all sensitive areas from electromagnetic interference, and to minimizing vibration of the parts of the probe with respect to each other. The SQUID housing, shown on the left hand side of Figure IV.2, is mounted on the end of a 31" long, 1/4" diameter stainless steel tube. Connected to the upper end of this tube is a 13 pin female connector for the cable to the feedback unit. The length of this tube restricts the distance from the SQUID to the top of the cryostat. The SQUID itself is hermetically sealed during manufacture, making it inaccessible to the user. A sliding niobium shield allows access to two 0-80 brass screws which connect to the coupling coil. The SQUID housing is securely fastened to the body of the probe by a lead nut on the 1/4-20 threaded niobium tube on the bottom of the housing.

The lower part of the probe, with the exception of the copper can covering the shunt resistor board, is made of brass. Solder coated 1/8" thick brass plate was used for the top and bottom of the sample chamber. The copper can and the sample chamber are lined with 0.005" lead foil.

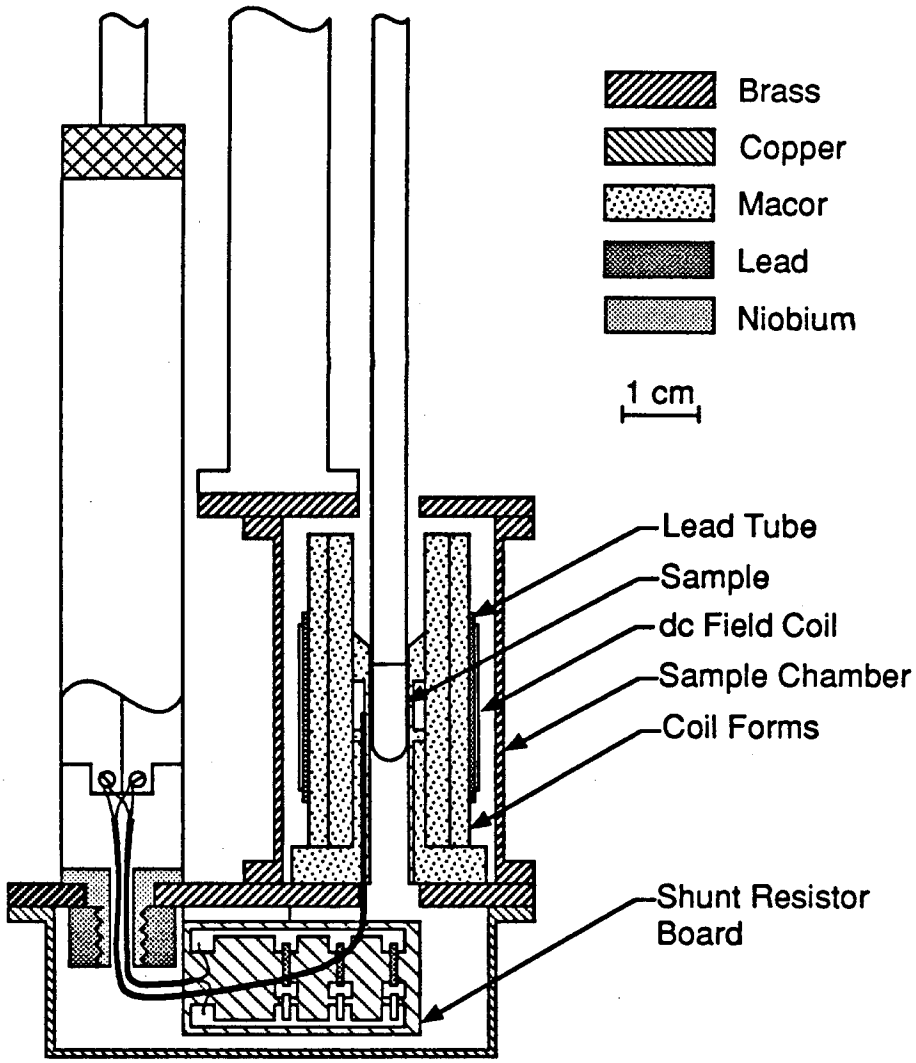

Figure IV.2: Scale drawing of the lower part of the low-temperature probe. See text for a complete description.

At liquid helium temperature solder and lead become superconducting, and are extremely effective in shielding magnetic interference at all frequencies.

The shunt resistor board was made by removing part of the copper cladding from fiberglass printed circuit board. The remainder of the cladding adheres very strongly, even at liquid helium temperatures. Three shunt resistors, made from 0.005" diameter manganin wire, are placed in parallel across the input to the SQUID. The resistances, typically about 1 to 0.01 Ω, were determined from the stated room temperature resistance of the wire, 11.67 Ω/ft. A change of about 10% in the resistance is expected on cooling to 4.2 K. Each of the resistors could be removed from the circuit separately by breaking a thin lead bridge in series with the resistor. Any bridge could be broken, while the probe was cold, by pulling on one of three strings (not shown) leading outside the cryostat. A twisted pair of 32 AWG copper wires, shielded by a 1 mm o.d. 60/40 lead-tin tube, connects the shunt resistor board to the SQUID input terminals. No mechanical problems were observed in several dozen runs using the shunt resistor board.

The pickup coil leads are also shielded by the lead-tin tubing. Forms for the pickup coil, rf coils, and field trapping tube were machined from MACOR, a mica glass-ceramic.[18] The pickup coil, 6.5 mm in diameter, is wound with 10 turns of 0.005" diameter Formvar-insulated NbTi wire. A slot about 0.012" wide and 0.065" deep was cut in the pickup coil form, and the pickup coil wound tightly inside. Cyanoacrylate glue keeps the coil rigid during operation.

The rf coils consist of two orthogonally oriented pairs of

Helmholtz saddle coils. For each coil, three turns of 32 AWG copper wire were wound inside 1/32" by 1/32" slots in the rf coil form, then potted in epoxy. The dimensions of the coils, 26 mm long by 16 mm in diameter and each forming an arc of 120^{o}, were arranged to maximize the rf field homogeneity. The calculated field to current ratio for each pair is 3 G/A. Experiments described in Chapter V indicate that the resulting fields are very nearly orthogonal.

A small dc field can be trapped in a lead tube around the outer coil form. The tube, made by rolling up and soldering closed a 1 mm thick lead sheet, fits tightly over the form at room temperature. The field is generated during cooling down of the probe by passing current through a copper solenoid wound tightly on the outside of the lead tube. This solenoid is made of 67 turns of 28 AWG wire, giving a calculated field of 30 G/A. The measured field trapped in the tube is very nearly equal to this calculated value.

The coils were centered with respect to each other to within about 0.005", and centered both laterally and longitudinally within the sample chamber to better than 0.040". The three MACOR coil forms were machined to tolerances of 0.003", so they fit very snugly together. To prevent vibration at low temperatures, but still allow easy dismantling, the mating surfaces of the forms were coated with a thin layer of vacuum grease before assembly. The entire coil form structure is screwed securely to the bottom of the sample chamber by two 6-32 nylon screws. To permit easy sample changing, it was necessary to compromise the shielding of the pickup coil somewhat by boring a 6 mm diameter hole through the top of the sample chamber.

Samples are packed in thin-walled 5 mm o.d., 4.5 mm i.d., glass NMR tubes, cut off to 7 cm long. Usually two or more samples, each about 1/2" long and separated by 1/4" spacers, are packed in each tube. The tubes are mounted by sliding them over the end of a sample stick, shown in Figure IV.3. Because the glass shrinks less than most organic solids on cooling, occasionally the sample tube remains in the probe when the sample stick is withdrawn. The problem was alleviated somewhat by cutting slots near the end of the sample tubes, and putting a thin coat of vacuum grease over the sample stick before mounting the tube. Even with this measure, the arrangement is not completely reliable.

D. Cryostat and Room Temperature Shielding

As previously mentioned, the cryostat used for this work was originally intended for high field NMR. It is constructed from stainless steel, and has a liquid nitrogen jacket. The helium capacity is about 10 liters. About 5 hours of operation are possible before the helium level reaches the SQUID. The helium level is monitored by a standard liquid helium probe and meter (American Magnetics Model 110) during the helium fill and periodically during operation.

A μ-metal shield on the outside of the cryostat reduces the ambient field by about a factor of 25 in the vicinity of the sample chamber. This shield is necessary during filling of the dewar to prevent trapping the small ambient magnetic field. After the superconducting shielding in the probe has cooled, the μ-metal shielding is probably not necessary.

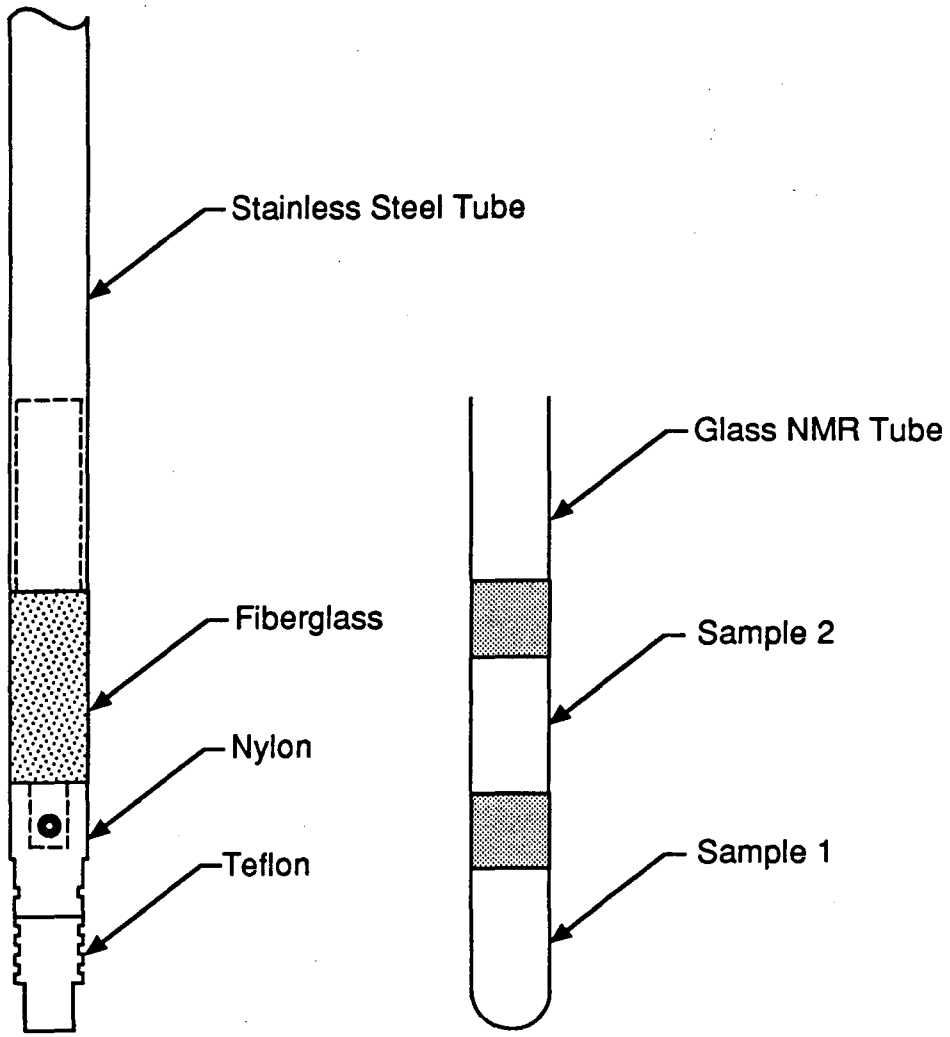

Figure IV.3: Detail of the sample holding arrangement. The glass sample tube slides over the end of the sample stick, shown on the left.

The SQUID is operated in a fairly noisy environment; there are several computers and a pulsed NMR spectrometer in the same room as the SQUID, and pulsed lasers are located in rooms nearby. To filter out some of this high frequency electromagnetic interference, a Faraday cage, constructed of copper mesh stapled on a wooden frame, surrounds the cryostat. The dimensions of the cage are approximately 6 feet square by 8 feet high. A copper plate with feed-through BNC's is used to pass wires into and out of the cage. Another connector in the plate passes the signals between the SQUID feedback unit and the SQUID controller. We do not operate any devices inside the cage which require 110 V ac power.

E. Room Temperature Electronics

During this work several rf sources were used. The earliest work was done with a homebuilt rf sweeper based on a voltage controlled oscillator (VCO). An op amp with a capacitor in its feedback path integrates a small dc voltage to produce a voltage ramp, which is fed into the VCO. Varying the dc voltage changes the sweep rate. The TTL output of the VCO is fed through a capacitor to remove the dc offset. This sweeper gives a maximum sweep range of about a factor of two, with the sweep center ranging from about 80 kHz to several megahertz. We used this device sucessfully for many experiments, but it has several drawbacks. The sweep is not highly linear, so careful frequency markers must be recorded for accurate frequency measurement. Many of the front panel controls are analog, so sweep conditions were hard to reproduce exactly. Finally, a separate current divider and phase shifter was

required to generate circularly polarized rf. Circularly polarized rf can be produced by feeding rf currents with the same amplitude, but a 90^{o} phase difference, into two orthogonally oriented coils. Before discussing the replacement for this sweeper, we briefly discuss the phase shifters used for our earlier work.

The simplest phase shifter is simply a pi network, as shown in Figure IV.4. We assume the phase shifter is inserted between components with input and output impedances of Z_o. If the condition $Z_o = 1/\omega C = \omega L$ is satisfied, a current will experience a 90^{o} phase shift as it passes through the network. This device has the advantage that it can withstand a great deal of current, if high power components are used, but unfortunately it is only suitable in the vicinity of $\omega = 1/Z_oC$.

A low power, broadband phase shifter was also constructed. This device, based on TTL logic, is represented in Figure IV.5. It produces exact 90^{o} phase shifts, assuming a 50% duty cycle of the input voltage, but it requires an input frequency of 2ω, twice the output frequency. The principle of operation is very simple: the input is split into two components, one of which is then inverted. The frequency of each component is divided in half by a D-type flip-flop. Since the flip-flops are positive-edge triggered, the output changes state only on positive edges of the input voltage. This triggering condition insures that the two outputs have a 90^{o} phase difference, rather than 0^{o} or 180^{o}. With this type of phase shifter, producing a $\pi/2^{n}$ radian shift at frequency ω requires an input frequency of $2^{n}\omega$, if the duty cycle of the input is fixed at 50%. Changing the duty cycle of the input produces two output components, each with a duty cycle of 50%, and an arbitrary phase

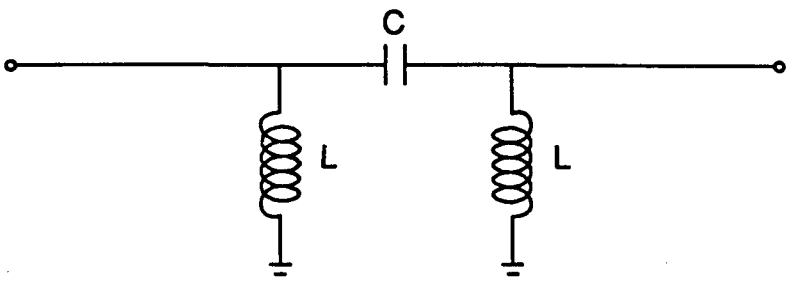

Figure IV.4: A simple narrowband 90° phase shifter, potentially useful for high power.

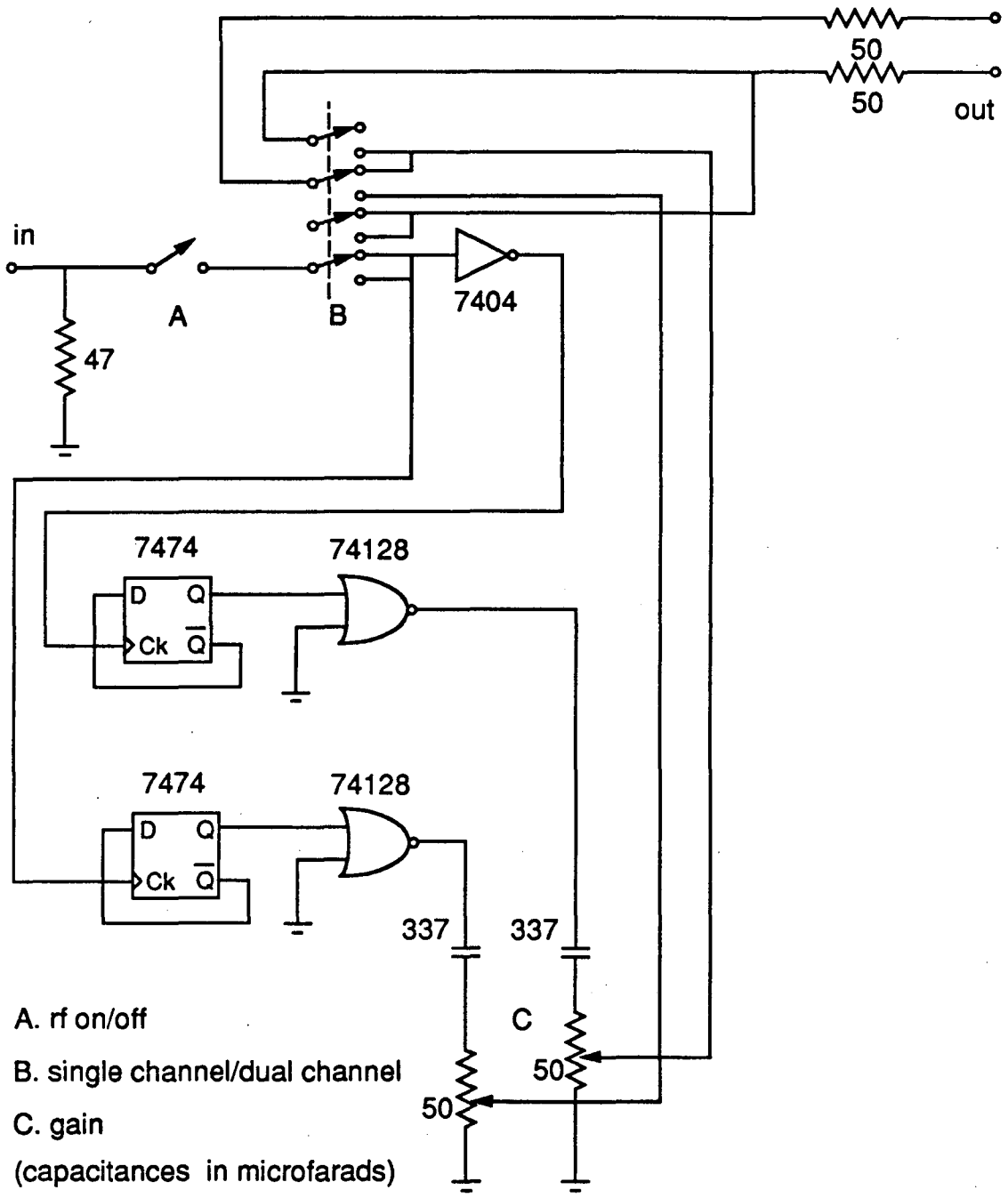

Figure IV.5: A low power, broadband phase shifter. An input at frequency 2ω produces two outputs at ω, with a 90° phase difference.

difference.

The rf generation problems were greatly simplified by the purchase of a Hewlett-Packard 3326A Two Channel Synthesizer that operates from dc to 13 MHz, at an output level of up to 10 V into 50 Ω. The sweep time can be varied from 1 ms to 1000 s. In two phase mode the two channels sweep together with a set phase difference, adjustable from 0 to 720°. Since the frequency synthesis is done digitally, it is possible to easily and repeatably set all parameters to any specified value. In addition, it is controllable by computer over the HPIB interface. The one disadvantage of this instrument is its restricted frequency range.

Higher frequency sweeps have been generated by discretely incrementing the frequency of a PTS 500 (Programmed Test Sources) synthesizer by computer control. Although strictly speaking this is not a frequency sweep, and may not work for experiments requiring adiabatic rapid passage, it worked very well for our purposes. Some commercial high frequency sweepers (e.g. Wiltron 610C and Wavetek Model 1062) do not have the precise frequency control required for observing narrow lines at high frequencies.

We next consider the processing of the signal as it comes from the SQUID probe (BTi Model DP probe with Model DSQ DC Hybrid SQUID).[19] The feedback unit (BTi Model 400) functions essentially as described in Chapter III. The signal is passed from the feedback unit to the SQUID controller (BTi Model 40), where it is amplified (x1, x10, x100, or x1000) and filtered. Either a 5 kHz or a 50 kHz bandwidth may be selected. Since the 5 kHz bandwidth is still far larger than we normally require, the output voltage of the SQUID is passed through a homebuilt

low-pass filter. The circuit diagram for this device is shown in Figure IV.6. It has a floating input as recommended by BTi, with an input impedance of 20 kΩ. Since the input floats, wild swings in the output voltage will be seen if the input is disconnected. Making a connection from the shield of the input BNC to ground will stabilize this effect if required. The bandwidth can be set from 200 Hz to 0.02 Hz in factors of ten, and the gain is continuously variable from 10 to 120.

The integrated signal is fed directly to a chart recorder (Fisher Series 5000). The mechanical damping of the pen mechanism limits the frequency response of the recorder to about 4 Hz.

If run averaging or further signal processing is required, data are collected on an AT clone computer (Leading Edge Model MH). The signal is digitized by an 8-bit digitizer (Rapid Systems Model R1000), then stored in RAM on the Rapid Systems interface card (Model R320).[20] After all the requested data points are collected, the data may be processed by the TMS 32010 processor on the interface board, or passed directly to computer RAM. Code was supplied by Rapid Systems to enable the TMS processor to do Fourier transforms. This option is sometimes used for diagnostics on the SQUID system, but data collected during frequency sweeps is sent directly to RAM after the sweep is completed. Data acquisition and frequency sweeps are controlled by a heavily modified program from Rapid Systems, written in Turbo Pascal.

Further data processing is done with another Turbo Pascal program. This program currently allows the user to make screen plots of the data, correct for linear baseline drift, smooth the data, fit to an exponential, add and subtract spectra, etc. Combining this program with

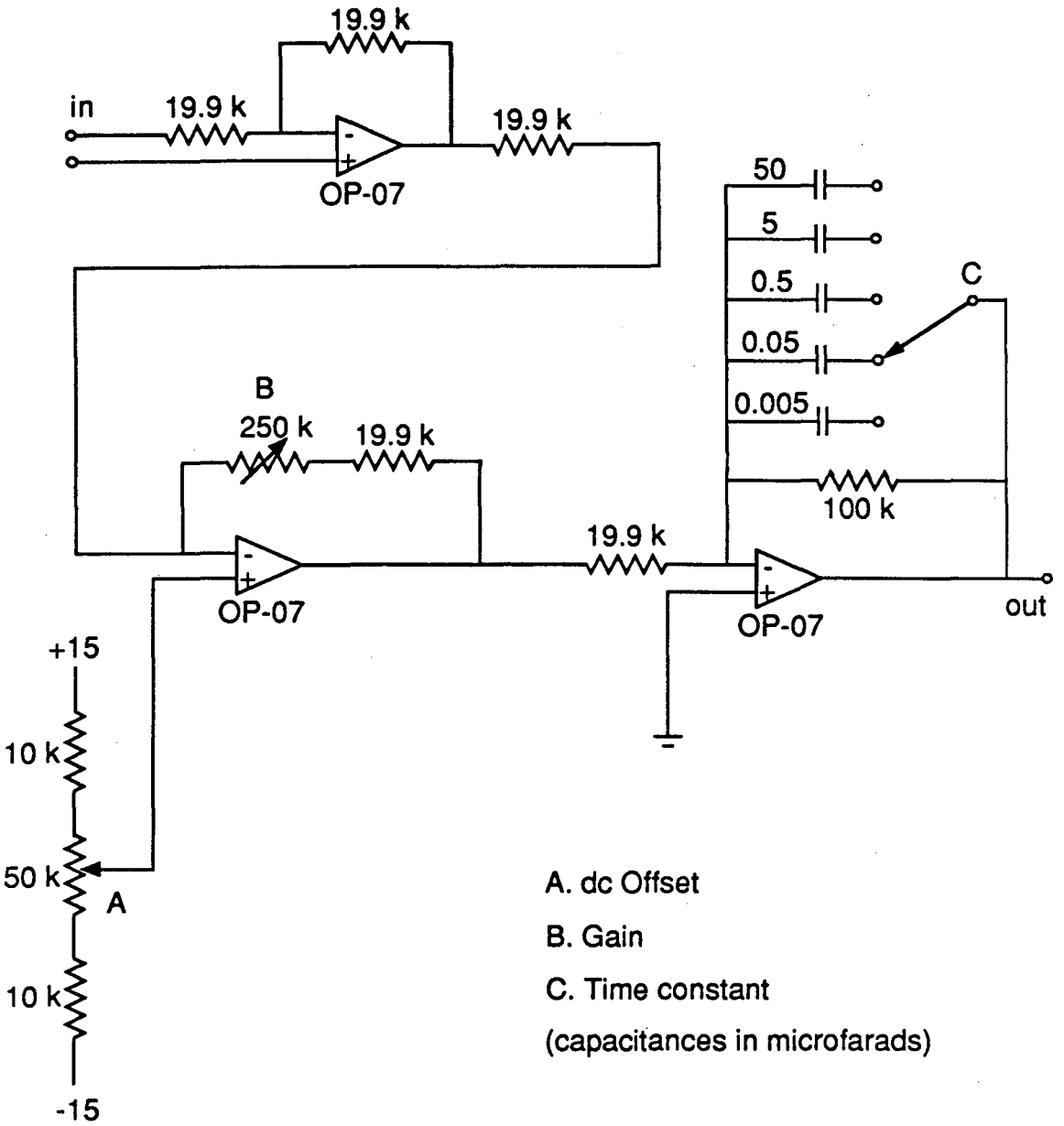

Figure IV.6: Low pass filter used for the SQUID output voltage.

the data acquisition program would simplify spectrometer operation.

F. System Performance

One parameter of interest for pulsed NMR spectrometers is the recovery time of the system after a magnetic field pulse has been applied to the sample. For work with solid samples this recovery time should be on the order of 10 μs or less, but some experiments will still be possible if the recovery time is longer. Although we are currently using cw mode, earlier experiments with our system were attempted in pulse mode. Since the recovery time of the BTi SQUID system may be of some interest for future experiments, two measurements of recovery time are reported in Figure IV.7. The coil configuration for these tests was a Helmholtz pair pulsing coil centered around a gradiometer-type pickup coil. Although the coils are collinear, the pulsed field is attenuated to better than 1 part in 100 by the gradiometer arrangement. The dc field pulse was applied by a Cober Model 606P pulse generator through a 200 Ω resistor in series with the pulsing coil. The field to voltage ratio for this arrangement is about 0.05 G/V. The blanking line to the SQUID, which probably decouples the SQUID from the preamplifier, is kept low (blanking on), during the pulse. The recovery time constants are on the order of 50 μs for the 50 V pulse and 100 μs for the 2000 V pulse. These recovery times are acceptable for pulsed NMR experiments in solids under favourable conditions.

With the spectrometer configured to run in the cw mode, as described in this chapter, one of the more important parameters is the

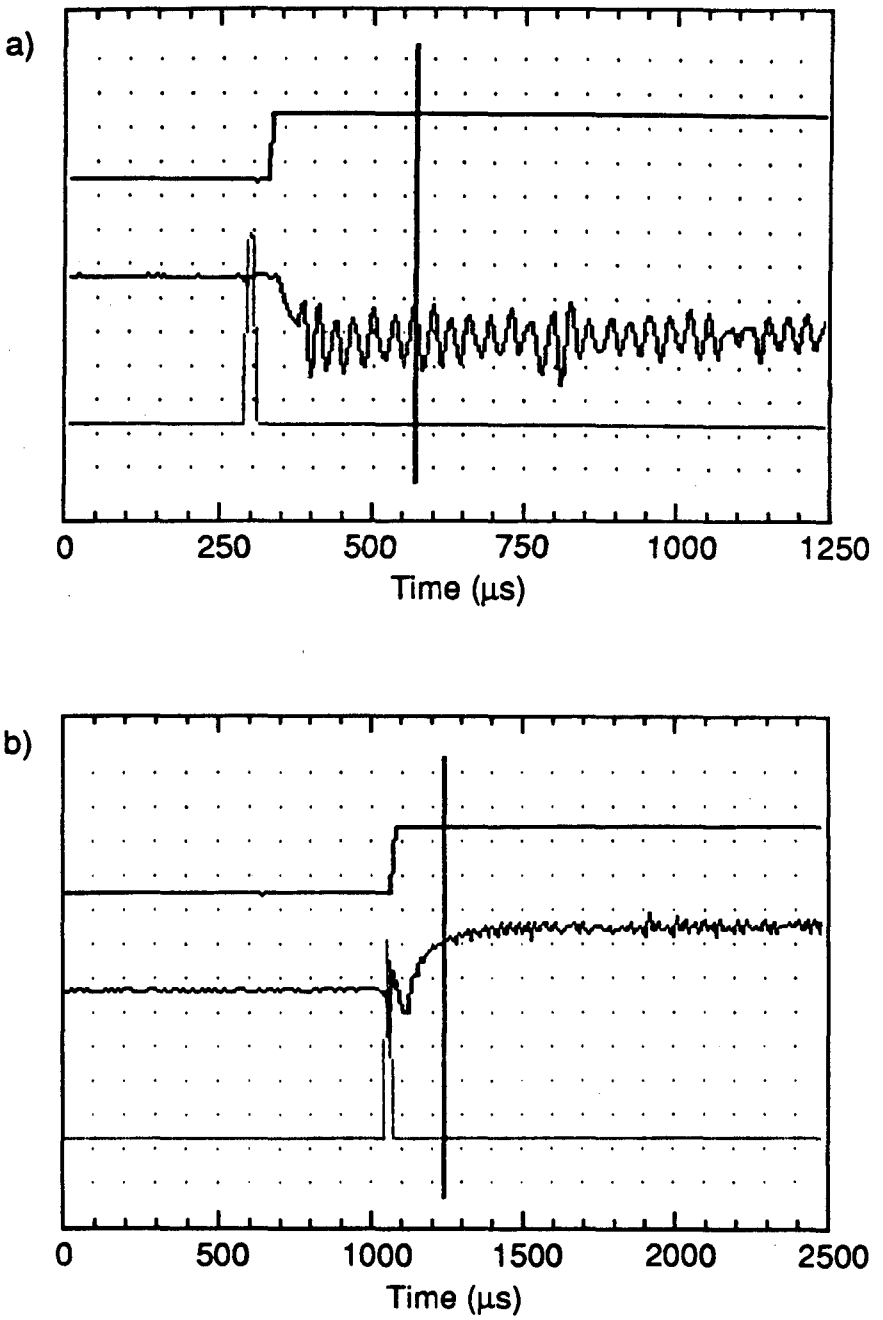

Figure IV.7: Recovery time measurements for the SQUID spectrometer, following a magnetic field pulse to the sample region. The voltage of the pulse is a)50 V and b)2000 V. The top trace in each figure shows the blanking line to the SQUID, which is disabled after the pulse. The middle trace shows the SQUID output, and the bottom trace the pulse.

coupling between the rf coil and the pickup coil. We have made fairly extensive measurements of this coupling for various shunt resistances. Figure IV.8 summarizes the results from these studies. These measurements were made by applying a fixed voltage to the rf coils and measuring the attenuation required to maintain the flux-voltage curve at a predetermined amplitude. We assume that all the rf frequencies, for a given amplitude, are equally effective in averaging the flux-voltage curve. These curves show that the shunt resistance is working as a low pass filter as expected. Using the inductance of the pickup coil, $L_p = 1.3\ \mu H$, and Equation (IV-3), the calculated 3 dB point of the filter is 200 kHz/Ω.

In both pulsed and cw mode the frequency spectrum of the noise should be well characterized. The easiest way to measure the frequency spectrum of the noise is by Fourier analysis, and the results from this method are shown in Figure IV.9. We see that the noise is white down to a frequency on the order of 1 Hz, and increases sharply below this frequency. Normally we observe magnetization changing at a rate on the order of 0.1 Hz, assuming a linewidth of 10 kHz and a sweep rate of 1 kHz/s. Thus lock-in detection combined with signal modulation may provide a large increase in sensitivity.

The magnitude of the noise is strongly dependent on the operating conditions. Often the noise level decreases during the first hour after the cryostat is filled with helium. This may be due to flux shifting within the SQUID probe or to temperature variations in the cryostat. The noise increases with the applied dc magnetic field. Since we are not currently using a gradiometer coil, the dc field is tightly coupled into

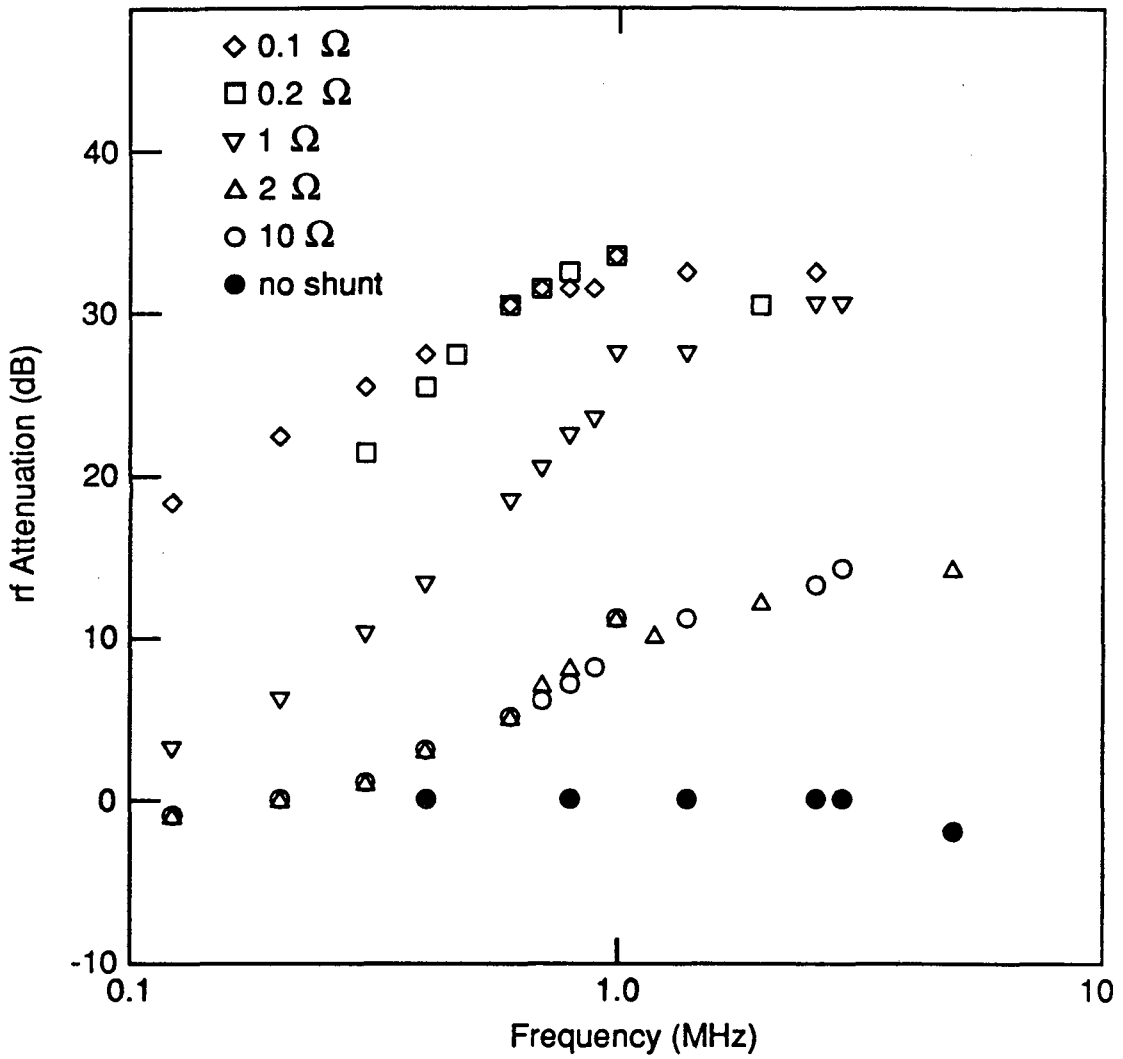

Figure IV.8: Measurements of the rf coupling to the SQUID for various shunt resistances. The y-axis represents the attenuation of rf by the shunt resistor, with the zero corresponding to $R_s = \infty$.

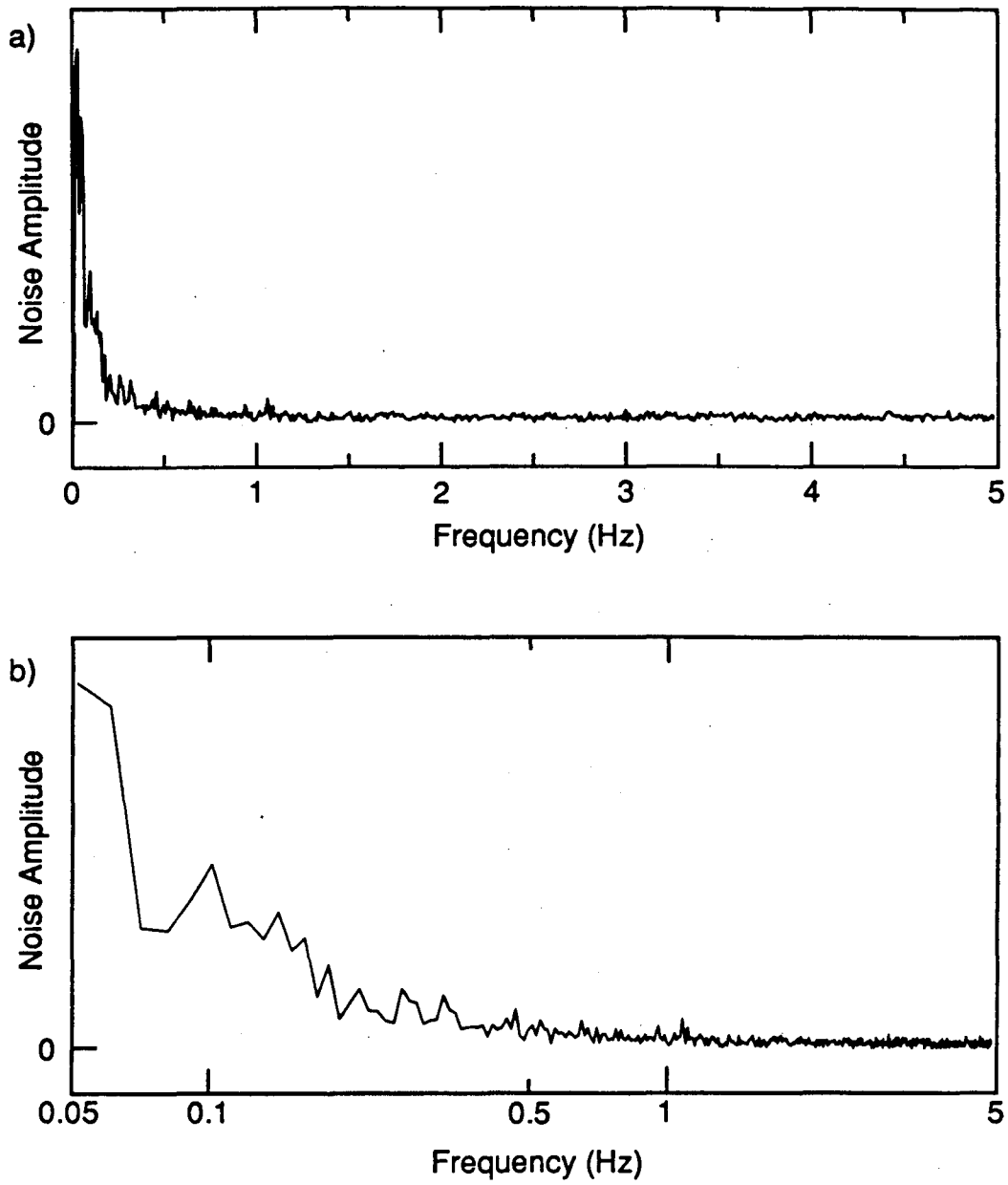

Figure IV.9: a)Noise amplitude per root hertz, as a function of frequency, at the SQUID output. b)Noise amplitude versus logarithm of frequency, showing the inverse frequency dependence.

the SQUID. Normally the noise increases by about an order of magnitude on going from a field of 10 G to 100 G. This noise increase could be due to increased flux movement in superconductors near the pickup coil, to paramagnetic materials in the probe, to small vibrations in the pickup coil, etc.

The noise level also increases with the amplitude of the rf field. This is due to partial averaging of the flux voltage curve as described earlier. Reducing the rf frequency at fixed amplitude also increases the noise, since the shunt resistor in the pickup circuit does not filter as effectively at low frequencies.

The actual noise observed in the output of the SQUID under normal operating conditions (with a dc field 10 G, rf field about 10 mG, filter bandwidth of 2 Hz, and total gain of 10^4) is on the order of 50 $mV/\sqrt{Hz}$ in the white region. Using the flux to voltage gain for the SQUID under these conditions, 51 V/Φ_o through the SQUID, and the stated intrinsic noise in the SQUID system, 1.2×10^{-5} $\Phi_o/\sqrt{Hz}$, we calculate an expected noise of 0.61 $mV/\sqrt{Hz}$. The discrepancy between these noise levels is of concern, but modifications to the spectrometer have not resulted in significant improvements.

It is often useful to know the absolute magnitude of the measured magnetization of the sample. The easiest way to calibrate the SQUID for this type of measurement is to wind a solenoid of the same dimensions as the sample. When the solenoid is placed in the position the sample normally occupies, a magnetization is produced by passing a current through this coil. Then one easily finds the overall gain of the spectrometer, in terms of the change in the output voltage for a given

sample magnetization. For our system, with the total gain set to 10000 (1000 from the SQUID controller and 10 from the integrator), we obtain 23 V/μG. Using this calibration factor, we estimated the absolute magnetization for several samples. The comparison with the calculated magnetization for these samples, shown in Table IV.1, indicates a reasonable agreement.

Table IV.1: Comparison of Measured and Calculated Sample Magnetization

Sample	Measured (μG)	Calculated (μG)
α-Alumina crystal (^{27}Al)	0.19	0.23
Nylon (^{1}H)	2	2.1
Teflon (^{19}F)	1.5	1.6
Propionic Acid (^{1}H)	1	1.7
Copper Acetate (^{1}H)	0.38	1.5
Boron Nitride (^{11}B)	0.1	0.8

These calculations were based on the assumption that all the nuclei in the sample contribute to the signal. Magnetizations were calculated using Table II.1 for NQR experiments (^{27}Al and ^{11}B), and using Equation (II-7) for NMR (^{1}H and ^{19}F), assuming the rf field completely saturates the spins. The reduced intensity of the boron nitride powder is at least partially due to the effects described in Section IID.

REFERENCES

1. E. P. Day, Phys. Rev. Lett. 29, 540 (1972).

2. M. Kohl, M. Odehnal, V. Petříček, and R. Tichý in SQUID'85-Superconducting Quantum Interference Devices and their Application, edited by H. D. Hahlbohm and H. Lübbig, (Walter de Gruyter, Berlin, 1985).

3. B. S. Deaver, Jr., T. J. Bucelot, and J. J. Finley in Future Trends in Superconductive Electronics, edited by B. S. Deaver, Jr., C. M. Falco, J. H. Harris, and S. A. Wolf (American Institute of Physics, New York, 1978).

4. S. E. Nave and P. G. Huray, Rev. Sci. Instrum. 51, 591 (1980).

5. J. S. Philo and W. M. Fairbank, Rev. Sci. Instrum. 48, 1529 (1977).

6. M. Cerdono, F. Mogno, G. L. Romani, C. Messana, and C. Gramaccioni, Rev. Sci. Instrum. 48, 300 (1977).

7. L. J. Friedman, A. K. M. Wennberg, S. N. Ytterboe, and H. M. Bozler, Rev. Sci. Instrum. 57, 410 (1986).

8. R. V. Chamberlain, L. A. Moberly, and O. G. Symko, J. Low Temp. Phys. 35, 337 (1979).

9. T. Jach, Ph.D. Thesis, Stanford (1975).

10. R. A. Webb, Rev. Sci. Instrum. 48, 1585 (1977).

11. J. Knuutila, A. Ahonen, and C. Tesche, J. Low Temp. Phys. 68, 269 (1987).

12. K. Weyand, Rev. Sci. Instrum. 59, 971 (1988).

13. R. L. Fagaly, Sci. Prog., Oxf. 71, 181 (1987).

14. J. Clarke, W. M. Goubau, and M. B. Ketchen, J. Low Temp. Phys. 25, 99 (1976).

15. J. H. Claassen, J. Appl. Phys. 46, 2268 (1975).

16. D. P. Osterman and S. J. Williamson, Rev. Sci. Instrum. 54, 1380 (1983).

17. E. P. Day. Ph.D. Thesis, Stanford (1972).

18. Corning Glass Works, Corning, NY 14830.

19. Biomagnetic Technologies, Inc., 4174 Sorrento Valley Blvd., San Diego, CA 92121.

20. Rapid Systems, Inc., 755 N. Northlake Way, Seattle, WA 98103.

V. NQR RESULTS

A. α-Alumina

This section presents results on α-Al_2O_3 single crystal and powder samples. These samples were quite thoroughly studied in an attempt to confirm much of the theory outlined in Chapter II. The availability of high quality single crystals, the simple crystal structure, convenient T_1, and good signal-to-noise ratio make this a very good compound for this type of work. Jach's original application of this NQR technique was on an α-Al_2O_3 crystal.[1]

Alumina commonly exists in three forms, referred to as the α, β, and γ forms.[2] γ-Alumina forms in a face centered cubic arrangement of 32 oxide ions. There are 16 octahedral and 8 hexagonal possible aluminum sites in this unit. As there are, on average, 21 1/3 aluminum ions in this unit, the aluminum is randomly distributed throughout the lattice. This randomness produces a broad distribution of quadrupole couplings, making any magnetic resonance experiment difficult. Attempts to obtain a signal from γ-alumina powder were unsuccessful, possibly due to this random distribution. The so-called β-alumina is not pure Al_2O_3, but contains other monovalent cations, often Na^+. Since it is also a disordered structure like γ-alumina, we did not attempt any experiments on the β form. α-Alumina is the densest and most highly ordered of the three forms. The oxygen ions are arranged in a hexagonal closest packed array. Two thirds of the possible aluminum sites, which are all octahedral, are filled in a well defined scheme. The local environment

of each aluminum ion consists of a triangle of oxide ions in the xy-plane of the quadrupole principal axis system, with symmetrically disposed oxide ions along the +z and -z axes. The z-axis of the principal axis system coincides with the crystallographic c-axis. This arrangement of oxygen nuclei produces an axially symmetric electric field gradient at the aluminum nuclear site. The field gradient splits the ±5/2 and ±3/2 states by 717 kHz, and the ±3/2 and ±1/2 states by 358 kHz. The splitting appears to be temperature independent between liquid helium temperature and room temperature.[1,3,4]

The single crystal used in this work was a cylinder 0.125" in diameter and 0.25" long, purchased from Union Carbide. The z-axis of the electric field gradient is aligned with the cylindrical axis of the crystal. The crystal was colorless and had a stated maximum paramagnetic impurity content of about 2 ppm.

The spectrum obtained from this crystal is presented in Figure V.1. The two transitions appear at the same frequency, to within experimental error, as those measured by Pound.[3] The plateau shape of the lines (see Figure II.4) is not readily apparent because of the large sweep width, as compared to the Larmor frequency. The calculated signal magnitude is 0.23 μG, while the measured magnetization is 0.19 μG. The measured magnetization was calibrated with a coil slightly larger than the sample, so the actual sample magnetization is very likely somewhat larger than 0.19 μG. The 0.23 μG is obtained by assuming the rf field saturates the transition, whereas if the adiabatic rapid passage condition is even partially satisfied, the calculated signal will be larger than 0.23 μG.

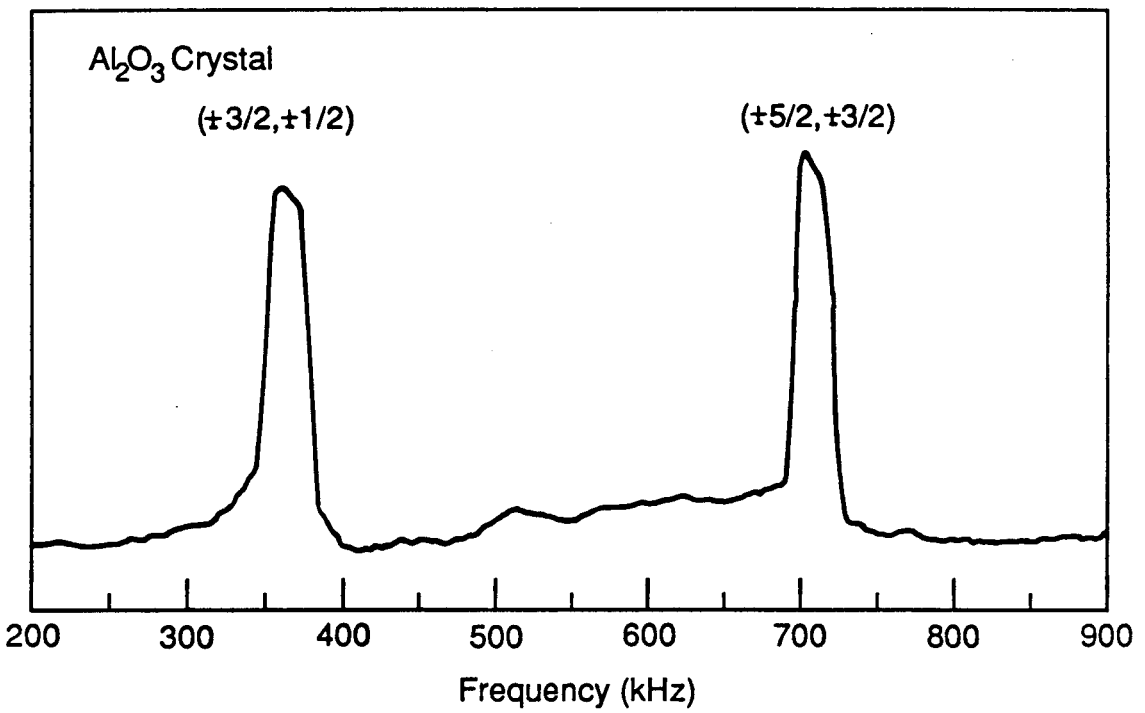

Figure V.1: The z-axis NQR spectra of a single crystal of α-Al_2O_3, in a dc field of 10 G.

Detailed studies of the lineshape of the (±5/2,±3/2) transition were made for a series of different sweep rates. As seen in Figure V.2 at the fastest sweep rate, the plateau lineshape as sketched in Figure II.4. is approximately obtained. This figure should be compared with the simulations in Figure II.6. The agreement with the simple model used for those simulations, within the narrow range of sweep rates studied, is quite good.

We also studied the polarization dependence of the two components of the (±5/2,±3/2) transition. They exhibited a similar behavior to the two components of the ^{35}Cl transition, observed by Weber and Hahn with pulsed NQR.[5] Our results are shown in Figure V.3. The assignment of the two components is based on a positive value for e^2qQ,[6] and the sign conventions used by Abragam.[7] The direction of the circular polarization is labelled according to the direction of rotation of the rf magnetic field, assuming the rf field corresponds to photons propagating toward the +z-axis. No attempt was made to correlate this labeling with the physical parameters of the rf field. The difference between the maximum of the upper trace and the minimum of the lower trace is roughly twice the Larmor frequency. In the limit of a very slow sweep, the Larmor frequency is exactly half the difference between the respective extrema of the curves. For an infinitely fast sweep, it is exactly half the difference between the points of maximum slope of the two curves. The signal decays in each case with a time constant T_1. Fitting a group of similar spectra to an exponential decay gives $T_1 = 70 \pm 20$ s. The large error in this value may be due to non-exponential relaxation, as has been observed for α-Al_2O_3 in high field at low temperatures.[8] This

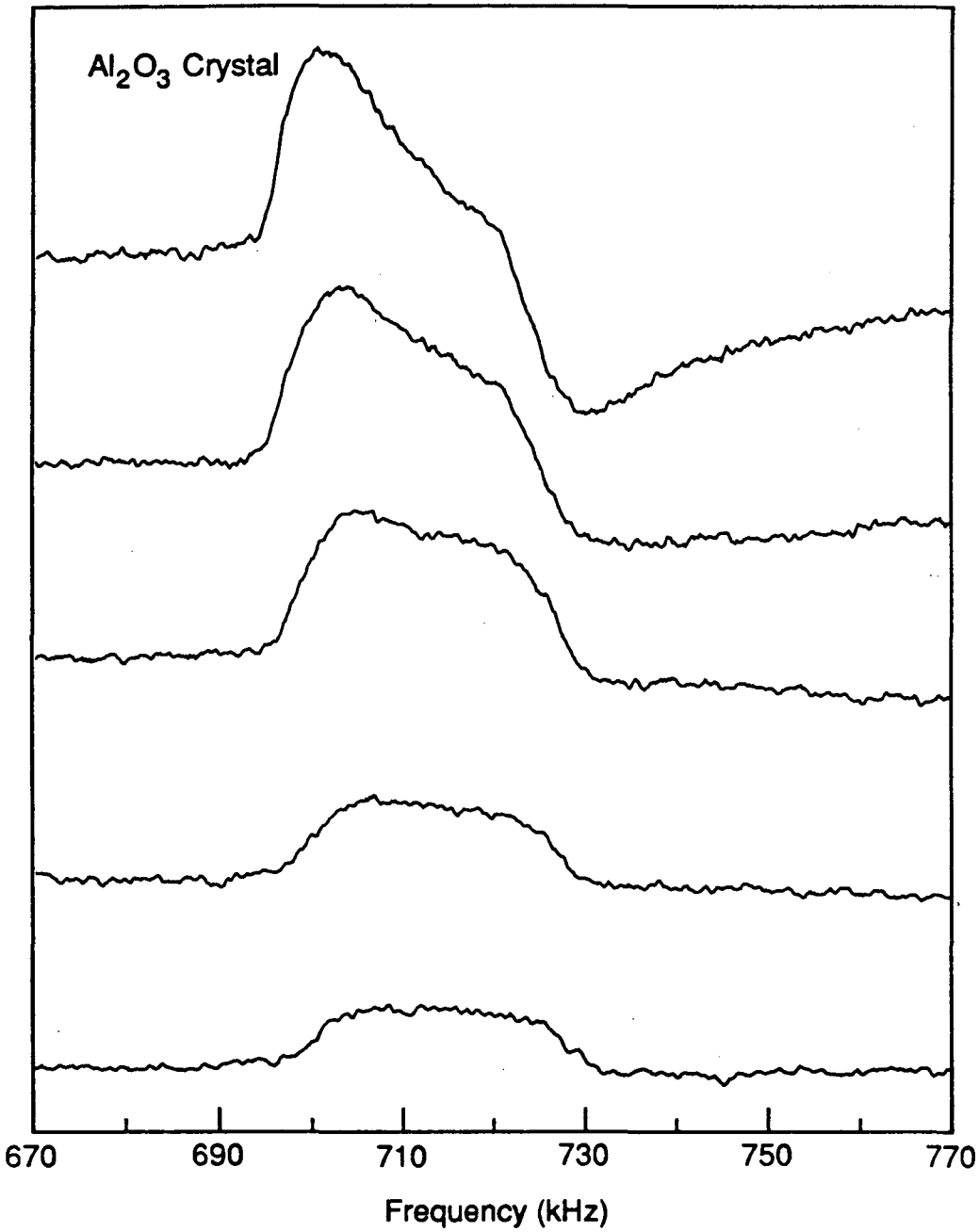

Figure V.2: Study of the lineshape of the (±5/2,±3/2) transition in an α-Al_2O_3 crystal, as a function of the sweep rate. The sweep rates, from top to bottom, are 0.2, 0.4. 1.0, 2.0, and 5.0 kHz/s.

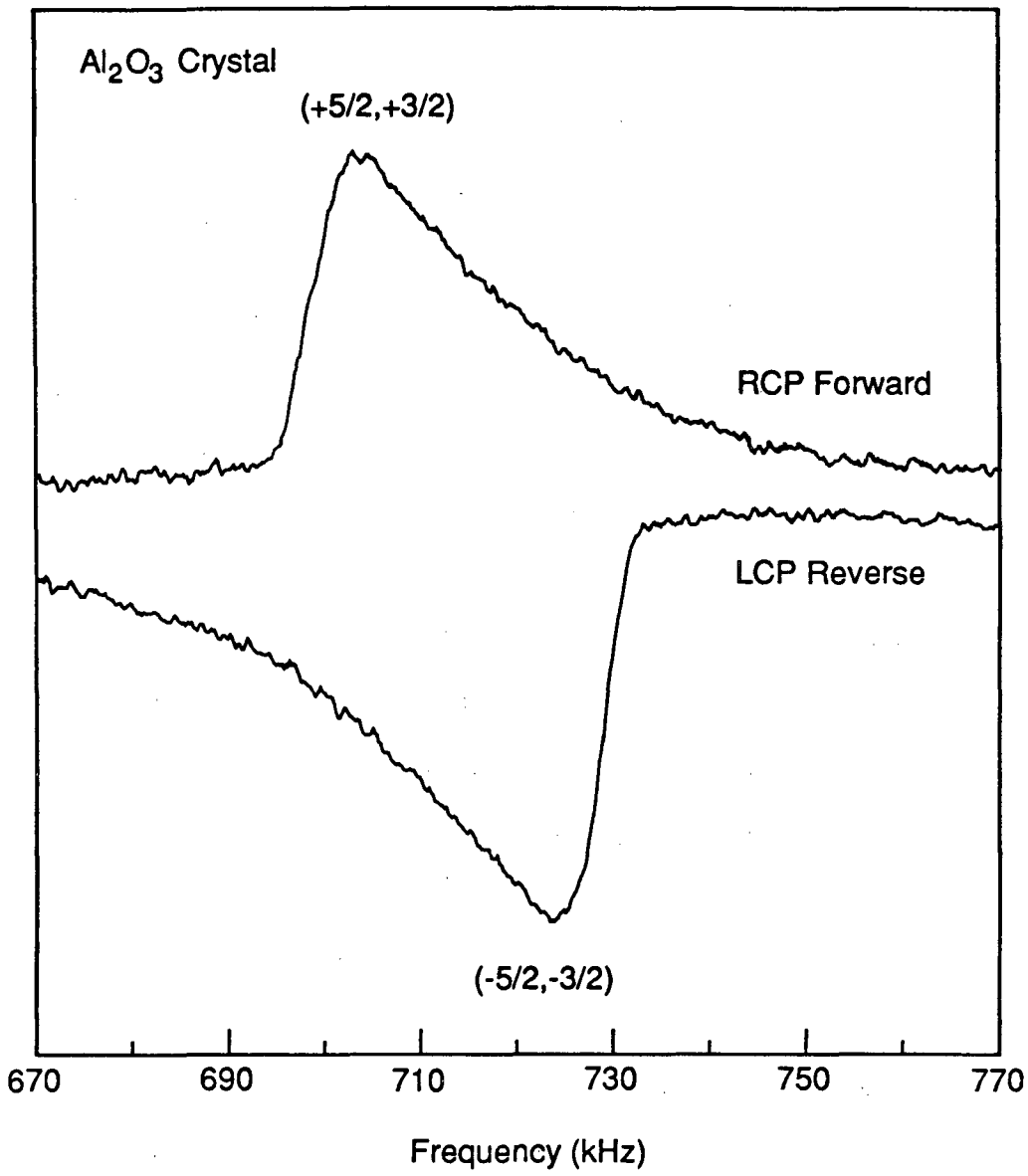

Figure V.3: Response of the (±5/2,+3/2) transition to circularly polarized rf fields. The upper trace was recorded during a sweep from low to high frequency, and shows the (+5/2,+3/2) component of the transition. The lower trace, using oppositely polarized circular rf swept from high to low frequency, shows the other component of the transition.

relatively short T_1, for nuclei in a rigid lattice, is due to fluctuating magnetic dipole moments of paramagnetic impurities in the sample.[9] Previous measurements of T_1 for α-Al_2O_3, as a function of paramagnetic impurity content, indicate this value of T_1 is not inconsistent with the maximum stated impurity level.[8]

One may wonder whether the absorption lineshape for the two transitions can be obtained from this type of spectroscopy. For a single crystal sample the answer is yes. As discussed in Section IIC, this may be done either by using a very slow sweep rate, or by taking the derivative of spectra recorded with a fast sweep rate. We have used the latter method, and show our results in Figure V.4. This derivative spectrum is obtained from the sum of the two spectra in Figure V.3. The widths of the two lines are on the order of 5 kHz. This width has been explained by dipolar coupling between ^{27}Al nuclei,[6,8] rather than by disorder in the crystal.

In choosing the sweep parameters for samples that have not been previously examined, it is important to know the general shape of the curves of signal strength versus rf strength and versus sweep rate. These two curves have been measured for α-Al_2O_3 (Figure V.5) and are considered representative of those for other samples. The variation with rf strength is fairly straightforward, having the general shape $(1 - \exp(-H_1/H_1^o))$. The parameter H_1^o describes the value of H_1 near the corner of the curve, and depends on the gyromagnetic ratio of the nuclei and on their spin-lattice relaxation time. When combined with the fact that the noise increases roughly linearly with rf strength, we see that there will be some optimum value of rf strength that gives the best

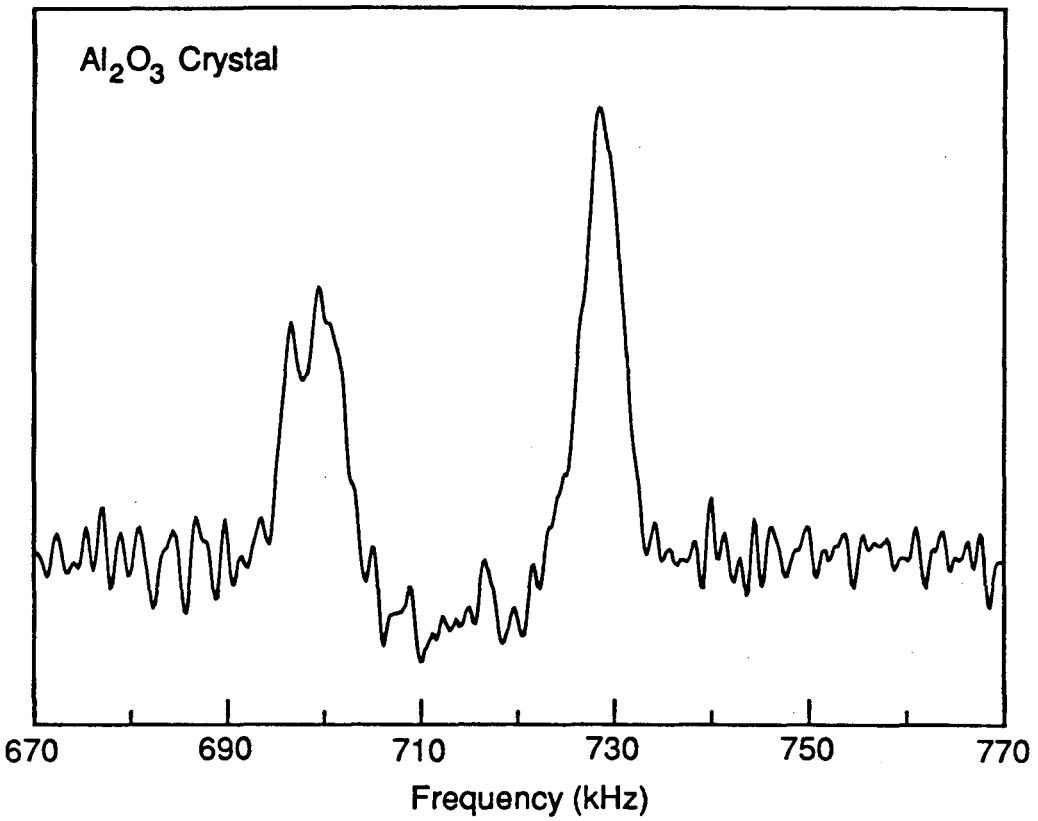

Figure V.4: Absorption lineshapes of the two components of the (±5/2,±3/2) transition in an α-Al_2O_3 crystal. This spectrum is obtained by numerically approximating the derivative of the sum of the two spectra in Figure V.3.

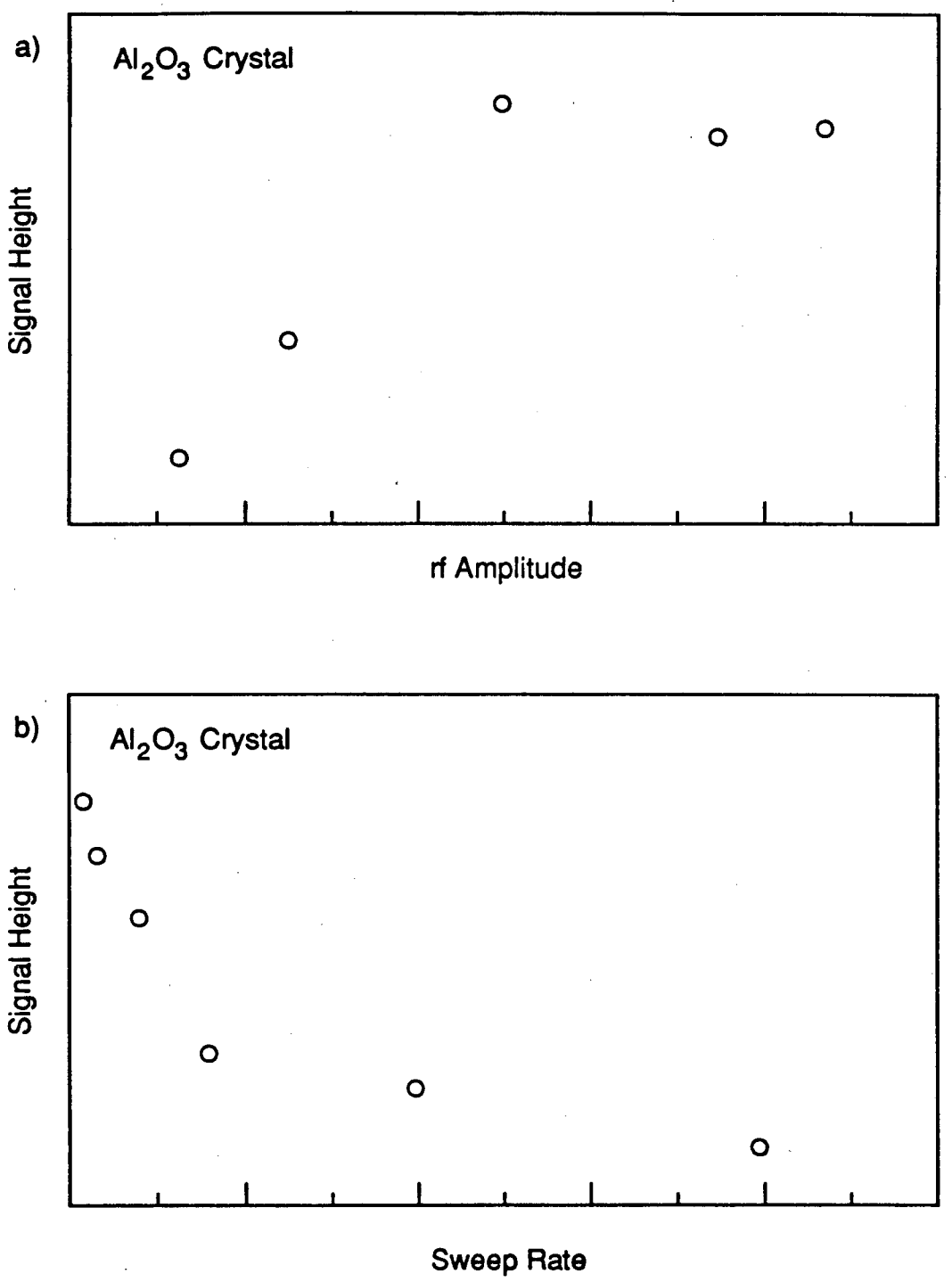

Figure V.5: Variation of the signal intensity as a function of a) rf amplitude, and b) sweep rate. These data were obtained from the (±5/2,±3/2) transition of an α-Al_2O_3 crystal, using linearly polarized rf.

signal to noise ratio. Unfortunately, this optimum value is usually difficult or impossible to estimate without knowledge about the samples behavior under these experimental conditions, since the variation of T_1 with magnetic field strength and with temperature is not easily predictable.

For the second plot, which shows the signal strength as a function of sweep rate, a qualitative explanation is easily made. At very fast sweep rates the rf frequency does not spend much time in the vicinity of the resonance frequency, so fewer nuclei undergo transitions for a given rf strength. As the sweep rate is reduced, more transitions are induced by the rf field, until at some rate the line is completely saturated. Under these conditions the maximum signal is obtained. If the line is inhomogeneously broadened, at sweep rates much slower than those used in Figure V.5(b) the signal should again begin to decrease. This occurs because spin lattice relaxation is able to restore equilibrium to the spin system nearly as fast as the rf field perturbs it. These competing effects reduce the signal for sweeps where the time required to pass through the line is on the order of T_1 or longer. Thus no signal will be observed for some samples with very short T_1's, because the maximum rf level is limited. The shortest T_1's that we are able to study depends on the linewidth, the cross-relaxation rate, the gyromagnetic ratio of the observed nuclei, etc.

Our last results on the α-Al_2O_3 system are for a powder sample. Initial experiments were carried out on a 3 μm powder sample from Linde, but only a very weak signal was observed. Two samples, of approximately 10 mesh and 50 mesh, were prepared by grinding a small piece of α-Al_2O_3

crystal similar to the one used for the crystal studies. Both these samples gave strong signals. The (±5/2,±3/2) transition for the more finely ground powder is shown in Figure V.6. A comparison with the magnitude of the signal from the crystal is of some interest, since it is a measure of the combined effects of the functions in Equation (II-20). A rough comparison shows that the signal from the powder sample is about 15% as large as that from the crystal. This spectrum was the first experimental indication that this method would be useful for powder samples. A glance at Equation (II-20) shows that it is by no means obvious that this technique would produce a signal of measurable intensity from powder samples. This is an important point, because single crystals are easily studied by conventional NMR techniques, whereas powder samples are much more difficult to study.

B. Boron Nitride

Boron nitride (BN), which is isoelectronic with carbon, has two phases analogous to graphite and diamond.[2] The cubic phase, in which boron and nitrogen nuclei are tetrahedrally bonded, has properties similar to diamond. We have studied the hexagonal phase, which is similar in structure to graphite. The boron and nitrogen nuclei are trigonally bound in infinite planes of six-membered rings, with little binding between planes. Unlike graphite, the nuclei in one plane are directly above the nuclei in the plane below, rather than offset by half the ring diameter.

We are concerned with the boron nuclei, of which there are two

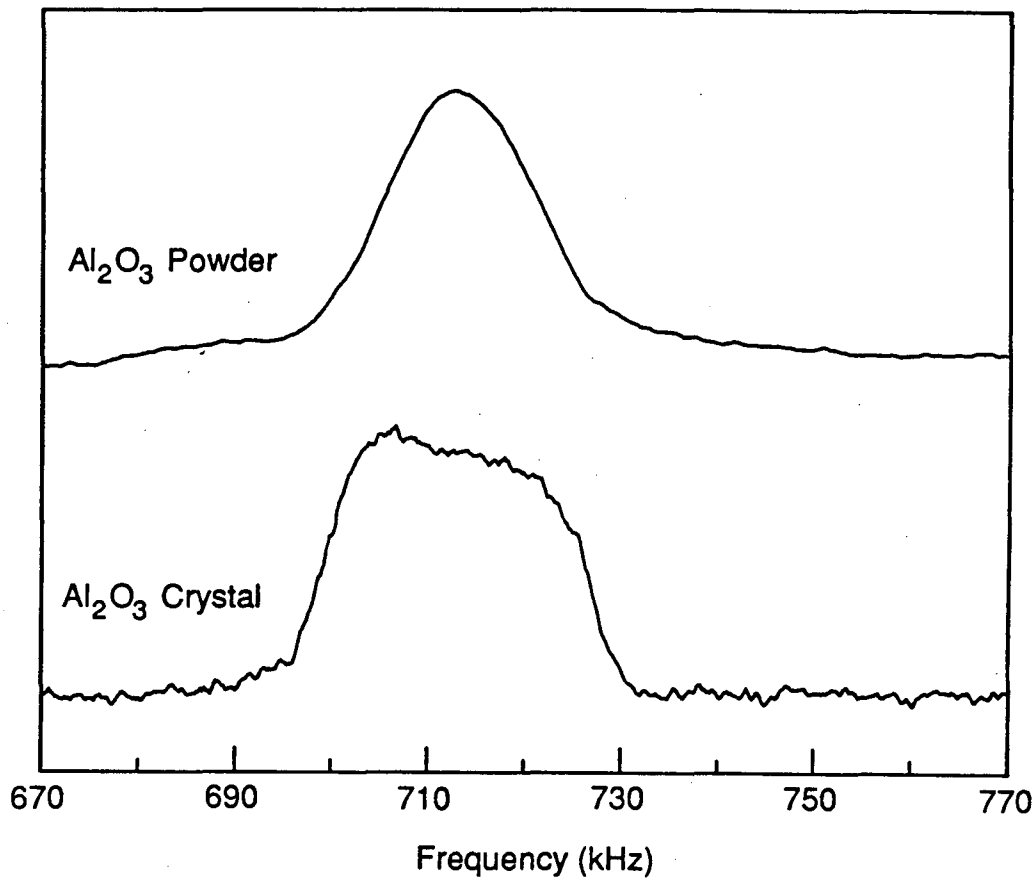

Figure V.6: The upper trace is the average of eight 8 scans of the (±5/2,±3/2) transition in α-Al_2O_3 powder. The single crystal spectrum, obtained under similar conditions, is shown below for comparison. This spectrum is the average of three scans. The two spectra are normalized to the same height in the figure, but the powder spectrum has only about 15% of the intensity of the crystal spectrum.

isotopes, ^{11}B and ^{10}B. The important NQR parameters for these nuclei are compared in Table V.1 with those of ^{27}Al.

Table V.1: NQR Parameters of ^{27}Al, ^{11}B, and ^{10}B Nuclei

	^{27}Al	^{11}B	^{10}B
Spin (I)	5/2	3/2	3
Natural Abundance (%)	100.0	80.4	19.6
Gyromagnetic Ratio (Hz/G)	1109	1366	458

The major part of our work has been on the ^{11}B isotope. The bonding to the boron nucleus has been discussed by Silver and Bray, and one can conclude that the electric field gradient is axially symmetric and perpendicular to the planes.[10] According to x-ray powder diffraction studies, there is some disorder in the crystal structure.[11,12] Some of the planes are shifted or rotated slightly with respect to the plane below, and this disorder shows up as a broadening of certain reflections in the diffraction pattern. An analysis of the reflection width provides an estimate of the thickness of the crystalline regions between defects. This thickness seems to depend on sample history.[12]

We studied two samples of boron nitride, both purchased from ESPI.[13] One was a 50 mesh powder of 99.5% stated purity. The other was a hot-pressed rod of unspecified purity. According to ESPI, the platelets acquire a preferred orientation during pressing, so there is some tendency of the planes to orient parallel to the cylindrical axis of the rod. ESPI was unable to specify the approximate degree of ordering. Two cylindrically shaped samples were cut from the rod. One had its

cylindrical axis parallel to the rod axis, while the other had its axis perpendicular to the rod axis. Thus we had three NQR samples, which we call powder, axial, and transverse respectively. The spectrum of the powder sample is shown in Figure V.7. The small peak near 1300 kHz is assigned to $B_2O_3 \cdot xH_2O$ impurities, partly on the basis of spectra of the borates presented in the following section. Since $B_2O_3 \cdot xH_2O$ is one of the products of the degradation of boron nitride by steam, it may be reasonably believed to be formed in small quantities when the powder is exposed to moist air. This peak did not appear in spectra from the samples cut from the rod, supporting the hypothesis that it is due to sample degradation through reaction with air. The two rod samples gave signals about twice as large as that for the powder sample, but were otherwise indistinguishable except for this peak near 1300 kHz. This factor of two in intensity is expected purely from the reduced filling factor of the powder sample. The similar shapes, and the relative amplitudes, of the three spectra indicate that the degree of ordering is low in the hot-pressed rod. Of the two rod samples, the signal from the transverse sample was possibly slightly larger, so this sample was used in further studies.

We were interested in studying the lineshape of the main peak near 1450 kHz. To improve the resolution we reduced the dc field to about 1.5 G. The spectrum of the main peak of the transverse sample, recorded in this small field, is shown in Figure V.8. The main peak appears at 1466 ± 2 kHz, in good agreement with the previous room temperature result, 1450 ± 50 kHz.[10] The small shoulder that appears on the low frequency side of the main peak is now more fully resolved. This

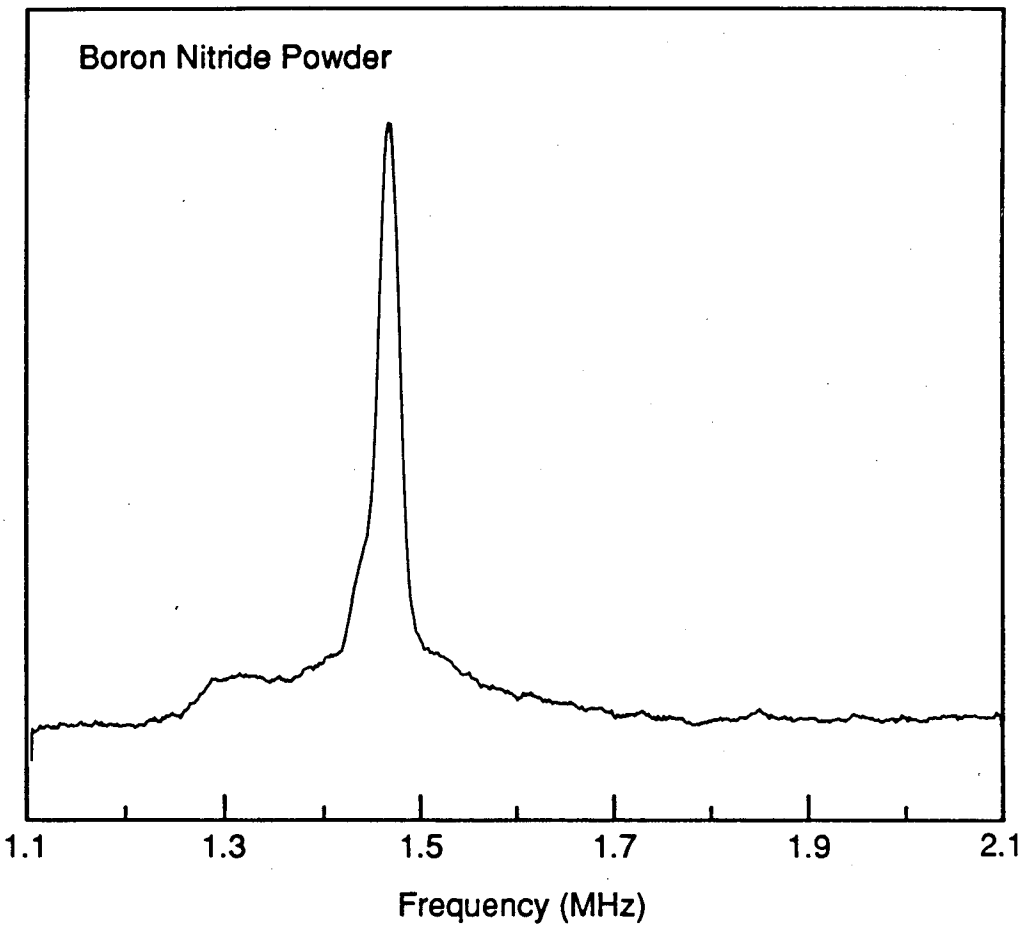

Figure V.7: ^{11}B NQR spectrum of boron nitride (BN) powder. This spectrum, the average of 20 scans, was recorded in a dc field of about 4 G.

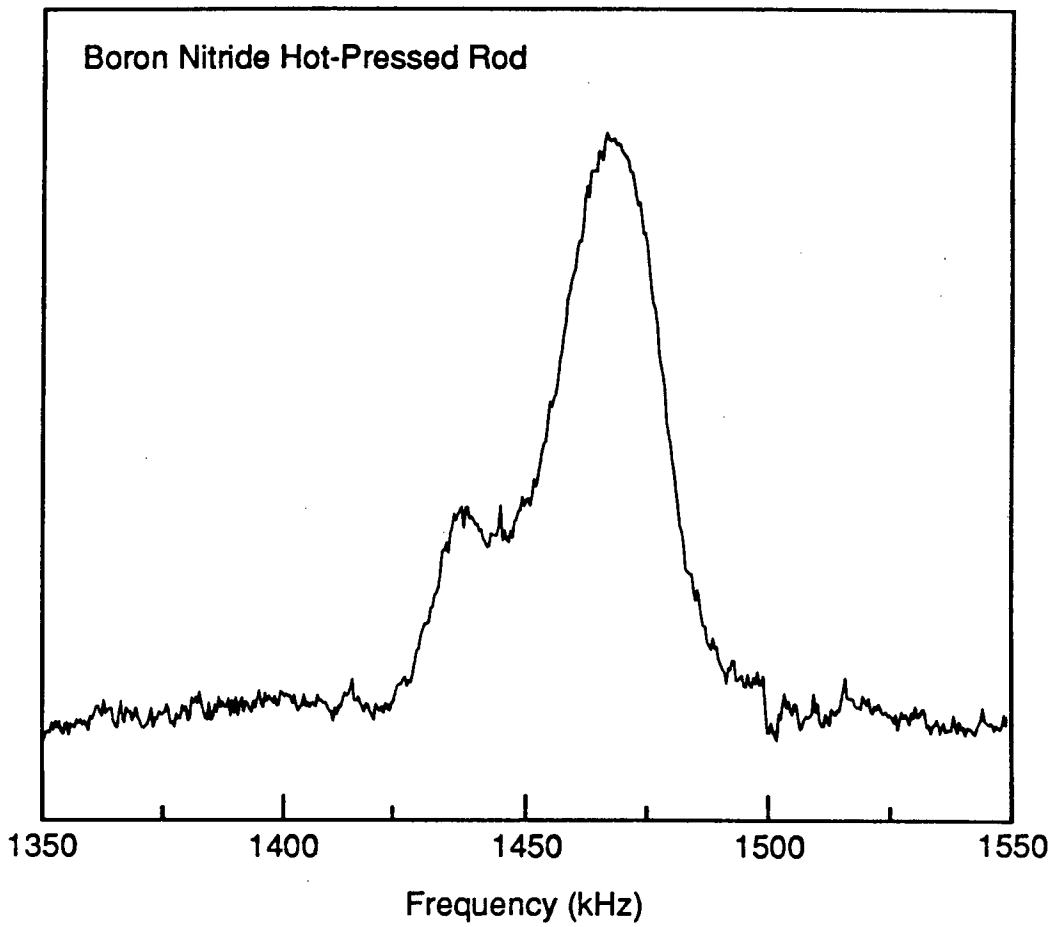

Figure V.8: NQR spectrum of a boron nitride sample cut from a hot-pressed rod. This spectrum, the average of 32 scans, was recorded with a dc field of 1.5 G. Note the reduced sweep width as compared with Figure V.7.

shoulder has not previously been reported for this sample, but the only other study[10] yielded a very poor signal to noise ratio. Given the simple structure of boron nitride, it seems quite reasonable that all the boron nuclei within any one sheet experience the same electric field gradient. We feel that it is unlikely that this peak comes from impurities, since the shoulder also appears with comparable intensity in the powder sample, which has a stated purity of 99.5%. Fitting the spectrum to a sum of Gaussians indicates that about 30% of the total intensity resides in the shoulder.

We suggest that this low frequency resonance may originate from nuclei in the planes at the defect. However, to account for the relatively narrow linewidth, one has to assume that all the defects consist of a shift by the same amount, possibly half a ring diameter. This does seem to be in disagreement with indications that the shifts are randomly distributed.[11] In any case, we can estimate the average thickness of the crystalline platelets, assuming that both types of boron nuclei give signals of comparable intensity. Since roughly 30% of the intensity lies in the shoulder, the platelets must be on average about 6 layers, or 20 Å thick. This result is in reasonable agreement with that published previously, 15 Å, for a sample that had not been annealed to increase crystallinity.[12] As a test of this hypothesis one should anneal a series of samples under different conditions, then compare their x-ray diffraction patterns with their NQR spectra. Recent spectra from a sample of boron nitride prepared by Alfa, which was reportedly highly ordered, did not exhibit the low frequency shoulder. This result rules out causes intrinsic to the pure well-ordered part of

the sample, such as the ^{14}N NQR resonance which is expected to lie in this frequency range.

C. Polycrystalline Borates

In this section we present a study of a few members of the borate family. Although borates have been extensively studied by NQR and NMR,[10,14-21] we were able to obtain some new information.

We consider the series of compounds $B_2O_3 \cdot xH_2O$, for x = 0, 1, and 3. Boric acid, the compound with x = 3, is also written H_3BO_3 or $B(OH)_3$. These compounds are made up of linked BO_3 and BO_4 units.[2,15] The BO_3 unit has a quadrupolar splitting of about 1200 kHz, with a small or zero asymmetry parameter. The splitting frequency is a rather sensitive probe of the immediate environment of the unit. The tetrahedral BO_4 unit has no quadrupolar splitting unless there is some distortion of the tetrahedral symmmetry. These distortions are usually not large enough to produce splittings at a high enough frequency for our spectrometer to be useful. Thus we restrict our attention to the BO_3 unit.

The spectra of polycrystalline samples of $B_2O_3 \cdot 3H_2O$, $B_2O_3 \cdot H_2O$, and B_2O_3 are shown in Figure V.9. The boric acid and B_2O_3 were supplied by Baker Chemical Co. and by ESPI[13] respectively. Both were reported to be of greater than 99.5% purity. $B_2O_3 \cdot H_2O$ was prepared by heating boric acid at 190°C, in an open container, for 26 hours.[15] The quadrupolar splitting frequency, linewidth, and estimated T_1 for these three samples are summarized in Table V.2. The quadrupolar splittings and linewidths are probably accurate to within about 5 kHz.

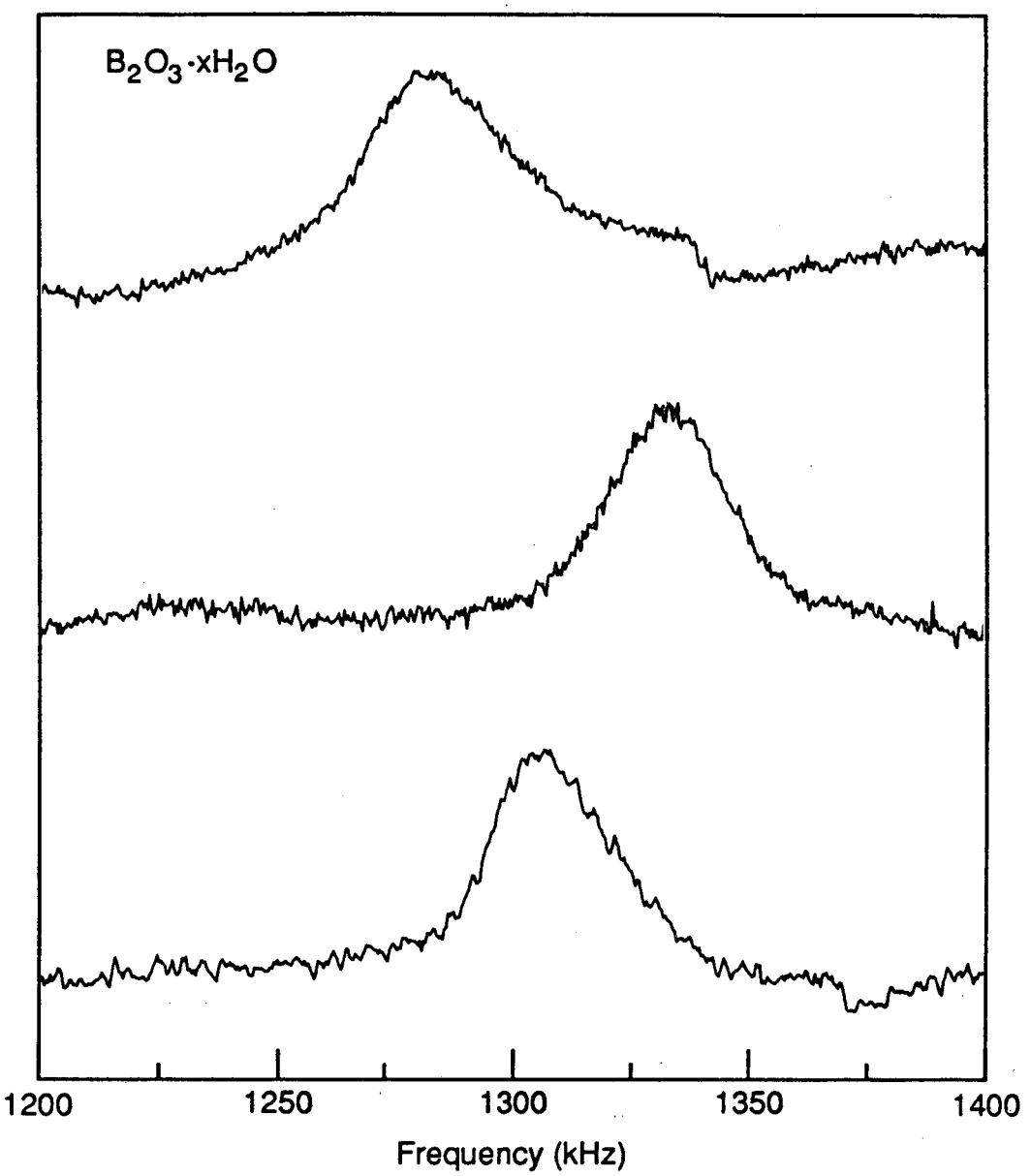

Figure V.9: Boron NQR spectra of the series of polycrystalline samples $B_2O_3 \cdot xH_2O$. From top to bottom, the traces correspond to x = 3, 1, and 0. The top spectrum is the difference of forward and reverse sweeps, while the lower two are from forward sweeps only. The traces are all normalized to the same height.

Table V.2: Measured NQR Parameters for Polycrystalline Borates

	$B_2O_3 \cdot 3H_2O$	$B_2O_3 \cdot H_2O$	B_2O_3
Quadrupolar Splitting (kHz)	1282	1333	1308
Linewidth (kHz)	40	30	30
Estimated T_1 (s)	300	60	60

The relative error in the T_1's is expected to be much larger, since no attempt was made to measure them exactly, but they are probably within a factor of two of the true values. The long T_1 of boric acid was observed in several different samples, some of which were prepared by hydrating B_2O_3. Thus it appears that this long T_1 is a property of the structure itself, and not simply a result of a lower paramagnetic impurity level in this compound. Attempts to reduce the T_1 by doping with paramagnetic ions were unsuccessful.

Two features of the spectra from this series of compounds deserve further attention. One is the resonance frequency of $B_2O_3 \cdot H_2O$. Early experiments by Silver[15] yielded the same quadrupole coupling for boric acid and $B_2O_3 \cdot H_2O$, 1280 ± 10 kHz, but our data distinctly show $B_2O_3 \cdot H_2O$ at a higher frequency. This may be due to the slightly greater precision of our data, or to differences in sample preparation techniques. The quadrupolar splitting of polycrystalline B_2O_3 does not seem to have been previously measured.

Of more fundamental interest is the shoulder appearing at 1340 kHz in the boric acid spectrum. Since the frequency of the shoulder is the same as that for $B_2O_3 \cdot H_2O$, it may be simply that the sample is not fully

hydrated. However, other spectra we have recorded show that the shoulder is much sharper that the $B_2O_3 \cdot H_2O$ resonance. Another possible explanation of this feature is that it is due to the (±2,±3) transition of ^{10}B. The expected resonance frequency for this transition, assuming η is negligibly small, is easily calculated. Using standard tables, the ratio of the frequency of the (±2,±3) transition of ^{10}B, to that for the (±1/2,±3/2) transition of ^{11}B in the same electric field gradient, is calculated as 1.042. Thus the ^{10}B transition should appear near 1336 kHz, in good agreement with the observed position of the shoulder. The estimated peak intensity for ^{10}B is about 25 times less than that for ^{11}B, due to the smaller magnetic moment, lower natural abundance, and larger number of transitions. However, the intensity of the resonance could be enhanced by spin diffusion between the two isotopes. Irradiating at the ^{10}B resonance frequency, coupled with cross-relaxation to the ^{11}B nuclei, would tend to saturate the ^{11}B transition, producing a large change in the sample magnetization. This explanation is supported by the fact that the (±1,±2) transition was not observed after a careful search. We also observe the shoulder in polycrystalline B_2O_3 (Figure V.9), but not in other boron compounds for which the lines are narrower. Spin diffusion is less probable in these compounds, so this data also supports the spin diffusion hypothesis. In addition, we only observe the shoulder in sweeps from high to low frequency, when the ^{11}B transition has not yet been saturated. This behavior indicates that spin diffusion occurs between the shoulder and the main peak. Finally, the shoulder does not appear to be present in preliminary studies of ^{10}B depleted $B_2O_3 \cdot 3H_2O$.

D. B_2O_3 Glass

Dry B_2O_3 exists in the polycrystalline form as studied in the previous section, as well as in the glass phase. The glass phase of pure B_2O_3 has been extensively studied by magnetic resonance,[14,15,17,19,22] but until very recently even simple information, like the linewidth of the NQR resonance, was unavailable. Part of the difficulty in studying glasses is in characterizing the degree of internal randomness. Because of this randomness a distribution of quadrupolar splittings will exist in the glass phase, leading to a broadening of the quadrupolar transition. Early theories of glass structure postulated a series of polycrystalline domains linked in random orientations.[22] Such a structure should give NQR spectra similar to those from polycrystalline samples. If the glass consists of relatively uniform groups in a randomly linked network, as has been proposed by Zachariasen,[23] the NQR linewidth will be relatively small, but larger than that for a polycrystalline sample. If the disorder extends to the structure of the component groups of the glass, the linewidth will be much larger. In this section we present a measurement of the linewidth in B_2O_3 glass, which may partially resolve this question.

The glass sample was prepared by heating polycrystalline B_2O_3 (Aldrich, 99% purity) in a graphite mold. The heat, applied with a propane/oxygen flame, was maintained for about 30 minutes. Bubbling of the melt had essentially ceased by this time. The sample temperature was reduced to room temperature over a period of about 15 minutes, and the graphite mold removed. A colorless glass slug about 4 mm in diameter and

graphite mold removed. A colorless glass slug about 4 mm in diameter and 1 cm long was obtained. ^{11}B spectra from this sample are shown in Figure V.10. Spectra recorded from two similarly prepared samples display no significant differences. This figure shows the importance of adding forward and reverse sweeps when the spectrum is distorted by short spin-lattice relaxation times or by spin-diffusion. The linewidth and resonance frequency are not easily obtained directly from either of the upper two spectra. The linewidth, 80 kHz, and line center, 1360 kHz, were measured from the lower spectrum. This relatively narrow linewidth lends support to the model of borate glasses as formed from small, well ordered domains consisting of a few linked BO_3 and BO_4 groups.[22]

Previous results from Bray and coworkers, obtained by fitting the quadrupolar-perturbed ^{10}B NMR spectrum of B_2O_3 glass, give the distribution in e^2qQ and η.[17] Using their results for the standard deviation of these distributions, $\sigma(e^2qQ/h) = 100$ kHz and $\sigma(\eta) = 0.043$, and assuming the two parameters are uncorrelated, one calculates a linewidth of about 100 kHz for the ^{11}B transition. This result is somewhat larger than our directly measured results. Recently, Bray's group has constructed a conventional cw NQR spectrometer that is reportedly capable of directly measuring the linewidth of resonances in this frequency range.[24-26] They obtain a linewidth of 60 kHz or less for the glass using this new spectrometer. From the pure ^{11}B NQR data alone, there appears to be no way to separate the contributions to the linewidth from variations in e^2qQ and in η. This is mainly because η splits the degeneracy of the $\pm m$ states for integer spin nuclei, such as ^{10}B, but not for half integer spin nuclei like ^{11}B.

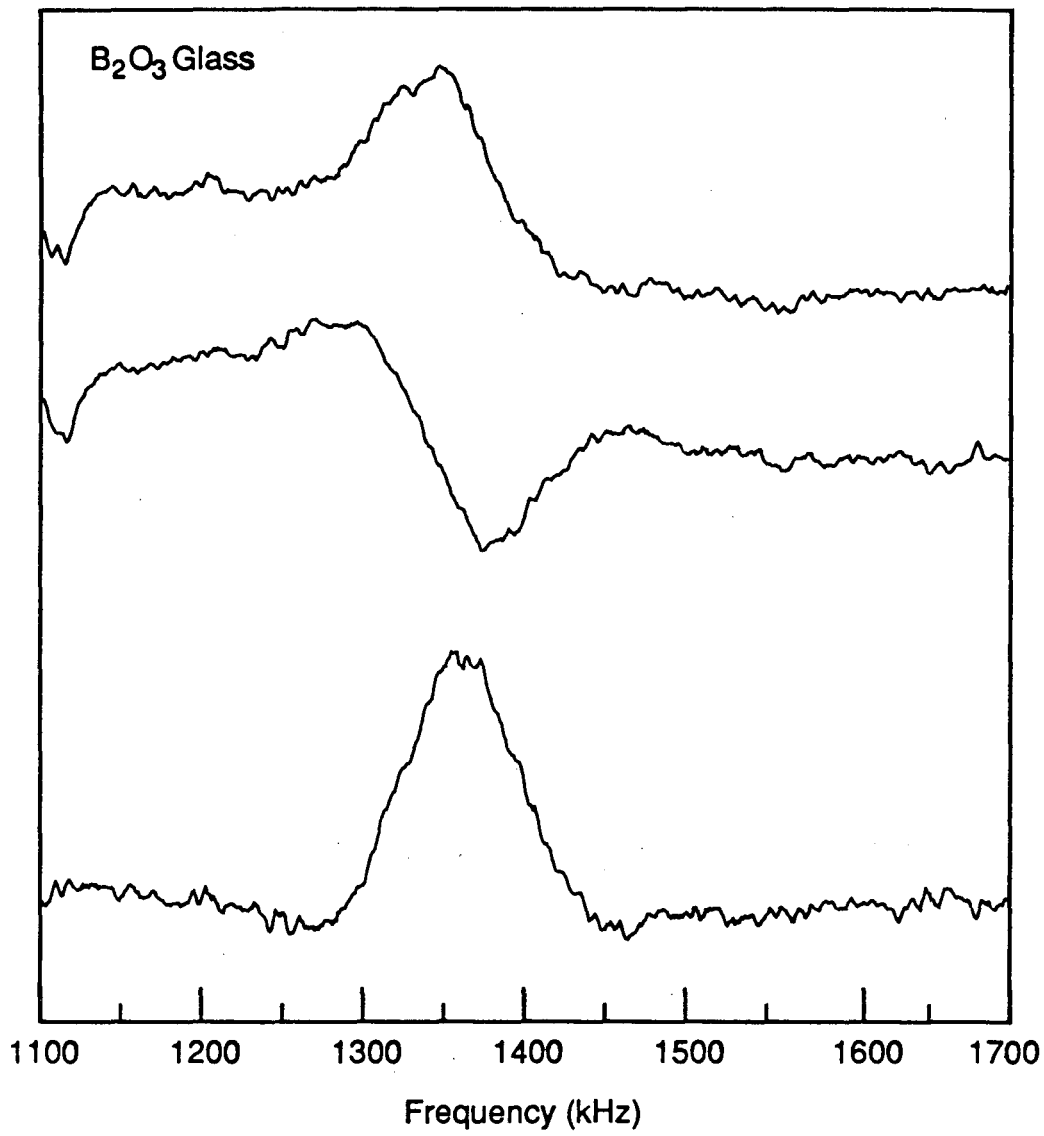

Figure V.10: ^{11}B NQR spectra of B_2O_3 glass. The upper two traces are the forward and reverse sweeps respectively, and the lower trace is their difference. All are normalized to the same height.

REFERENCES

1. T. Jach, Appl. Phys. Lett. 28, 49 (1976).

2. N. N. Greenwood and A. Earnshaw, Chemistry of the Elements (Pergamon Press, Oxford, 1984).

3. R. V. Pound, Phys. Rev. 79, 685 (1950).

4. R. J. Mahler, Phys. Rev. 188, 584 (1969).

5. M. J. Weber and E. L. Hahn, Phys. Rev. 120, 365 (1960).

6. A. H. Silver, T. Kushida, and J. Lambe, Phys. Rev. 125, 1147 (1962).

7. A. Abragam, Principles of Magnetic Resonance (Clarendon Press, Oxford, 1961).

8. C. M. Verber, H. P. Mahon, and W. H. Tantilla, Phys. Rev. 125, 1149 1962).

9. N. Bloembergen, Physica 15, 386 (1949).

10. A. H. Silver and P. J. Bray, J. Chem. Phys. 32, 288 (1960).

11. R. S. Pease, Acta. Cryst. 5, 356 (1952).

12. J. Thomas, Jr., N. E. Weston, and T. E. O'Connor, J. Am. Chem. Soc. 84, 4619 (1963).

13. Electronic Space Products International, 5310-U Derry Ave., Agoura, CA 91301.

14. A. H. Silver and P. J. Bray, J. Chem. Phys. 29, 984 (1958).

15. A. H. Silver, J. Chem. Phys. 32, 959 (1960).

16. P. J. Bray, J. O. Edwards, J. G. O'Keefe, V. F. Ross, and I. Tatsuzaki, J. Chem. Phys. 35, 435 (1961).

17. G. E. Jellison, Jr., L. W. Panek, P. J. Bray, and G. B. Rouse, Jr., J. Chem. Phys. 66, 802 (1977).

18. L. G. Butler and T. L. Brown, J. Magn. Reson. 42, 120 (1981).

19. P. W. France and M. Wadsworth, J. Magn. Reson. 49, 48 (1982).

20. P. J. Bray, J. Non-Cryst. Solids 73, 19 (1985).

21. G. L. Turner, K. A. Smith, R. J. Kirkpatrick, and E. Oldfield, J. Magn. Reson. 67, 544 (1986).

22. P. J. Bray, J. Non-Cryst. Solids 75, 29 (1985).

23. W. H. Zachariasen, J. Am. Chem. Soc. 54, 8 (1932).

24. P. J. Bray, Bull. Am. Phys. Soc. 34, 900 (1989).

25. P. J. Bray, S. J. Gravina, and D. H. Lee, Bull. Am. Phys. Soc. 34, 954 (1989).

26. P. J. Bray, S. J. Gravina, and D. H. Lee, Poster Presentation, Xth International Symposium on Nuclear Quadrupole Resonance Spectroscopy, Takayama, Japan, 1989.

VI. NMR RESULTS

A. Nylon

Aside from the NQR results reported in the previous chapter, the SQUID spectrometer is also useful for low frequency NMR experiments. The Zeeman Hamiltonian, Equation (II-3), is the dominant interaction for these experiments, with the Larmor frequency on the order of 400 kHz. All spectra were recorded at a temperature of 4.2 K

An earlier version of the probe used nylon coil forms for the pickup, rf, and dc coils. We observed a very broad, strong peak near the Larmor frequency of protons when doing experiments at tens of gauss. Even at fields of about 10 G we were able to observe traces of this signal. However, the signal appeared to have a very short recovery time, contrary to what one may expect for organic solids at low temperature. After replacing the nylon coil forms with MACOR forms, we ran experiments on a sample of nylon, obtaining results of which Figure VI.1 is representative. NMR peaks with negative amplitudes are consistent with positive peaks in NQR spectra, since the magnetization is destroyed in NMR experiments, but increased in NQR. The NMR signals are typically about an order of magnitude larger than the NQR signals (see Table IV.1) but this increase is partially offset by higher noise levels, since larger dc magnetic fields are required for NMR.

The resonance in Figure VI.1, centered at 476 kHz, is about 50 kHz wide. Since the peak shows very little distortion at the sweep rate used, 5 khz/s, we estimate T_1 of less than 5 s. This value agrees with

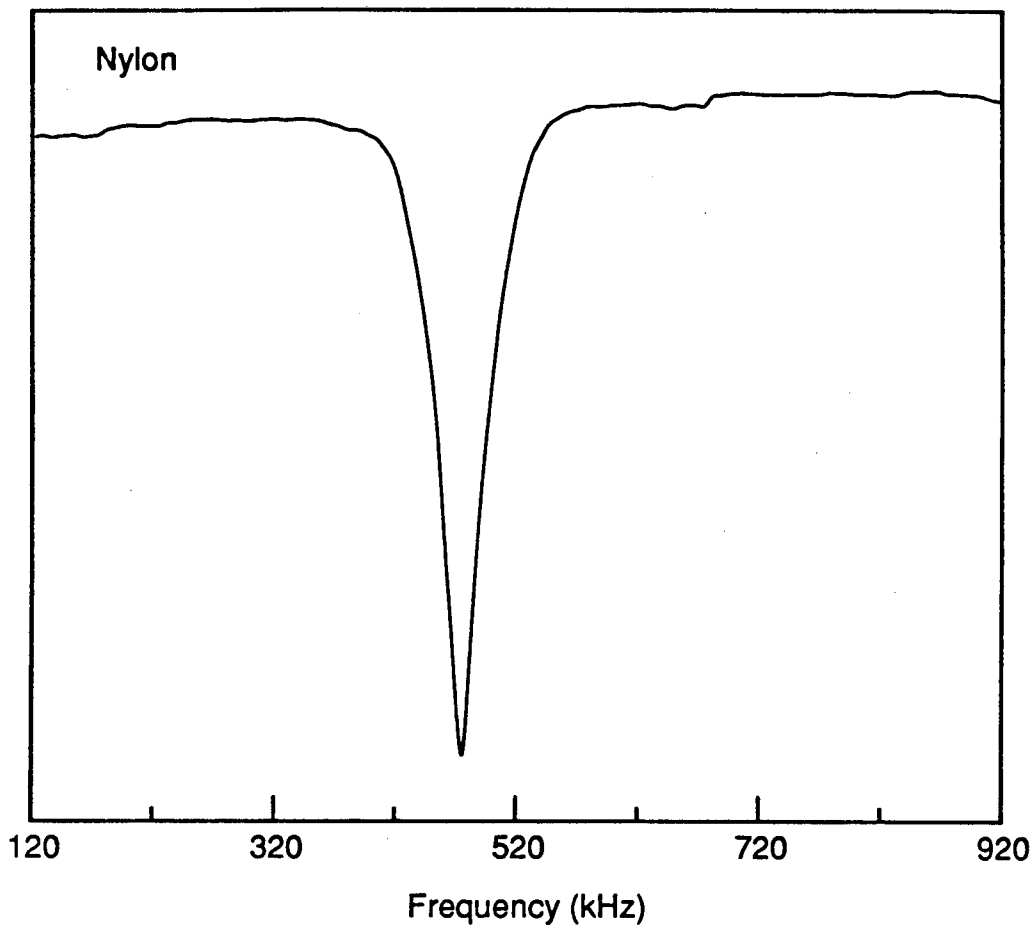

Figure VI.1: z-Axis cw NMR spectrum of ^{1}H in nylon, using a dc magnetic field of 112 G, with a sweep rate of 5 kHz/s.

that previously observed for the background signal, when the nylon coil forms were in place. The process usually responsible for spin-lattice relaxation in organic compounds is the modulation of the dipolar interaction by molecular motion.[1] This process is not very effective in solids at low temperature, with the exception of those solids that contain relatively unhindered methyl groups. The unexpectedly short T_1 observed in nylon is probably due to free radicals[2] remaining from the production process.[3]

The dipolar interaction, which is responsible for the linewidth in most organic solids, could account for the linewidth. Any extra width is probably due to inhomogeneity of the dc field. This is certainly expected, since the lead tube which traps the dc field is only an order of magnitude larger than the sample. For the NQR experiments in powder samples, this inhomogeneity, even if it amounts to 100% of the total field, is of no real importance. The most serious effect it can produce is a possible loss of intensity from regions of the sample where the field is small.

B. Teflon

Since the proton T_1 in nylon is short, apparently due to free radicals, we decided to try to observe the signal from ^{19}F in teflon. Since teflon is created by a free radical polymerization reaction,[3] it should also have a short T_1. We did a series of experiments with different sweep rates, the results of which are shown in Figure VI.2. As can be seen from the decay tail, the T_1 is in fact very short. An

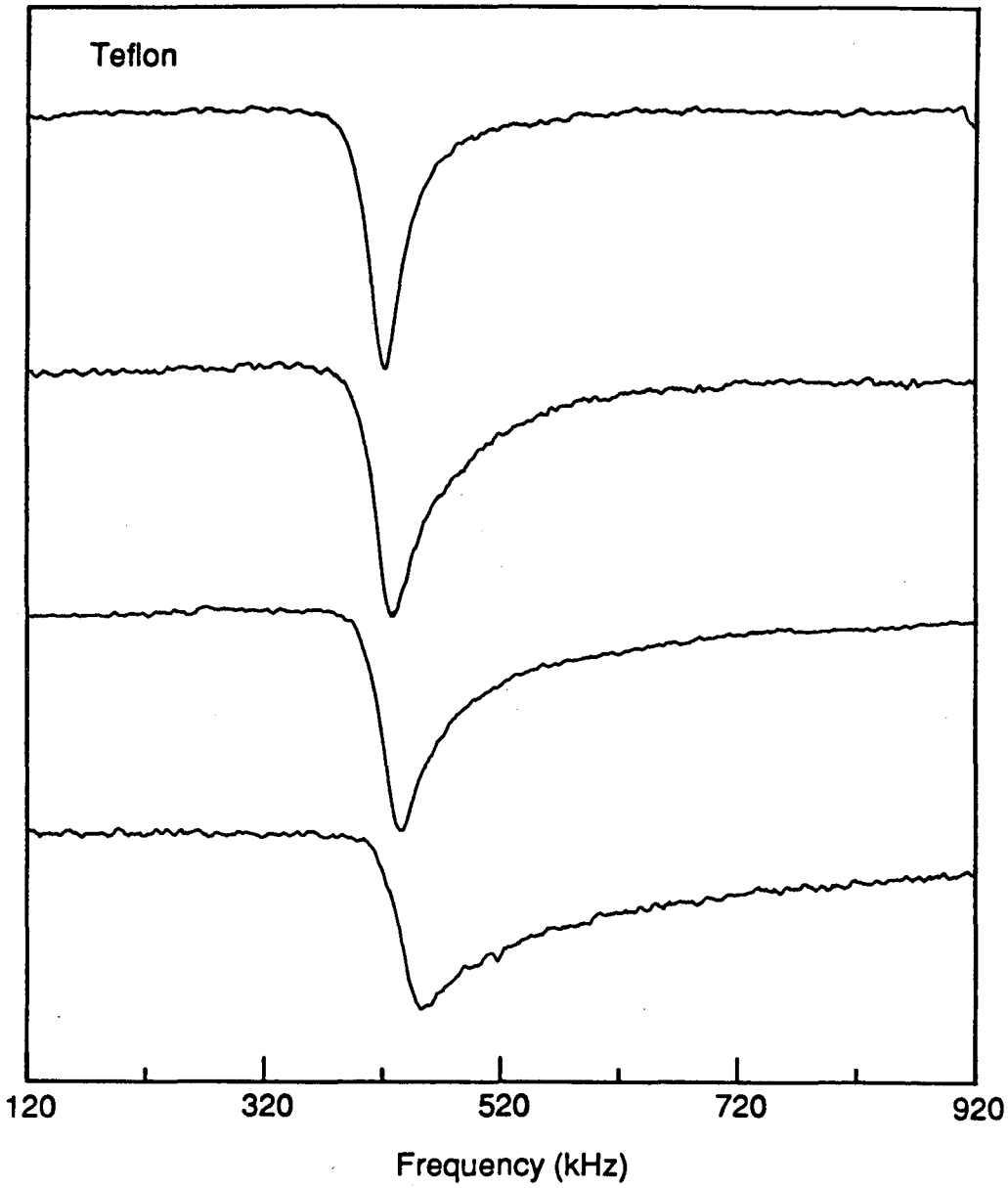

Figure VI.2: ^{19}F NMR spectrum of teflon, for several different sweep rates, in a dc field of 107 G. The rf was swept from low to high frequency, producing a distortion of the high frequency side of the peak at the faster sweep rates. The sweep rates, from top to bottom, are 8, 16, 32, and 80 kHz/s.

exponential fit to the right hand side of the spectra gives $T_1 = 4.2 \pm 0.3$ s. This experiment has the enormous advantage over many conventional methods in that hundreds of points on the T_1 decay curve can be collected in a time of order T_1. Most conventional methods require several T_1's for each point. This technique becomes even more important when complicated, non-exponential decay behaviour occurs, as in superfluid ^{3}He-B.[4,5]

C. Propionic Acid

Propionic acid, $CH_3CH_2CO_2H$, has a much more complicated energy level diagram than the previous two samples because it contains methyl groups. The theory behind the NMR spectra of methyl groups at low temperature has been extensively covered in the literature.[6-12] Rather than reproduce a detailed discussion of this theory, we digress only to provide a qualitative derivation of the methyl group energy level diagram. Hopefully this section will provide an introduction to the more sophisticated discussions available in the literature.

The dominating theme of this discussion will be the symmetry characteristics of the wavefunction describing the methyl group at low temperatures. We assume the methyl group has C_3 symmetry. The total wavefunction can be expressed as

$$\Psi_T = \Psi_e \Psi_v \Psi_r \Psi_s \qquad \text{VI-1}$$

where the four functions in the product correspond to the electronic, vibrational, rotational, and spin parts respectively. According to the

Pauli principle, Ψ_T must be antisymmetric under exchange of two protons.[13] Under exchange of two pairs of protons then, the total wavefunction must be symmetric. This operation corresponds to a rotation by $2\pi n/3$, i.e. an operation by C_3. An inspection of the C_3 character table shows that Ψ_T must therefore have A symmetry. We will also make

Table VI.1: The C_3 Character Table

C_3	E	C_3	C_3^2	
A	1	1	1	
E_a	1	ϵ	ϵ^*	
E_b	1	ϵ^*	ϵ	$\epsilon = e^{2\pi i/3}$

use of the multiplication rules

$$A \times A = A \qquad A \times E_a = E_a \qquad A \times E_b = E_b$$

$$E_a \times E_a = E_b \qquad E_b \times E_b = E_a \qquad E_a \times E_b = A$$

to determine the symmetry of the product of wavefunctions. It is generally assumed that Ψ_e and Ψ_v are ground state functions of A symmetry. Therefore the possible products $\Psi_r\Psi_s$ are restricted to those with A symmetry.

We consider the form of Ψ_r first. The rotational Hamiltonian appropriate to the methyl group is the sum of a kinetic term, corresponding to the free rotation of the group, and a potential term $V(\phi)$, assumed for simplicity to possess threefold symmetry,

$$\mathcal{H}_r = -\frac{\hbar^2}{2I}\frac{\partial^2}{\partial\phi^2} + \frac{1}{2}V(1 - \cos 3\phi) \quad . \qquad \text{VI-2}$$

The problem now is to find the eigenstates of $\mathcal{H}_r$. One approach, particularly useful for states with energies much lower than the barrier height V, is an expansion in harmonic oscillator states.[7,14] To rationalize this, we consider a Taylor series expansion of the potential in $\mathcal{H}_r$, about the minima at $\phi_o = 0$, $2\pi/3$, and $-2\pi/3$. To first order in the expansion we obtain

$$V(\phi) \cong \frac{9}{4}V(\phi - \phi_o)^2 \quad . \qquad \text{VI-3}$$

Now Equation (VI-2) can be expressed as

$$\mathcal{H}_r = -\frac{\hbar^2}{2I}\frac{\partial^2}{\partial\phi^2} + \frac{1}{2}I\omega^2(\phi - \phi_o)^2 \qquad \text{VI-4}$$

where I is the moment of inertia of the group, and ω is defined by

$$\omega = \left(\frac{9V}{2I}\right)^{1/2} \quad . \qquad \text{VI-5}$$

The solutions to Equation (VI-4) are the Hermite polynomials in $(\phi - \phi_o)$. The vibrational ground state is triply degenerate, with eigenstates explicitly expressed by

$$X_o(\phi_o) = \left(\frac{I\omega}{\hbar\omega}\right)^{1/2} \exp((-I\omega(\phi - \phi_o)^2/2\hbar) \qquad \text{VI-6}$$

where, again, $\phi_o = 0, \pm 2\pi/3$.

Now we return to the exact Hamiltonian of Equation (VI-2) and express its eigenstates in the basis formed by the three harmonic oscillator ground states. This requires diagonalizing a 3 by 3 matrix, with elements given by

$$\int_0^{2\pi} X_o(\phi_o)\mathcal{H}_r X_o(\phi_o')d\phi \quad . \qquad \text{VI-7}$$

Explicit evaluation of the integrals is tedious but straightforward. By convention one element of the matrix has been associated with a frequency ω_t, called the tunneling frequency,[7]

$$\omega_t = -\frac{3}{\hbar}\int_0^{2\pi} X_o(0)\mathcal{H}_r X_o(-2\pi/3)d\phi \quad . \qquad \text{VI-8}$$

The eigenstates of $\mathcal{H}_r$ in the basis of Equation (VI-6) are found to be

$$\begin{aligned}
\Psi_o^1 &= \frac{1}{\sqrt{3}}\left(X_o(0) + X_o(-2\pi/3) + X_o(2\pi/3)\right) \\
\Psi_o^\epsilon &= \frac{1}{\sqrt{3}}\left(X_o(0) + \epsilon X_o(-2\pi/3) + \epsilon^* X_o(2\pi/3)\right) \qquad \text{VI-9} \\
\Psi_o^{\epsilon^*} &= \frac{1}{\sqrt{3}}\left(X_o(0) + \epsilon^* X_o(-2\pi/3) + \epsilon X_o(2\pi/3)\right)
\end{aligned}$$

where $\epsilon = e^{2\pi i/3}$. The functions in Equation (VI-9) are three of the possible states represented by Ψ_r in Equation (VI-1). The corresponding eigenvalues are

$$E^1 = E_o - \frac{2\hbar\omega}{3}t$$

$$E^\epsilon = E^{\epsilon^*} = E_o + \frac{\hbar\omega}{3}t \qquad \text{VI-10}$$

where E_o is the ground vibrational energy in the approximately harmonic potential. To determine the symmetry of the products $\Psi_r\Psi_s$, we need to classify the three eigenstates in Equation (VI-9) according to the irreducible representations of the C_3 group. This may be done by determining the eigenvalues of each state for the operations of the group, with the help of the character table. For example, with the C_3 operation defined so as to increase ϕ,

$$C_3\Psi_o^\epsilon = \epsilon^*\Psi_o^\epsilon \quad . \qquad \text{VI-11}$$

One finds that the states Ψ_o^1, Ψ_o^ϵ, and $\Psi_o^{\epsilon*}$ transform as the A, E_b, and E_a irreducible represention respectively. The energy level diagram for these rotational states is given in Figure VI.3. In somewhat loose terms one can think of the E_a and E_b states as corresponding to rotation of the methyl group in opposite directions, while the A state describes a non-rotating methyl group. Hence the term rotational polarization is used to describe a system in which a population imbalance exists between the E_a and E_b levels.

Now we consider the spin part of the total wave function. Ignoring the dipolar interaction, the spin Hamiltonian is simply the Zeeman term,

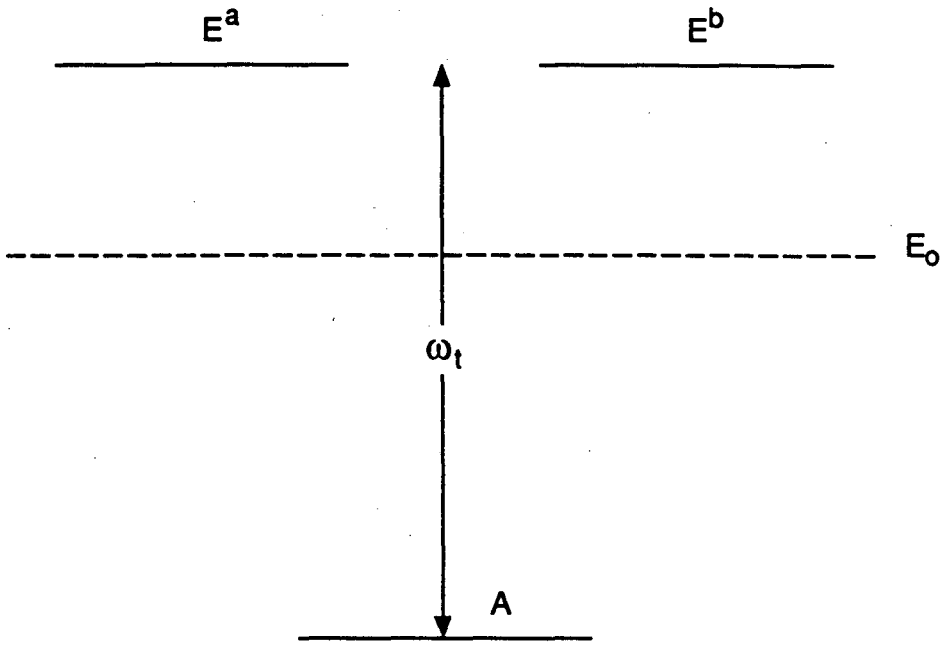

Figure VI.3: Energy level diagram for the rotational part of the wavefunction describing a tunneling methyl group. The energy E_o is the ground state vibrational energy.

$$\mathcal{H}_z = -\hbar\gamma H_o \sum I_z \quad . \qquad \text{II-3}$$

where the sum over I_z corresponds to a sum over the three protons in the methyl group. The simplest set of eigenstates is simply the eight direct products of the eigenstates for each proton. For example, the configuration with spins 1 and 2 in the spin up state and spin 3 in the spin down state corresponds to the eigenstate $|\alpha\alpha\beta\rangle$. However, these simple direct product eigenstates are not eigenstates of the C_3 symmetry group operations, so cannot be simply classified as having A, E_a, or E_b symmetry. It is necessary to form linear combinations of the degenerate direct product states to generate a set of eigenstates of the symmetry operations, which are simultaneously eigenstates of the Zeeman Hamiltonian. These symmetry adapted states are characterized by the irreducible representation they transform under, and also by the total quantum number $m = m_1 + m_2 + m_3$. Explicitly, the states are[6]

$$\begin{aligned}
A_{3/2} &= |\alpha\alpha\alpha\rangle \\
A_{1/2} &= \tfrac{1}{\sqrt{3}}(|\alpha\alpha\beta\rangle + |\alpha\beta\alpha\rangle + |\beta\alpha\alpha\rangle) \\
A_{-1/2} &= \tfrac{1}{\sqrt{3}}(|\beta\beta\alpha\rangle + |\beta\alpha\beta\rangle + |\alpha\beta\beta\rangle) \\
A_{-3/2} &= |\beta\beta\beta\rangle \\
E^a_{1/2} &= \tfrac{1}{\sqrt{3}}(|\alpha\alpha\beta\rangle + \epsilon|\alpha\beta\alpha\rangle + \epsilon^*|\beta\alpha\alpha\rangle) \\
E^a_{-1/2} &= \tfrac{1}{\sqrt{3}}(|\beta\beta\alpha\rangle + \epsilon|\beta\alpha\beta\rangle + \epsilon^*|\alpha\beta\beta\rangle) \\
E^b_{1/2} &= \tfrac{1}{\sqrt{3}}(|\alpha\alpha\beta\rangle + \epsilon^*|\alpha\beta\alpha\rangle + \epsilon|\beta\alpha\alpha\rangle) \\
E^b_{-1/2} &= \tfrac{1}{\sqrt{3}}(|\beta\beta\alpha\rangle + \epsilon^*|\beta\alpha\beta\rangle + \epsilon|\alpha\beta\beta\rangle) \quad .
\end{aligned} \qquad \text{VI-12}$$

The energy level diagram for these spin states is shown in Figure VI.4.

Now we return to the condition from the start of this section, which requires that the product of the spin and rotational wavefunctions must be of A symmetry. This restricts the products to the combination A x A, E_b x E_a, and E_a x E_b. For example, if the methyl group is in the E_b rotational state, the nuclear spin state must be either $E^a_{+1/2}$ or $E^b_{-1/2}$. The energies of the eight possible product states are depicted in Figure VI.5, with the ratio of tunnel splitting to Zeeman splitting appropriate to the conditions under which propionic acid was studied. Since the rotational and spin Hamiltonians commute, the energies of the product states are simply given by the sum of the energies for the spin and rotational states.

On first glance it may appear that an rf field could be used to excite transitions between the A and E states, thereby providing a direct measure of the tunnel splitting. A simple argument shows that this is forbidden on symmetry grounds.[15] The transition matrix element for excitation between two states Ψ_1 and Ψ_2 has the form

$$\int \Psi_1^* \mathcal{H} \Psi_2 d\tau \qquad \text{VI-13}$$

where $\mathcal{H}$ is the Hamiltonian used to induce the transitions, and the integral over $d\tau$ symbolizes integration over the configuration space of the system. This integral vanishes unless the product $\Psi_1 \mathcal{H} \Psi_2$ has a component of A symmetry. For rf excitation, $\mathcal{H}$ has the form given by Equation (II-4), and does not have the appropriate symmetry to induce transitions between states of different symmetry. Transitions between states of A and E symmetry are therefore symmetry forbidden. However, as

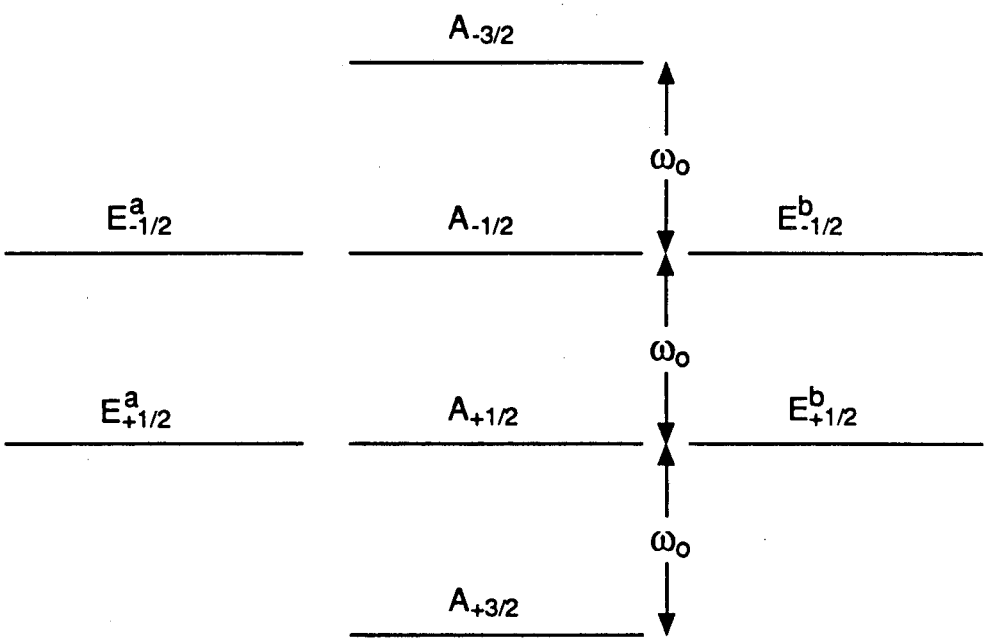

Figure VI.4: Energy levels of the symmetry adapted spin states of a methyl group.

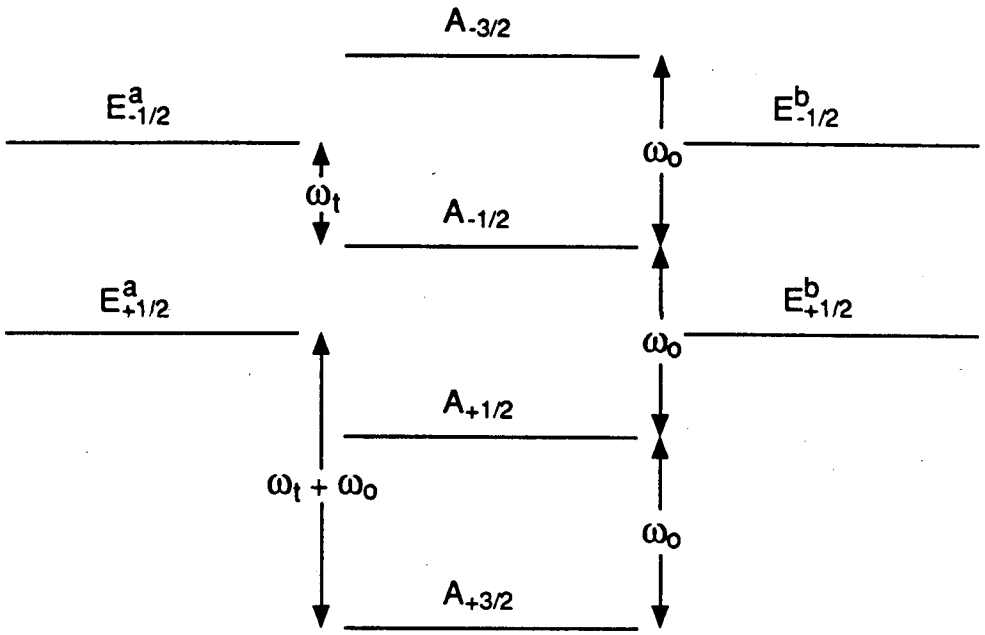

Figure VI.5: Energy level diagram for the product of the spin and rotational states, labeled acording to the symmetry of the spin part of the wavefunction. The E states are increased in energy by $\hbar\omega_t$, as compared to Figure VI.4. Transitions between E and A states are symmetry forbidden in high field NMR, but become allowed in low field.

explained by Clough and co-workers, there are ways to excite the transitions using low-field NMR.[16,17]

According to Clough's picture, the rf field and the dc field can be summed to give a time dependent magnetic field.[16] In the lab frame the field vector oscillates at the rf frequency. In a reference frame moving with the field, the dipolar interaction contains terms changing at the rf frequency. Thus the appropriate Hamiltonian in Equation (VI-3) is the dipolar Hamiltonian, which, because of its greater complexity, is able to induce transitions between the A and E states. The matrix elements of the dipolar Hamiltonian have been calculated by Zweers[8] and others,[9,10,18] in the context of spin-lattice relaxation. Note that, according to this picture, the transition probability depends on the strength of the rf and dc fields, and on the strength of the dipolar coupling, but not on the tunnel splitting itself. Thus this method is more generally useful than older methods which were used to directly measure tunnel splittings, but are only useful if the splittings are from one to five times larger than the dipolar coupling.[19,20]

In Figure VI.6 we show low field NMR spectra of Cu^{2+}-doped propionic acid. Paramagnetic doping was used to reduce the T_1 from several minutes to about one minute. The energy level diagram for the methyl group (Figure VI.5) shows that several forbidden transitions may occur in a low field experiment. Their frequencies, in an frequency swept experiment, are ω_t, $\omega_o \pm \omega_t$, and $2\omega_o \pm \omega_t$. Previous work by Clough and co-workers, using field-cycling NMR, shows that the tunnel splitting of propionic acid at 4.2 K is 210 kHz.[17] Initial spectra recorded with our spectrometer, using undoped propionic acid at a Larmor frequency of

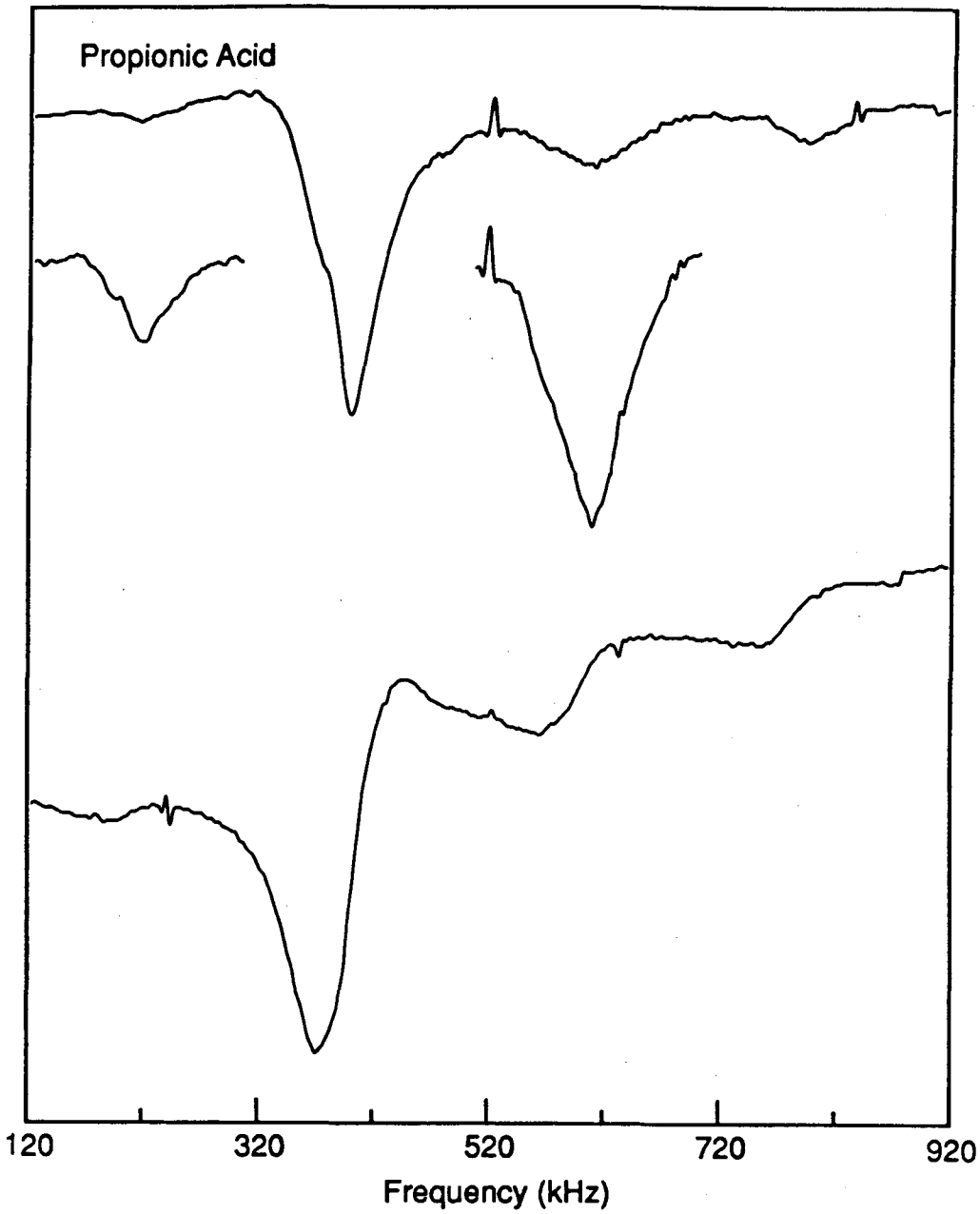

Figure VI.6: Low field z-axis NMR spectra of Cu^{2+}-doped propionic acid at 4.2 K, in a dc field of 95 G. The upper trace, recorded using a sweep from low to high frequency, shows symmetry forbidden transitions at the methyl group tunneling frequency, and at the sum of the Larmor and tunneling frequencies. The insets were produced by summing over several such spectra. The shoulder on the low frequency side of the main peak comes from ^{19}F in teflon spacers in the sample tube. A sweep from high to low frequency, using the same sweep rate as for the upper trace, yielded the lower trace. The slope in the baseline appears to be due to a longer effective spin-lattice relaxation time, not to drift in the spectrometer baseline level.

437 kHz, show transitions at 226 and 647 kHz, i.e. at $\omega_o \pm \omega_t$. Figure VI.6, recorded with a Larmor frequency of 400 kHz, shows clear transitions at 210 and 610 kHz. i.e. at ω_t and at $\omega_o + \omega_t$. At present we have no explanation for this discrepancy, but the possibility that doping the sample is responsible for this difference should not be ignored. Using the results of Zweers,[8] it appears that the ω_t transition should be about 5/3 times as intense as the $\omega_o - \omega_t$ peak, ignoring the Boltzmann factor. Note that one must be careful when comparing the spectra recorded by Clough's group, where the field is incremented, to our spectra obtained using a frequency sweep. These two techniques give peaks at different frequencies when studying complex systems with forbidden transitions.

Part of the purpose in pursuing this problem is to test a hypothesis by Clough.[17] He explains asymmetric lineshapes in his spectra by introducing a molecular friction which dissipates the rotational motion of the methyl group. This friction splits the energies of the E_a and E_b states if a rotational polarization is generated. In other words, the energy levels of the E states depends on their relative populations. Our spectrometer is possibly more suited to making this type of measurement than is Clough's field-cycling apparatus, because we can measure the complete spectrum in a time of order T_1. Thus a splitting of the E states would appear as a shift in the tunneling peaks, rather than as an asymmetry in the peak shapes. Experiments aimed at testing this molecular friction hypothesis have not been completed.

D. γ-Picoline

γ-Picoline, pictured below, is famous because for many years it

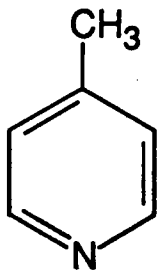

was the one known example of a very interesting low-temperature phenomenon, the Haupt effect.[8,21-24] This effect relies on the symmetry of the CH_3 group. Phenomenologically, the effect is quite simple. The tunnel splitting in γ-picoline is very large, 0.13 THz at 4.2 K,[25] so there is a large population difference between the A and E states at thermal equilibrium. Consider the effect of a rapid reduction in sample temperature. To restore thermal equilibrium across the tunnel splitting, there must be an increase in the number of spins in the A state at the expense of the E spins. There are several transitions which accomplish this result, corresponding to all the possible ways of pairing up the A and E states. The key to the Haupt effect is that not all these transitions occur at the same rate. Depending on the details of the sample, a population excess will accumulate in either the $A_{\pm 1/2}$ or the $A_{\pm 3/2}$ states. This population imbalance is referred to as dipolar order, since the dipolar Hamiltonian produces a splitting between the $A_{\pm 1/2}$ and the $A_{\pm 3/2}$ states in zero field. For γ-picoline, the effect is relatively slow on the NMR time scale. The time constant for establishment of thermal equilibrium across the tunnel splitting is several thousand

seconds at 4.2 K, while the time constant for creating dipolar order is about 30 s at this temperature.[23] Different microscopic interpretations of the Haupt effect have been proposed.[21,22]

The dipolar polarization generated by this effect can be very large, about 10^4 time larger than the thermal equilibrium dipolar order. With this enhancement the magnitude of the dipolar polarization corresponds to a splitting of tens of megahertz, and is comparable to the Zeeman polarization in high field NMR. In γ-picoline, the effect is easily seen with conventional cw and pulsed NMR spectrometers. The Haupt effect has also been observed in lithium acetate,[26] and in matrix isolated CH_3CN and CH_3F.[27]

We are interested in the Haupt effect for several reasons. Mixing γ-picoline with other organic liquids at room temperature may produce a large polarization of the other compound, when the temperature of the mixture is rapidly reduced to liquid helium temperature. This may permit signal enhancement in a wide variety of samples. If γ-picoline is mixed with an insoluble powder, it may be possible to selectively observe the nuclei near the surface of the powder. Also, the Haupt effect directly produces dipolar order, so measurements of the zero-field dipolar splitting, an interesting low frequency application of our spectrometer, may become more convenient. We have a convenient way to carry out the temperature jump in zero field, as well as the capability to measure dipolar order in zero field. In addition, more information on the mechanism of this interesting effect may be obtained if the experiment can be carried out in zero field.

The experiments described here were performed on a sample of

γ-picoline vacuum distilled in three cycles, then sealed in a Pyrex tube. Originally the material was tinted brown, but became clear after distillation. The temperature jump was carried out somewhat crudely. A carbon resistor, with known resistance at 77 K and at 4.2 K, was mounted inside the sample stick about 1.5" above the sample. The sample was withdrawn to the region above the liquid helium in the cryostat, where the resistance corresponded to about 77 K. After several minutes at this temperature, the sample was quickly immersed in the helium bath, but not inside the dc field in the sample chamber. After about two minutes in the helium bath, the sample was inserted into the pickup coil. The output of the SQUID was monitored as soon as possible, typically about 5 s after the sample was placed in the pickup coil. We observed a large exponential drift in output, with a time constant of about 60 s, a few orders of magnitude larger than the equilibrium sample magnetization. This observation may be related to the Haupt effect, since the direction of the drift was the same for many temperature jumps, and changed sign when the field was inverted. However, some caution should be used in its interpretation. Small concentrations of paramagnetic impurities in the sample or sample holder could be responsible. Thermal effects are possible but unlikely.

Our primary evidence that the Haupt effect has ocurred is a large increase in the signal magnitude, and a markedly different signal shape. The peak-to-peak signal amplitude, as a function of the time since the temperature jump, is plotted in Figure VI.7. An exponential fit gives a decay time constant of 3.6 ± 1.3 ks. The large error is not due to scatter in the data, rather to the fact that the decay curve is not a

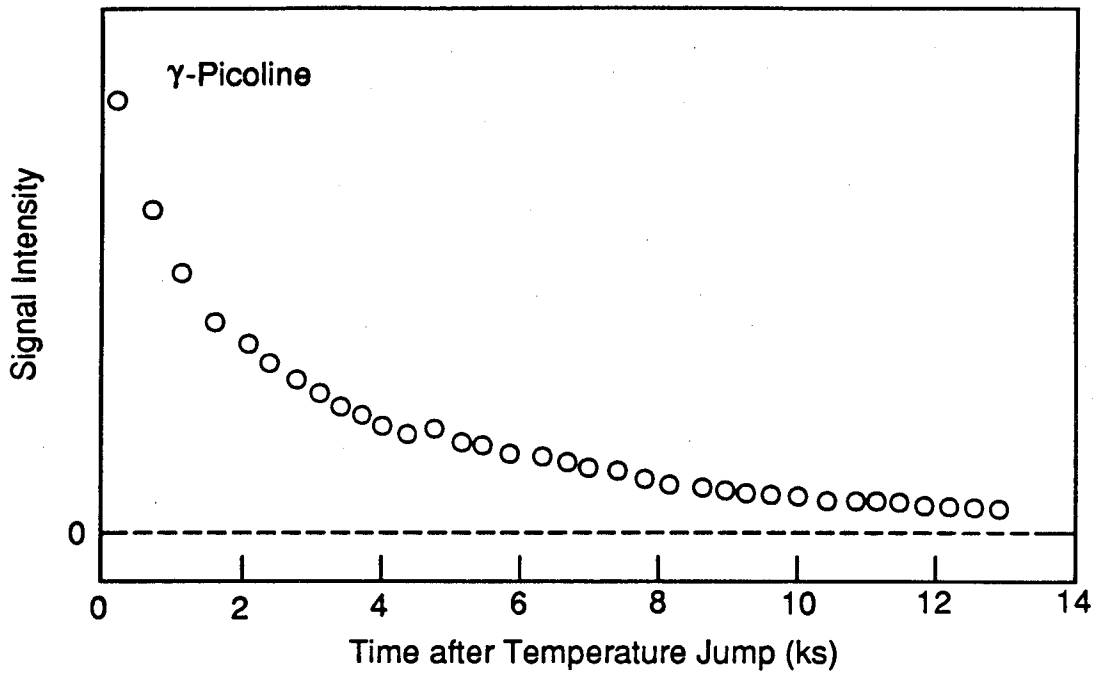

Figure VI.7: Amplitude of the NMR signal from γ-picoline, as a function of the time after a temperature jump from about 77 K to 4.2 K. The dc field was 107 G.

simple exponential. The initial magnitude shows an enhancement of the NMR signal by a factor of at least 50. Typical lineshapes are shown in Figure VI.8. As can be readily seen, a sweep through the resonance position produces an initial decrease in the magnetization, followed by a large increase. This behavior is characteristic of systems with a mixture of Zeeman and dipolar order.[24] The dipolar order produces a dispersion-type lineshape, while the Zeeman order gives a negative absorption type signal. The ratio of dipolar to Zeeman order is greatest about 100 s after the jump, and then decays to zero after tens of thousands of seconds. This decay can be observed in Figure VI.8 by noting the relative heights of the positive and negative components in each spectrum. Detailed interpretation of the results have not yet been completed.

In summary, the results discussed in this chapter show that, in addition to its usefulness for NQR measurements, the SQUID spectrometer is an important tool for low-frequency NMR. Spin-lattice relaxation measurements can be easily and accurately made. Carefully designed and interpreted experiments may provide a great deal of information on the energy level structure of methyl groups at low temperatures. In addition, symmetry conversion and spin-diffusion rates are much more accessible than with conventional NMR instrumentation, or with field-cycling spectrometers.

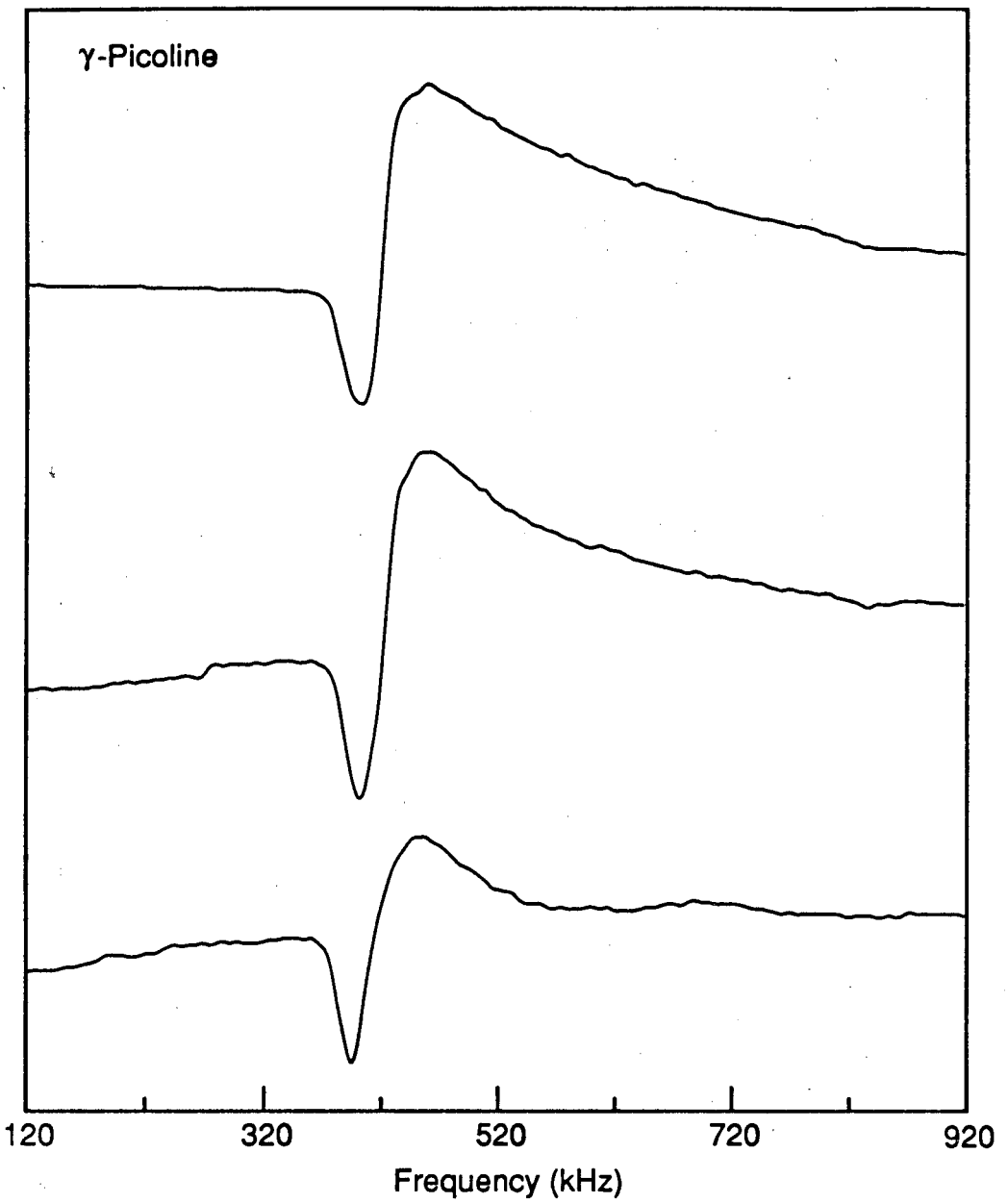

Figure VI.8: Lineshape of the γ-picoline resonance after a temperature jump from about 77 K to 4.2 K. From top to bottom, the traces were recorded 500 s, 6500 s, and 12000 s after the jump. The spectra are scaled to roughly the same amplitude. Their relative heights are represented in Figure VI.7.

REFERENCES

1. A. Carrington and A. D. McLachlan, Introduction to Magnetic Resonance (Harper and Row, New York, 1967).

2. N. Bloembergen, Physica, 15, 386 (1949).

3. A. Streitwieser, Jr. and C. H. Heathcock, Introduction to Organic Chemistry (Macmillan, New York, 1976).

4. R. A. Webb, Rev. Sci. Instrum. 48, 1585 (1977).

5. A. Abragam and M. Goldman, Nuclear Magnetism: Order and Disorder (Clarendon Press, Oxford, 1982).

6. J. H. Freed, J. Chem. Phys. 43, 1710 (1965).

7. S. Clough, in NMR-Basic Principles and Progress, edited by M. M. Pintar, Vol. 13 (Springer-Verlag, Berlin, 1976).

8. A. E. Zweers, Ph.D. Thesis, Leiden, 1976.

9. S. Clough, J. Phys. C 4, 2180 (1971).

10. S. Emid, R. J. Baarda, J. Smidt, and R. A. Wind, Physica 93B, 327 (1978).

11. S. Emid, R. A. Wind, and S. Clough, Phys. Rev. Lett. 33, 769 (1974).

12. B. Gabryś, Mol. Phys. 51, 601 (1984).

13. H. Clark, A First Course in Quantum Mechanics (Van Nostrand Reinhold, Berkshire, 1982).

14. W. H. Flygare, Molecular Structure and Dynamics (Prentice Hall, Englewood Cliffs, New Jersey, 1978).

15. L. D. Landau and E. M. Lifshitz, Quantum Mechanics, Non-Relativistic Theory, 3rd. ed. (Pergamon Press, Oxford, 1977).

16. S. Clough, A. J. Horsewill, P. J. McDonald, and F. O. Zelaya, Phys. Rev. Lett. 55, 1794 (1985).

17. S. Clough, G. J. Barker, K. J. Abed, and A. J. Horsewill, Phys. Rev. Lett. 60, 136 (1988).

18. J. Haupt, Z. Naturforsch. 26a, 1578 (1971).

19. C. S. Johnson, Jr. and C. Mottley, Chem. Phys. Lett. 22, 430 (1973).

20. J. A. Ripmeester, S. K. Garg, and D. W. Davidson, J. Chem. Phys. 67, 2275 (1977).

21. J. Haupt, Z. Naturforsch. 28a, 98 (1973).

22. S. Clough, Phys. Lett. 42A, 371 (1973).

23. P. Beckmann, S. Clough, J. W. Hennel, and J. R. Hill, J. Phys. C 10, 729 (1977).

24. B. Van Reit and L. Van Gerven, Phys. Rev. B 26, 2442 (1982).

25. B. Alefeld, A. Kollmar, and B. A. Dasannacharya, J. Chem. Phys. 63, 4415 (1975).

26. L. Crits and L. Van Gerven, in Quantum Aspects of Molecular Motion in Solids, edited by A. Heidemann, A. Magerl, M. Prager, D. Richter, and T. Springer (Springer-Verlag, Berlin, 1987).

27. M. Murphy and D. White, Poster Presentation, 30th Experimental NMR Spectroscopy Conference, Pacific Grove, CA, 1989.

LAWRENCE BERKELEY LABORATORY
UNIVERSITY OF CALIFORNIA
INFORMATION RESOURCES DEPARTMENT
BERKELEY, CALIFORNIA 94720